DISSERTATION

Titel der Dissertation

„Neural control over crawling and steering motions underlies the regulation of locomotion strategies in *C. elegans*“

Verfasserin

Ingrid Margarete Hums

angestrebter akademischer Grad

Doctor of Philosophy (PhD)

Wien, Oktober 2015

1 Summary

1.1 Abstract

Animals must be able to control their locomotion strategy to efficiently navigate through their environment. For effective travel across distances, fast and regular movements are beneficial, while less regular but more flexible motions enable a more thorough exploration of the nearby environment (= local search). In my thesis work I addressed the questions of how animals coordinate stereotypic and more flexible motions to yield distinct travel or local search behaviors, and how they control switches between these different locomotion strategies.

I studied locomotion behaviors of the nematode *C. elegans*, which travels longer distances via regular undulatory motions along its entire body (= body waves), but drastically changes its locomotion strategy into a local exploratory search when evoked by a specific sensory stimulus (decrease in ambient oxygen levels). With a computational decomposition approach I quantitatively captured the behavioral changes in the worms' body waves: I described worm locomotion as two parallel overlaid motion patterns that generate either regular crawling motions or more flexible and irregular steering /turning motions. I demonstrated how inverse adjustment of the motion patterns, which were termed crawling wave and steering wave, in coordination with locomotion speed enabled the animals to alter their locomotion strategy from fast and directed travel to local search after the stimulus. In summary, the crawling wave, which was strong during traveling behavior, decreased while animals slowed down. At the same time the steering wave increased in strength leading to more complex postures resulting in many steering and turning maneuvers that enabled exploration of the local environment.

I aimed to identify parts of the neural control system regulating crawling and steering motions. Using genetic manipulations and calcium imaging of neural activity, I characterized two posture-modulating counter-acting interneuron classes, AVK and DVA, employing FLP-1 or NLP-12 neuropeptide signaling, respectively. AVK and FLP-1 peptides proved essential for restricting steering and crawling motions, while DVA and NLP-12 peptides promoted crawling motions. Both counter-parts were required for proper switching from travel to local search after the stimulus. AVK appeared as a coordinator of locomotion speed and steering motions, while rises of DVA activity during forward movement were related to increases in crawling wave strength.

In conclusion, crawling and steering waves decomposed from worm body postures appear as meaningful motion patterns, which are coordinated with each other and locomotion speed. Peptidergic interneurons modulate the employment of these patterns to regulate the execution of distinct locomotion strategies. The results support a concept of higher-level organization of locomotion behaviors through superposition of motion patterns generating either regular or flexible motions. This concept suggests that nervous systems might control complex behavioral outputs by combining and coordinating simpler elementary motion patterns.

1.2 Zusammenfassung

Tiere müssen in der Lage sein, ihre Fortbewegungsstrategie zu kontrollieren, um effizient durch die Umwelt zu navigieren. Um effektiv Distanzen zurückzulegen, sind schnelle und regelmäßige Bewegungen von großem Vorteil, während weniger regelmäßige und flexiblere Bewegungen eine gründlichere Erkundung der näheren Umgebung ermöglichen. In meiner Doktorarbeit habe ich die Fragestellung untersucht, wie Tiere ihre stereotypischen und flexiblen Bewegungen koordinieren, um verschiedene Verhaltensweisen wie zielgerichtetes Vorwärtskommen oder lokal begrenzte Suche zu erzeugen und wie sie zwischen diesen Strategien wechseln.

Dazu studierte ich das Fortbewegungsverhalten des Nematoden *C. elegans*, welcher mit regelmäßigen wellenförmigen Bewegungen entlang seines gesamten Körpers vorankriecht. Jedoch ändert der Wurm seine Bewegungsstrategie drastisch, ausgelöst durch sensorische Stimulation (Reduktion der Sauerstoff-konzentration), zu einer erkundenden Suche der näheren Umgebung. Mit einem rechenintensiven Dekompositionsansatz erfasste ich quantitativ die Verhaltensänderungen der Körperwellen des Wurms: Dabei beschrieb ich Wurmbewegungen als zwei parallele überlagerte Bewegungsmuster, die entweder regelmäßige Kriechbewegungen oder flexiblere und unregelmäßige Lenk- /Wende-Bewegungen generieren. Ich zeigte wie die umgekehrte Anpassung der beiden Bewegungsmuster, welche „crawling wave" (Kriechwelle) und „steering wave" (steuernde Welle) genannt wurden, abgestimmt mit der Fortbewegungsgeschwindigkeit den Tieren ermöglichten, ihre Fortbewegungs-strategie nach der Stimulation zu verändern von einem schnellen und zielgerichteten Vorwärtskriechen zu einer lokal begrenzten Suche. Die „crawling wave", welche kräftig war solange die Tiere sich rasch vorwärts bewegten, nahm ab und die Tiere wurden langsamer. Gleichzeitig verstärkte sich die „steering wave", was zu komplexeren Haltungen der Würmer führte und viele Lenk- und Wendemanöver hervorrief, um die örtliche Umgebung zu erkunden.

Um das neuronale Kontrollsystem zu identifizieren, welches „crawling wave" und „steering wave" reguliert, arbeitete ich mit genetischen Manipulationen von Würmer und Kalzium Imaging der neuronalen Aktivität. Dabei konnte ich zwei Klassen von entgegenwirkenden haltungsregulierenden Interneuronen namens AVK und DVA charakterisieren, welche jeweils mithilfe von FLP-1 oder NLP-12 Neuropeptiden Signale weiterleiten. AVK und FLP-1 Peptide erwiesen sich als essenziell um „steering" (steuernde) und „crawling" (Kriech-) Bewegungen zu begrenzen, während DVA und NLP-12 Peptide „crawing" (Kriech-) Bewegungen förderten. Beide Gegenparts dieses

Kontrollsystems wurden benötigt, um nach dem Stimulus einen normalen Übergang vom Vorwärtskriechen zur lokalen Suche herbeizuführen. AVK wirkte als Koordinator zwischen Fortbewegungsgeschwindigkeit und „steering" (steuernden) Bewegungen, während DVA Aktivitätserhöhungen während der Vorwärtsbewegung mit Steigerungen der „crawling wave" Stärke assoziiert waren.

Schlussfolgernd erscheinen „crawling wave" und „steering wave", die durch Dekomposition von Wurmbewegungen erhalten wurden, als sinnvolle Bewegungsmuster, welche miteinander und jeweils mit der Fortbewegungs-geschwindigkeit koordiniert sind. Neuropeptid-sekretierende Interneurone modulieren die Benutzung dieser Muster, um die Ausführung verschiedener Fortbewegungs-strategien zu regulieren. Meine Ergebnisse unterstützen ein Konzept einer übergeordneten Organisation des Fortbewegungs-verhalten in Form einer Superposition von Bewegungsmustern, welche entweder reguläre oder flexible Bewegungen erzeugen. Dieses Konzept legt nahe, wie Nervensysteme komplexe Verhalten möglicherweise mittels Kombination und Koordination einfacherer elementarer Bewegungsmuster kontrollieren.

2 Introduction

2.1 Control of rhythmic animal movements

Movements highly shape the behavioral repertoire of all animals. Locomotion behaviors like walking and swimming are very important forms of rhythmic movement. It is anticipated that most, if not all, rhythmic movements are generated by central neural networks that can organize rhythmic patterns of motor activities even without central or sensory feedback input. These structures are generally referred to as central pattern generators (CPGs). Thus, they do not only underlie locomotion but also rhythmic movements like breathing and feeding, and reflexes like coughing and swallowing (Grillner, 2003; Marder and Bucher, 2001).

Rhythmic oscillations of neural activity can generally arise from two mechanisms. In pacemaker-driven CGPs one or several neurons endogenously generate rhythmic bursts of activity through intrinsic cellular properties and can drive other, non-rhythmic neurons to oscillate themselves. This mechanism is thought to be less common. A prominent example is the pyloric rhythm involved in feeding behavior in the crustacean stomatogastric ganglion (Hooper and Marder, 1987). Another pacemaker-driven rhythm is involved in vertebrate respiration (Smith et al., 1991). The other, more common, mechanism is a network-driven CPG. Rhythms arise from synaptic coupling between non-bursting neurons. The simplest example is a 'half-center oscillator'. Two neurons that show non-rhythmic activity in isolation, fire rhythmically with alternating burst through reciprocal inhibition (Marder and Bucher, 2001). Reciprocal inhibition is in general an important feature of all known CPGs. Well-studied examples of network-driven CPGs comprise the leech heartbeat system (Angstadt and Calabrese, 1991; Calabrese, 1998), the swimming system of the mollusk *Clione* (Satterlie, 1985) and the spinal cord of the lamprey (Grillner, 2003). Generally, CPGs consist of interneurons connected amongst each other and relaying circuit output onto motor neurons. However, there are occasions where motor neurons themselves engage in the CPG circuit activity (Heitler, 1978; Staras et al., 1998).

While some CPGs continuously generate motor output, for example breathing, many CPGs including those for locomotion need to be activated and terminated when necessary. Input into CPGs can be via central descending commands, sensory feedback from the periphery or hormones from neurosecretory structures (Marder and Bucher, 2001). Besides simply turning CGP networks on or off, these inputs can also be important for modulation of CPG activity. Modulation via classical neurotransmitters, biogenic amines and neuropeptides can alter circuit dynamics or

even circuit configurations by affecting membrane properties or synaptic strength of target cells. As a consequence, the same circuit elements can produce different output motor patterns. Moreover, different CPG circuits are often not clearly separable networks, but partially overlap so that some neurons can take part in different CPG circuits and thereby in the generation of different rhythms and motor outputs (Marder et al., 2005).

An intensively studied example of CPG networks is the crustacean stomatogastric ganglion (STG). It consists of ~30 neurons (inter- and motor neurons) and generates two rhythms that regulate feeding motor outputs by controlling several different muscle groups. A fast pyloric rhythm is nearly always active and arises from intrinsic neural properties (pacemaker-driven CPG). A slower gastric mill rhythm is only intermittently expressed and emerges from circuit connectivity (network-driven CPG) and descending input. Thus, the two rhythms can occur in parallel. They can be attributed to distinct sub-circuits, which are however highly interconnected with each other (Marder and Bucher, 2007). At least 20 different modulatory substrates have been identified, all of which evoke changes in motor output. For example, the neuropeptide proctolin, when released from a projection neuron, can activate or strongly enhance a slow pyloric rhythm (Nusbaum and Marder, 1989).

Modulatory input to the pyloric CPG can change the firing of individual neurons relative to the overall phase of the pyloric rhythm (Eisen and Marder, 1984) (modulation of circuit dynamics). Certain neurons of the STG can even fully participate in both sub-circuits (Weimann et al., 1991), i.e. they can switch between the generation of the pyloric and the gastric rhythm and thereby between two feeding motor patterns (modulation of circuit configuration). The switch is under the control of neuromodulatory input and ongoing circuit dynamics (Marder and Bucher, 2007). Interestingly, interactions between the sub-circuits are also active when both rhythms are expressed. Additional examples from different CPG structures and different animals such as the sea hare *Aplysia* (Hurwitz et al., 2003; Morgan et al., 2002) or the leech *Hirudo medicinalis* (Shaw and Kristan, 1997) further illustrate the complexity of overlapping CPG networks: The same neuron class is active during distinct behaviors, such as egestion-ingestion in *Aplysia* feeding behavior, or swimming and whole-body shortening in leech. The activation or inhibition of another neuron class via descending central input or peripheral feedback is involved in the decision between the alternative motor patterns.

Neural rhythms of CPGs drive rhythmically alternating muscle contraction and relaxation. Antagonistic muscle groups can be regulated via the same CPG, when the

respective motor neurons are antagonistically activated and /or inhibited through the generated rhythm (Marder and Bucher, 2001). A certain neural rhythm can thus generate a coordinated motor pattern, while modulation of one neural ensemble can produce different rhythms and therefore various motor patterns. However, more complex motor patterns like locomotion, e.g. when several segments or body parts are involved, might require more complex motor coordination. Animals such as leech or lamprey swim by using left-right alternations of multiple body segments, which produce a wave of body contractions over the length of the animals. Each segment comprises semi-autonomous circuit structures that generate a rhythm, which is similar to that of other segments. For propagating the wave along the body, the segmental rhythms need to be coordinated in a phase-shifted manner. Ascending and descending connections between the segments partially fulfill this. Besides potential contribution of biomechanical properties like stiffness of the body, sensory peripheral feedback via stretch receptors is additionally necessary for proper coordination (Friesen and Cang, 2001; Hill, 2003). In other animals, such as crayfish, central mechanisms dominate the coordination of body segments (the swimmerets) during locomotion. On the contrary, in the multi-legged walking stick insect feedback from the sensory periphery seems to predominantly control coordination of multiple joints per leg or different body segments (Marder et al., 2005). Thus, motor pattern formation for locomotion through coupling of different body parts is controlled to varying degrees by peripheral and central mechanisms in different animals.

Nevertheless, these motor patterns need to be modified according to centrally generated decisions in order to produce voluntary movements and different behaviors: A turn during escape will require a different motor output than straight, forward migration. May it be through diverse modulations of a neural ensemble or through differential coupling /coordination of multiple CPG networks that regulate different body parts. Either mechanism allows the generation of a wide range of different motor outputs and behaviors.

A related view suggests that many body muscles or even their individual motor units (which can be several thousand) need to be coordinated to generate a certain voluntary movement (Bizzi and Cheung, 2013). If every individual motor unit were controlled individually by central neural structures, this would demand rather huge computational efforts. It has been suggested that nervous systems might rather control fewer dimensions in terms of pre-fixed, coordinating patterns of groups of muscles (Sherrington, 1910; Lee, 1984). Central nervous structures would employ various

combinations of these building blocks to produce complex motor programs. On the neural level there is evidence for organization of e.g. spinal cord neurons into neural modules or motor modules (Bizzi et al., 2002). Each of these functional units is thought to encode a specific pattern of muscle activation and generate a particular body movement. This is related to the concept of muscle synergies, which are patterns of relative levels of muscle activation that serve as building blocks to construct complex motor outputs (Bizzi and Cheung, 2013; Tresch and Jarc, 2009;). Several synergies or neural modules, each encoding a certain motion pattern of the body or a body part, can thus be active in parallel. These ideas about higher-level organization of motor behaviors are supported by experimental data:

Studies in mice have recently shown that limb alternation at two different levels of movement speed relies on two separate, genetically distinct subpopulations (modules) of spinal cord interneurons (Bellardita and Kiehn, 2015; Talpalar et al., 2013). Locomotion was not completely abolished after genetic ablation of either or both of the identified subpopulations, but mice could still move in a simpler manner by synchronous movement of their limbs generating a range of different speeds. Possibly, the motion patterns controlling limb alternation are overlaid upon a more simple movement mode that generally provides the drive for locomotion. Similarly, the networks controlling locomotion speed in zebrafish could be deconstructed into three distinct microcircuit modules: Separate interneuronal subclasses drove motoneurons during slow, intermediate, or fast swimming. This means that an increase of speed is achieved by the sequential recruitment of different microcircuit modules (Ampatzis et al., 2014).

Many studies record muscle activities via electromyograms (EMGs) in intact animals performing a task such as walking, swimming or grasping. They then employ computational analyses to identify a set of muscle synergies (relative muscle activation patterns) that well describe the EMG data when combined. Importantly, the synergies can be correlated to task-relevant variables. For example, three synergies derived from 13 muscles measured during frog leg kicking, can be related to distinct functions. While two synergies are mainly responsible for leg movement during the extension phase, with one predominantly controlling hip motions and the other one knee motions, the third synergy is responsible for the flexion phase (d'Avella et al., 2003). Some synergies are shared among different behaviors like jumping, swimming, and walking in frogs while others appear to be rather behavior-specific. Moreover synergies are similar in between different individual animals (d'Avella and Bizzi, 2005). The significance of EMG decomposition into muscle synergies is supported by the finding

that activities of frog spinal cord interneurons are more related to the activation of muscle synergies than to individual muscle activities (Hart and Giszter, 2010).

Studies in a variety of species besides frogs, such as rats (Tresch and Bizzi, 1999), cats (Ting and Macpherson, 2005), primates (Overduin et al., 2008), humans (Torres-Oviedo and Ting, 2007), and also simpler invertebrates as *Aplysia* (Jing et al., 2004) support the concepts of neural modules and muscle synergies as building blocks of motor behaviors. Nevertheless, criticism of these concepts indicates that task constraints or biomechanical limitations of the musculoskeletal system could be the origin of apparent coupling among actually independently controlled muscles (Kutch and Valero-Cuevas, 2012).

Higher central structures (like motor cortical areas in vertebrates) should combine appropriate muscle synergies encoded by neural modules (in the spinal cord), adjusting synergy amplitudes and their temporal sequence, to regulate complex motor outputs. In fact in monkeys, stimulation of a motor cortical area with descending connections to the spinal cord can elicit EMG patterns, which can be decomposed into muscle synergies similar to those extracted during natural grasping behaviors (Overduin et al., 2012).

2.2 Locomotion strategies

Animals control their motion patterns in order to produce various forms of locomotion strategies. For example studies on large mammalian herbivores show how animals switch between strategies such as travelling /relocation and settlement in foraging areas while exploring and selecting their habitat. During foraging, turn angles of animal trajectories are more variable than during relocation periods, indicating sinuous movement versus more directed movement (Fryxell et al., 2008). Similarly, when looking for food, animals generally can change between more local and more global search dependent on food availability: When no information about the location of food is available, straight movement in the form of longer runs is an efficient strategy ('straight-line search') when food is assumed to be distributed in patches. All motile organisms including bacteria and humans employ this strategy (Jander, 1975). When food is likely to be nearby, as indicated for example by information from past experience, animals switch to so-called 'area-restricted search' consisting of short moves and frequent high-angled turns. This behavior is observed in a large variety of animal species including flies, moths, leeches, nematodes, rodents and humans (Bell, 1991; Hills, 2006).

Environmental cues like chemical or light signals can trigger locomotion strategies to cause aggregation at the signal source in the form of chemotaxis or phototaxis. The strategies can be discriminated as kinesis, undirected changes of movement in response to stimulus changes, and taxis, directed movement toward (or away) from the cue (Fraenkel and Gunn, 1961).

During klinokinesis animals change the frequency of undirected turning in response to changes of stimulus concentration. This is often called 'random biased walk'. A prominent example is bacterial chemotaxis. A reduction in the level of the chemical signal induces a tumble that results in a change of direction of the following run (Berg and Brown, 1972). During orthokinesis animals change their locomotion speed in response to stimulus changes. For example, lamprey larvae move more actively and in a non-directional manner in higher versus lower intensities of light (Harden-Jones, 1955). Both forms of kinesis will eventually lead the animals to accumulate at the stimulus source.

In klinotaxis, also called weathervaning, animals adjust the direction of their course in order to move toward or away from the stimulus source. For example fly larvae employ klinotaxis during negative phototaxis, moving away from a light source (Fraenkel and Gunn, 1961; Sawin et al., 1994), or positive chemotaxis toward an odor source (Gomez-Marin and Louis, 2014). It has been shown for odor gradients that larvae continuously bias the direction of forward runs toward the local gradient. Therefore, they wave their head to compare stimulus intensity on both sides and eventually reorient, i.e. turn toward weaker intensity of light (Fraenkel and Gunn, 1961) or higher intensity of odor (Gomez-Marin et al., 2011), respectively. Animals slow down or even stop to perform large head casts to actively sample the environment. Reorientation maneuvers are performed via two alternating motor programs: peristalsis, which generates the forward drive, and asymmetric contraction of anterior body segments, which produces head casts. For completion of the turn the larva returns to peristalsis by straightening its body along the new heading direction (Lahiri et al., 2011). This means that adjusting the coordination of motions along the body is crucial for execution of this klinotaxis locomotion strategy.

Other species, such as rats and also humans, are able to perform related strategies when tracking an odor trail (Khan et al., 2012; Porter et al., 2006). They can follow an odor trail via zigzagging movements along the trail and larger casting movements when they have lost the trail. The rat's zigzagging movements of the nose appear to be generated by motions including the whole body (Khan et al., 2012). The tracking

strategy thus might combine a motion pattern that drives forward movement along to the trail, with a zigzagging pattern that generates the more flexible movement around the trail.

Overall, animals can generate complex and flexible motions to execute different locomotion strategies for exploration of the nearby environment in the presence or absence of sensory cues. In contrast, different, more stereotypic motion types seem beneficial for efficient travel during migration (Barnard, 2004; Domenici, 2000).

To further address how animals coordinate stereotypic and more flexible motions to yield distinct travel or search locomotion strategies, I studied locomotion behavior in the nematode *C. elegans*, which will be introduced in the next section.

2.3 *Caenorhabditis elegans* locomotion

2.3.1 Model organism

Caenorhabditis elegans is a free-living small nematode of about 1 mm length, which can be found in many places around the world and is thought to live in rotting plant materials and in soil, where it feeds on bacteria (Frézal and Félix, 2015). After hatching from its egg, it goes through four larval stages (L1-L4) before it reaches the adult state. In the 1960s and 1970s Sidney Brenner and collaborators initiated the establishment of the worm as a biological model organism (Brenner, 1974). With a completely sequenced and extensively annotated genome of compact size (~100 megabases (C. elegans Sequencing Consortium, 1998)) and techniques at hand to mutagenize or transgenically modify its genome, *C. elegans* is very amenable to genetic studies. The predominant form of reproduction is self-fertilization, as most animals within *C. elegans* populations are hermaphrodites, which greatly facilitates genetic studies. Mating hermaphrodites to males makes targeted crosses easily possible. Due to many detailed gene expression studies, a wide range of promoters with broader or limited expression patterns (including single cell expression) is available and can be utilized to control spatial expression of transgenes. *C. elegans'* rapid reproduction cycle of 3-4 days and simple cultivation conditions (agar plates seeded with *E. coli* bacteria) further promote its popularity as a model organism. Importantly, many of its ~20,000 genes display a high degree of conservation with genes of higher organisms (C. elegans Sequencing Consortium, 1998; Schwarz, 2005). As the nematode does not need to move for feeding or reproduction under laboratory cultivation conditions, it survives diverse manipulations of its genes or cells (especially ablated neurons), which greatly

facilitates investigations of gene and cellular functions.

The nematode has a simple and stereotypic anatomy: Cell number (959 somatic cells) and cell position are constant from individual to individual and the full cell lineage from egg to adult has been characterized (Sulston and Horvitz, 1977; Sulston et al., 1983). As its body is transparent, microscopic studies like those describing the cell lineage are possible in living animals. Likewise, correlates of neural activity can be analyzed in a non-invasive manner in living worms by combining high-magnification fluorescence microscopy with targeted expression of genetically-encoded calcium indicators (GECIs), such as GCaMP, in cells of interest. Engineered GFP (green fluorescent protein) molecules assess intracellular calcium levels, which play essential roles in excitable cells, via direct binding of calcium ions through a C-terminally fused calmodulin protein domain. Thereupon calmodulin can bind to an N-terminally fused M13 peptide (Ca^{2+}-calmodulin binding domain of muscle protein). The associated conformational change evokes a further conformational change of the circularly permutated GFP molecule, which greatly enhances its fluorescence intensity (Nakai et al., 2001). These GECIs are continuously optimized to yield even better sensitivity, dynamic range, baseline fluorescence levels, photostability, calcium affinity and binding kinetics (Akerboom et al., 2012; Chen et al., 2013).

Compared to its small size and anatomical simplicity, *C. elegans* displays a relatively rich behavioral repertoire including mating, navigation and foraging (including the detection of a wide range of sensory cues), egg-laying, escape and avoidance, and even some forms of learning (de Bono and Villu Maricq, 2005). Sophisticated tracking methods have been developed within the research community to automatically track and analyze behavior (especially locomotion behaviors) (Chalasani et al., 2007; Cronin et al., 2005; Ramot et al., 2008; Yemini et al., 2013). These can be combined with simultaneous investigation of neural activity correlates or behavioral manipulation via optogenetics (Faumont et al., 2011; Kocabas et al., 2012; Leifer et al., 2011; Piggott et al., 2011). For the above-mentioned characteristics and further reasons explained in the next section, *C. elegans* is a very powerful and popular model organism for neurobiology and the study of the neural basis of behavior.

2.3.2 Neurobiology of *C. elegans*

A major strength of *C. elegans* as a neurobiological model organism is its compact and stereotypic nervous system of 302 neurons and 95 body wall muscle cells. The complete structure and synaptic connectivity of the nervous system have been mapped through reconstructions from serial electron micrographs (Ward et al., 1975;

White et al., 1986). There are 118 neuron classes based on similar morphology and connectivities, with each class comprising between one and 13 members. After recent re-evaluation of the connectivity data, the wiring diagram of *C. elegans* comprises 6393 chemical synapses, 890 gap junctions and 1410 neuromuscular junctions (Varshney et al., 2011). These numbers refer to the 282 somatic neurons, which means excluding the 20 neurons of the pharyngeal nervous system, which is independent from the somatic nervous system. There is only one interneuron pair (RIP) connecting the two systems. Many neurons are part of bilaterally symmetric pairs, which often function similarly. However, some pairs have been shown to fulfill distinct properties, e.g. the sensory neuron pair ASE displays asymmetries in gene expression, ion preference and neural responses to ion concentration changes (Pierce-Shimomura et al., 2001; Suzuki et al., 2008; Yu et al., 1997). The cell bodies of the nematode's neurons are organized into several ganglia situated mostly in the head but also in the tail. There are only few synapses within the ganglia, but neural processes are sent out from ganglia into longitudinal nerve bundles, where most synapses are formed and which are connected via dorsoventral commissures. The largest commissural region is the so-called nerve ring situated in the head of the worm, into which 180 neurons project processes. The main longitudinal nerve bundle is the ventral nerve cord (VNC), which runs from the head to tail at the ventral body side and contains also cell bodies of the VNC motor neurons. Neurons are small and have simple morphologies with mostly one or two unbranched processes (White et al., 1986).

The nematode's sensory neurons often respond to several different sensory cues (Bargmann, 2006). Many are recurrently connected indicating additional interneuron functions and are believed to themselves fulfill a high degree of processing to transform sensations into behaviors (Izquierdo and Lockery, 2010; Suzuki et al., 2008; Thiele et al., 2009). The sensory neurons signal further to interneurons, which can be classified into layers based on their connections: Primary or first-layer interneurons directly receive information from the sensory neurons and signal to secondary or second-layer interneurons, which are mostly connected to other interneurons (Gray et al., 2005; Tsalik and Hobert, 2003). Neurons from both layers are highly interconnected and further signal directly or indirectly, via a small set of pre-motor interneurons, to motor neurons.

There are 113 motor neurons, most of which innervate the 95 body wall muscle cells (besides pharyngeal muscle, egg-laying and defecation musculature). Head motor neurons are situated around the nerve ring, into which they send their neural

processes and to which most synaptic inputs and outputs are confined. Many head motor neurons synapse also onto other neurons, i.e. additionally function themselves as interneurons. Ventral cord motor neurons have their cell bodies and processes (or portions thereof) within the ventral nerve cord (details about VNC motor neuron classes and their connections in section 2.3.4). The muscle cells are organized into circumferential quadrants of anterior-posterior running rows of 24 or 23 longitudinal muscle cells, arranged in interleaved pairs. Two quadrants or 4 muscle cells per section align to both the dorsal and ventral body wall. The 16 anteriormost muscle cells (head muscles) receive innervation exclusively from head motor neurons. The neck muscles are composed of the following 16 muscle cells and receive innervation from both head and VNC motor neurons. The remaining 63 body muscles receive input only from VNC motor neurons. Notably, the worm lies on its left or right side. Due to more complex wiring of head motor neurons onto head and neck muscles, the worm's head can move laterally in addition to the dorso-ventral plane. Body movements are only possible in dorsoventral directions (White et al., 1986; 1976).

The chemical synapses are formed as axonal swellings *en passant* between adjacent processes. For neuromuscular junctions, muscles extend long, thin processes to synapse onto the motor neuron processes (Altun and Hall, 2011). The classical transmitters glutamate, acetylcholine and GABA and the monoamines serotonin, dopamine, tyramine and octopamine are employed. Receptors, synthesis and release pathways of neurotransmitters are highly conserved between *C. elegans* and mammals (Bargmann, 1998). Electrical synapses via gap junctions are made out of so-called innexins proteins (25 different members), which have a distinct origin than 'connexin' proteins building gap junctions in mammals, but are more related to vertebrate 'pannexin' proteins (Altun et al., 2009; Phelan and Starich, 2001; Starich et al., 1996). *C. elegans* contains over 200 potential neuropeptides encoded by over 100 genes belonging to FMRFamide-like peptides FLP, insulin-like peptides INS, or remaining neuropeptide-like proteins NLP (Li et al., 1999; Nathoo et al., 2001; Pierce, 2001). As in other animal species these short peptide sequences can act as modulatory co-transmitters or potentially primary transmitters at synapses, or signal extra-synaptically through local or broader diffusion. These molecules therefore have the potential to superimpose a wireless network onto the existing wiring diagram.
Most *C. elegans* neurons are probably (nearly) isopotential and employ graded synaptic transmission. They do not fire classical sodium-dependent action potentials, consistent with the absence of voltage-gated sodium channels in the nematode's genome, but rather employ voltage-regulated calcium and potassium currents

(Bargmann, 1998; Goodman et al., 1998; Lindsay et al., 2011). Related to that, neurons of the larger nematode *Ascaris* display calcium-based signal amplification, but no sodium-dependent action potentials (Davis and Stretton, 1989). Based on these characteristics and the fact that calcium is needed for synaptic vesicle release, using calcium indicators as a correlate for neural activity appears reasonable. While the transmission at neuromuscular junctions is also reported to be graded (Liu et al., 2009), muscle cells can fire calcium-based all-or-none potentials (Gao and Zhen, 2011; Liu et al., 2011b), the synchronization of which depends on electrical coupling of the muscle cells (Liu et al., 2011a).

2.3.3 Locomotion states and strategies

C. elegans moves by generating thrust via sinusoidal undulations along its body against the direction of locomotion. While lying on its side, it generates dorsoventral body bends through alternating contractions of its ventral or dorsal longitudinal body wall muscles. A full undulation cycle takes at about 2.5 s when it moves off food and produces an average speed of 0.15-0.2 mm/s (Cronin et al., 2005). The worm predominantly moves head-first in forward direction with undulations passing from head to tail. But it can also move tail-first in reverse direction with undulations passing from tail to head; this movement is termed reversal. Besides these two movement states the worm also exhibits pause or quiescence states (Gallagher et al., 2013; Stephens et al., 2011a). Reversals usually end with resumption of forward movement into a new direction. To achieve this the worm changes its heading direction via changes in body posture. Deep bends of the head towards the tail during forward movement are termed omega turns (as their shape resembles the Greek letter Ω) or referred to as turning in the course of this study. These deep turns are mostly directed toward the ventral side (Gray et al., 2005). Subtler directional changes are achieved through biases in bending strength between the ventral and dorsal side during one or several subsequent undulation cycles (Kim et al., 2011). This is referred to as shallow turn or in the course of this study as steering. It appears to be the most frequent reorientation maneuver (during locomotion off food). Reversals together with subsequent changes of heading direction are often referred to as reorientation maneuvers. Turning and especially steering also occur in the absence of a preceding reversal during continuous forward locomotion.

C. elegans exhibits a range of locomotion states or strategies to move through its environment with or without sensory cues. These are based on the control of forward and reverse movement, turning and steering. It performs chemotaxis to a variety of

odorants and tastants, aerotaxis in oxygen or carbon dioxide gradients and thermotaxis toward preferred temperature (of previous cultivation). It therefore can employ several chemotaxis strategies:

When moving up (or down) a spatial gradient of an attractive stimulus, animals increase (decrease) the duration of forward movement (runs) by down- (up-) regulating stochastically occurring turning events, so-called pirouettes. These are bursts of reversals and omega turns in close succession (reorientation maneuvers). The klinokinesis strategy biases movement towards favored environments as it interrupts runs in the non-favored direction and prolongs runs in the favored direction. It is employed for a variety of different stimuli such as tastants and temperature (Pierce-Shimomura et al., 1999; Ryu and Samuel, 2002). It is often referred to as biased-random walk, although *C. elegans* navigates more sophistically than bacteria (Berg and Brown, 1972). The nematode can regulate the frequency of pirouettes in both directions depending on the sign of the concentration change. Moreover, the directional changes caused by pirouettes are not completely random but display forms of course corrections (Pierce-Shimomura et al., 1999). Opposite adjustments drive worms away from a repelling sensory cue (avoidance behavior).

The up- or down-regulation of pirouettes is also observed when *C. elegans* is stimulated with temporal step changes. Odor stimuli or odor removal evoke down- or up-regulation of reversals and omega turns, respectively (Albrecht and Bargmann, 2011). Similarly, increased omega turns and /or reversals occur after oxygen downshift (Zimmer et al., 2009), oxygen upshift (Cheung et al., 2005) or carbon dioxide upshift (Bretscher et al., 2008).

While executing forward runs within spatial gradients, worms also make course corrections, which are subtler than the strongly reorienting omega turns or pirouettes. Through continuous weak bias of dorsoventral undulatory bending or rarely, abrupt heavily biased bends, worms adjust the heading direction toward the line of steepest ascent and can steer towards the source of a gradient (Iino and Yoshida, 2009). This is the so-called weathervaning strategy or klinotaxis. It has been studied within salt and odorant gradients (Iino and Yoshida, 2009) and contributes also to thermotaxis in the form of isothermal tracking (Hedgecock and Russell, 1975; Luo et al., 2006). Active orienting via weathervaning seems to arise from active sensing of stimuli during head sweeps associated with sinusoidal locomotion in the order of seconds (Izquierdo and Lockery, 2010; Kocabas et al., 2012). It contributes majorly to navigational adjustments when the animals move perpendicular to the gradient direction and then serves to align the worms along the gradient direction. Thus, strongest changes of

heading direction during forward runs are associated with an orthogonal alignment of worm heading direction and gradient direction (Iino and Yoshida, 2009). In contrast, the regulation of pirouette frequency relies on temporal sensory integration over about a minute and especially causes orientation changes when animals move parallel to the direction of the gradient (Pierce-Shimomura et al., 1999).

C. elegans also adjusts its locomotion speed in response to stimulation. The orthokinesis strategy has been less well studied within spatial gradients, but has been reported not to contribute to tastants chemotaxis (Pierce-Shimomura et al., 1999; Iino and Yoshida, 2009). However, worms clearly down-regulate their speed in response to step-like stimuli: Odorant removal causes transient slowing (Albrecht and Bargmann, 2011), encounter of a food patch evokes long-lasting speed reductions (Sawin et al., 2000) and decreases in ambient oxygen concentration trigger transient slowing responses (Cheung et al., 2005; Zimmer et al., 2009).

Oxygen levels are believed to be important for *C. elegans'* navigation, as local reductions could indicate the presence of bacteria food due to oxygen consumption by bacteria. In line with that, *C. elegans* avoids atmospheric levels of 21% oxygen and displays a preference for intermediate oxygen levels when placed in a gradient (Gray et al., 2004). Thus it seems conceivable that worms would slow down in order to locate a nearby food source when encountering lower oxygen levels. In the wild type laboratory strain N2, oxygen decreases are sensed and transferred into behavioral changes by the sensory neuron pair BAG (Zimmer et al., 2009). This sensory pathway together with a paradigm of decreasing oxygen levels was used in the current study to investigate postural changes during stimulus-evoked changes in worm locomotion.

The presence or absence of food greatly influences *C. elegans* locomotion behaviors. On food, the nematode (wild type laboratory strain N2) moves generally slower than off food. On encountering a food patch, well-fed worms slow down, which is termed 'basal slowing response'. After about >30min of food deprivation the reduction in speed is even greater, termed 'enhanced slowing response' (Sawin et al., 2000).

In the absence of additional sensory stimuli, *C. elegans* spontaneously alters its locomotion behavior when moving on food. It frequently switches between two behavioral states, referred to as dwelling and roaming. Dwelling consists of especially slow movement with a high level of reorientation maneuvers (mainly reversals) and therefore displays very low displacement. Roaming describes faster movement along straighter paths with few directional changes and leads to greater displacement, which promotes movement in between food patches. Usually animals spend most time

dwelling. But when food is limited or of low quality, the time spent roaming increases, implicating that decisions about behavioral switches are under the environmental influence (Ben Arous et al., 2009; Fujiwara et al., 2002). Roaming and dwelling behaviors can last several minutes; they end with abrupt transitions and are thought to represent discrete states. However, a recent modeling study suggests that *C. elegans* on-food behaviors are not limited to discrete roaming and dwelling states, but that intermediate states also occur (Gallagher et al., 2013).

Upon removal from food *C. elegans* probes the nearby environment through forward bursts with enhanced locomotion speed and up-regulation of reversals and turns (Gray et al., 2005; Hills, 2004; Wakabayashi et al., 2004). In analogy to similar locomotion patterns in other organisms, this is referred to as area-restricted search or local search (Bell, 1991). It is related to klinokinesis during chemotaxis as a non-favored environmental change induces an up-regulation of pirouettes. Animals employ this strategy due to the recent experience of food in their environment and the associated probability to find another food source nearby. But if no food is found after a while (15-30 minutes), worms change their locomotion strategy toward long-range dispersal behavior to find food in other, more distant areas. This consists of fast and straight movement with suppression of reorientation events (reversals, omega turns). While the frequency of pirouettes adapts rapidly after a sensory stimulus during chemotaxis, it falls much more slowly after removal from food (Gray et al., 2005; Hills, 2004; Wakabayashi et al., 2004).

C. elegans is also capable to swim in liquids with distinct movement kinetics compared to crawling on food. Undulations have longer wavelengths of about 1.5 worm lengths (crawling wavelength = 0.6 worm lengths), increased bending frequencies of 1.7 Hz (crawling 0.3-0.4 Hz) and decreased wave amplitudes (Fang-Yen et al., 2010; Pierce-Shimomura et al., 2008). Worm postures during swimming are C-like shapes, whereas crawling postures are more S-like shapes. Due to these differences and the abrupt transition between the two movements when entering or exiting fluids, crawling and swimming were originally thought to represent to distinct gaits (with potentially two distinct underlying neural circuits) (Pierce-Shimomura et al., 2008; Vidal-Gadea et al., 2011). Yet, other studies propose that crawling on dry surfaces and swimming in liquids are extremes of a single gait, which is defined by the mechanical load of the environment. Media of gradually increasing viscosity or gradually elevated confinement result in a smooth transition of the worms' locomotion pattern from swimming to crawling (Berri et al., 2009; Lebois et al., 2012).

2.3.4 Neural circuits generating undulatory locomotion

To date, how *C. elegans* generates neural rhythm(s) and transforms it (them) into patterned and coordinated undulatory locomotion is not resolved. However, the wiring diagram together with neuronal ablations and imaging experiments and along with computational models have shed light onto features of the nematode's 'locomotion circuits'. There are reasons to believe that two distinct locomotion circuits exist, one in the head situated around the nerve ring and the other one located in the ventral nerve cord (VNC). As mentioned in section 2.3.2, the motor neurons of these circuits have distinct muscle output fields to head-neck (nerve ring) or neck-body muscles (VNC), respectively. Furthermore, synaptic connections in the nerve ring circuit (where many motor neurons show interneuron-like wiring) are more complex than between the recurrently connected VNC motor neurons (Gray et al., 2005; White et al., 1976). Consistently, the head can perform more complex motions, i.e. bend in 3D, while the body bends only in 2D. With the control of >80% of the entire body length (Chen et al., 2006), the VNC locomotion circuit is anticipated to be the main origin of the sinusoidal wave that generates thrust for progression. Current understandings of the VNC circuit functions will be summarized here. The contribution of the nerve ring circuit to locomotion control will be explained in the next section.

C. elegans has 8 different classes of ventral cord motor neurons based on morphology and synaptic connectivity. While all cell bodies reside on the ventral side of the worm body, a part of the neurons sends commissures into the dorsal nerve cord to form neuromuscular junctions (NMJ) with dorsal body wall muscles. These are DA, DB, DD (D stands for dorsal) and AS neurons. NMJ with ventral body wall muscles are built by VA, VB, VD and VC (V stands for ventral) neurons (White et al., 1986). Each class comprises 6-13 members that are distributed along the nerve cord (12 VA, 9 DA, 11 VB, 7 DB, 13 VD, 6 DD, 11 AS, 6 VC). Within each class, the muscle output regions are evenly distributed along the body and barely overlap (White et al., 1976).

Most VNC motor neurons (VA, DA, VB, DB, AS, VC) are cholinergic and form excitatory NMJs, while D-type neurons (DD and VD) use GABA as inhibitory neurotransmitter at NMJs (Duerr et al., 2008; McIntire et al., 1993; Rand and Nonet, 1997). Thus, muscle contraction is induced or inhibited by cholinergic or GABAergic inputs, respectively, which regulate firing of action potentials in muscle cells (Liewald et al., 2008; Liu et al., 2013). Muscle calcium levels and muscle contraction have been shown to be consistent, however with a delay between maximum calcium level to maximum bend (Pierce-Shimomura et al., 2008, Butler et al., 2014).

The excitatory VNC motor neurons with ventral and dorsal members evoke contraction

of body wall muscles and can be distinguished based on their morphology into A-type and B-type motor neurons: A- or B-type neurons extend their axonal processes forming the NMJs anteriorly or posteriorly, respectively. The neural processes extend further distally beyond the synaptic regions without any detectable morphological specialization (White et al., 1986). A- and B-type neurons can further be distinguished based on their major synaptic inputs from a set a few pre-motor interneurons, frequently referred to as "command neurons": the left-right pairwise neurons AVA, AVB, AVD, AVE (in the head) and PVC (in the tail). These interneurons send long processes along the ventral nerve cord. A-type neurons receive input from AVA (electrical and chemical synapses), AVD (chemical synapses) and AVE (chemical synapses). B-type neurons receive input from the head neuron pair AVB (electrical synapse) and the tail neuron pair PVC (chemical synapses). The left-right cells of each pair are highly coupled to each other by electrical synapses while different pre-motor interneuron classes are interconnected by chemical and electrical synapses (White et al., 1986).

The inhibitory D-type motor neurons extend their neural processes both anteriorly and posteriorly along the nerve cord to form NMJs and receive input only from other VNC motor neurons: VD (DD) neurons inhibiting ventral (dorsal) muscles receive input on the dorsal (ventral) side from excitatory DA and DB neurons (VA and VB) (White et al., 1986; 1976). Thus D-type motor neurons could provide cross-inhibition within the VNC motor control system, inhibiting ipsi-lateral muscles while contra-lateral muscles are being activated.

Gap junctions connect adjacent members of the same motor neuron class and body wall muscles in each row. Reexamination of the original *C. elegans* connectivity data (Chen et al., 2006; Varshney et al., 2011) revealed many additional gap junctions and chemical synapses between different VNC motor neuron classes. These include inhibitory inputs from D-type neurons onto excitatory B-type neurons or inhibitory D-type neurons and excitation of D-type neurons through B-type neurons of the same side of the body. Overall, the VNC circuitry appears to be equipped for some forms of circuit computations.

The ventral excitatory VC motor neurons innervate vulval muscles and are involved in egg-laying (VC4-5) (Weinshenker et al., 1995; White et al., 1986). They (VC1-3) also make connections with body wall muscles and with other VNC motor neuron classes especially VD and DD neurons in the anterior body half (Haspel and O'donovan, 2011) and might be involved in relaxing the anterior body half of the worm. Excitatory AS neurons innervate dorsal muscles and display similarities to DA neurons with anteriorly

directed processes, which are however shorter. They further synapse onto VD neurons and have gap junctions with VA, DA and AVA neurons and receive input from all pre-motor interneuron classes (White et al., 1986; 1976). Both AS and VC neurons have not been studied extensively and have no assigned function in locomotion by now.

Forward and backward locomotion in the nematode seem to rely on two largely distinct circuits, which is founded on (the just described) neural structure and connectivity patterns, studies of manipulated worms and calcium imaging of neural activities. B-type motor neurons are believed to excite muscles during forward movement to generate anterior-posterior travelling body waves, which is consistent with their posteriorly directed neural processes. They receive activating input from the pre-motor neurons PVC and especially AVB. During backward locomotion, A-type motor neurons provide excitatory input onto muscles to produce posterior-anterior traveling body waves, which is consistent with their anteriorly directed processes. They are activated via the pre-motor interneurons AVD, AVE and especially AVA. When A- or B-type motor neurons are ablated in the first larval state L1 (when only DA and DB but not VA and VB motor neurons are developed), animals are selectively incapable of moving in forward or reverse direction, respectively, while locomotion in the other direction is normal (Chalfie et al., 1985). When DD neurons are ablated (which innervate rather ventral than dorsal muscles at L1, while VD are not fully developed yet), animals move in a severely uncoordinated manner in both directions. Studies of animals at later life stages and thus on the ventral counterparts have not been done yet. However, based on their corresponding morphology and connections, VA and VB motor neurons are thought to take comparable roles during reverse or forward movement. D-type neurons seem rather dispensable for movement (at least in forward direction) during later life stages than L1, as their ablation or defective GABA synthesis does not cause impairment thereof (McIntire et al., 1993).

An interesting support for the control of directional movement via two distinct VNC modules comes from mutations causing defective wiring: Worms mutant in *unc-4* do not have functional VA neurons as these are innervated by AVB and PVC (instead of AVA, AVD, AVE) and cannot move backwards (White et al., 1992). Worms mutant in *vab-7* do not have functional DB neurons as these send their neural processes anteriorly like DA neurons instead of posteriorly. This causes uncoordinated movement in forward direction (Esmaeili et al., 2002).

Ablation of AVB or AVA pre-motor interneurons causes highly uncoordinated movement selectively into forward or reverse direction, respectively. Ablation of PVC

or AVD alone does not impair spontaneous movement but forward or reverse movement in response to touch. Combined ablation of AVB and PVC, or AVA and AVD completely abolishes undulatory body movement in forward or reverse direction, respectively (Chalfie et al., 1985). Due to its similar anatomy to AVD and the synapses onto A-type motor neurons, AVE is thought to act as another pre-motor interneuron important for reverse movement.

Calcium imaging of neural activity could confirm assigned roles of neuron classes within the locomotion circuits. B-type motor neurons display increases in calcium levels upon switches from backward to forward movement, while A-type neurons display a decrease in calcium. The opposite case is true for switches from forward to reverse movement (Haspel et al., 2010). While another study showed that both A- and B-type motor neurons have calcium oscillations during both directions of movement with ventral (dorsal) neurons active during ventral (dorsal) bends (Faumont et al., 2011), a third study revealed an imbalance of A- and B-type neurons as the basis of directional movement (Kawano et al., 2011): During forward (reverse) locomotion, B-type neurons have higher (lower) calcium levels than A-type neurons. The reciprocal activity change evokes the directional change. The activity of pre-motor interneurons also matches their assigned functions in locomotion. AVA and AVE neurons display rises in calcium levels upon switches to backward movement, while AVB neurons show increases upon switches to forward locomotion (Ben Arous et al., 2010; Faumont et al., 2011; Kato et al., 2015; Kawano et al., 2011; Piggott et al., 2011).

Overall, the two described locomotion circuits mediate the execution of forward and backward undulatory locomotion. However, where the rhythmically alternating dorsoventral bends are initiated and how they are propagated into a coordinated wave pattern along the body is not solved. Both features could be achieved via either central pattern generators (CPG) or sensory feedback. A CPG is an autonomous feed-forward generator of rhythmic, patterned neural output underlying locomotion in all animals investigated so far (Marder and Bucher, 2001). *C. elegans'* undulatory movement could rely on a CPG in the worm's head: The neural circuitry in the worm's head is suggestive of containing a CPG (Cohen and Sanders, 2014) and a detailed model based on the head circuitry of 41 neurons produces practical head oscillations (Sakata and Shingai, 2004). This idea is further supported by the fact that animals can slowly move forward solely via the head motor system when all pre-motor interneurons have been manipulated (Kawano et al., 2011; Zheng et al., 1999). Therefore and due to the

fact that activities of pre-motor interneurons are tonic and do not oscillate in the range of dorsoventral alternations (Faumont et al., 2011; Kawano et al., 2011), these neurons can be excluded as rhythm generators despite their promising connectivity to all forward or reverse module VNC motor neurons. It is moreover unlikely that the pre-motor interneurons provide sequential input to motor neurons along the length of the body to control muscular wave propagation: Transmission of the electrical signal along the interneurons' neural processes is predicted to be much faster than the muscular body wave (Niebur and Erdös, 1993).

Rhythmic locomotion could also arise within the VNC motor neurons themselves. The A- and B-type neurons display oscillatory activities correlating with dorsoventral bending (Faumont et al., 2011; Kawano et al., 2011) and VNC neurons are locally wired within a distributed and recurrent architecture, which has the potential to endogenously produce local rhythmic patterns (Haspel and O'donovan, 2011). This could be a similar mechanism as in leech and lamprey, which are however, in contrast to *C. elegans*, segmented animals (Friesen and Cang, 2001).

The inhibitory D-type motor neurons are thought to provide cross-inhibition within the VNC motor system based on their wiring (White et al., 1986). This could potentially coordinate dorso-ventral undulations: e.g. signals activating dorsal muscles contraction can simultaneously indirectly, through the activation of D-type neurons, evoke relaxation of ventral muscles, altogether making a dorsal bend possible. Consistently, mutant animals with defective GABA synthesis are not able to coordinate ventral and dorsal contraction in response to touch stimuli. Instead of reversing, animals shrink by simultaneous contraction of ventral and dorsal muscles (McIntire et al., 1993). The neural activity of D-type motor neurons has not been investigated in *C. elegans*, but their correlates in the nematode *Ascaris* display oscillatory activities (Angstadt and Stretton, 1989). Despite their engagement in local feedback circuits, D-type neurons are unlikely to be the source of the locomotion rhythm; the motif of reciprocal inhibition necessary for network-based CPG activity is absent from the ventral cord circuitry. Moreover, GABAergic transmission is dispensable for sinusoidal wave generation, but involved in the regulation of wave amplitude (McIntire et al., 1993).

Oscillations could also arise from the body wall muscles themselves. They display spontaneous calcium-based action potentials when devoid of synaptic input (Liu et al., 2011a). Thus, despite having severe locomotion defects, animals without cholinergic and GABAergic transmission are still capable of some locomotion (Francis et al., 2005; Touroutine et al., 2005), suggesting that body wall muscles themselves can produce some coordinated motions without neural inputs.

Gap junctions between motor neurons of the same class or between muscle cells could be involved in the wave propagation. However, when the main gap junction proteins (*unc-7, unc*-9) in the worm nervous system are defective, anteriorly traveling waves persist and generate continuous reverse movement. Moreover, the inability of generating coordinated posteriorly traveling waves necessary for forward movement can be re-established by reducing A-type motor neuron activity without restoring the electrical coupling. Thus, gap junctions between AVA and A-type motor neurons seem essential for forward movement via reducing AVA activity through shunting mechanism (Kawano et al., 2011). However, electrical coupling is not essential for initiating and propagating the traveling waves.

Sensory feedback is implicated in the regulation of the worm's sinusoidal motions and could potentially propagate bends along the body or participate in the generation or modulation of locomotion rhythms. In general, CPGs are under the control of inputs the sensory periphery (Friesen and Cang, 2001). *C. elegans* A- and B-type motor neurons possess long undifferentiated processes extending distally beyond the synaptic zones. They are in close association with the body wall and have been suggested to function as stretch receptors providing sensory feedback about body bending (proposed by Russell and Byerly, cited in (White et al., 1986)). These processes extend anteriorly or posteriorly in the case of backward A-type or forward B-type motor neurons, respectively. Neural models incorporating sensory feedback via stretch receptors located posterior to the contracting muscle have yielded good representations of anterior-posterior wave propagation during forward movement (Niebur and Erdös, 1991) and generation of dorsoventral rhythmic bending (Bryden and Cohen, 2008). These sensory feedback-driven representations of nematode crawling behavior can be extrapolated to produce a range of robust undulatory motions during the continuum between (forward) crawling and (forward) swimming (Boyle et al., 2012). Another mechanical model suggests the implementation of short-range anterior proprioception (via shorter dendritic processes) of B-type motor neurons during forward movement in the propagation of rhythmic bends (initiated by a head oscillator) and the adjustment of undulations to the environmental viscosity (Wen et al., 2012).

Sensory feedback onto the locomotion circuits might involve proprioception via the single interneuron DVA, which is situated in the tail of the worm and sends a process along the entire VNC into the nerve ring. DVA calcium levels have been reported to reflect dorso-ventral body bending of tail-glued animals in a proprioceptive manner. This is dependent on the transient receptor potential protein (TRP) *trp-4*, which is the pore-forming subunit of a stretch- sensitive channel (Kang et al., 2010; Li et al., 2006).

DVA therefore might be sensitive to overall body curvature and transmit this signal via a small number of synapses onto A- and B-type VNC neurons. Mutation of *trp-4* cause increased wave amplitude of body undulations and this effect can be rescued by specific expression in DVA. Ablation of DVA, however, causes the opposite phenotype, a reduction of wave amplitude. In both cases, animals can generate traveling waves and perform forward and reverse locomotion. DVA releases NLP-12 neuropeptides which leads to increased synaptic transmission at cholinergic neuromuscular junctions and promotes locomotion speed and body wave amplitude (Bhattacharya et al., 2014; Hu et al., 2011; Janssen et al., 2008). This pathway could provide sensory feedback about body bending and serve to maintain motor neuron and locomotory activity. However, it is not essential for rhythm initiation or wave propagation.

2.3.5 Regulation and neuromodulation of locomotion

The previous section highlights the major known facts about the *C. elegans* neural systems generating body undulations important for thrust production and progression (in forward and reverse direction). The exact mechanisms initiating the rhythmically alternating bends and producing the wave pattern along the body are not solved. A great part of work on *C. elegans* locomotion has focused on the regulation of switches between locomotion in forward and reverse direction. Less is known about the motor control mechanisms of steering and turning maneuvers during forward movement However, important pathways including neurons and signaling molecules that regulate /modulate undulatory worm movement to control locomotion strategies, are increasingly becoming evident.

Consistent with the finding that the activity of many inter- and motor neurons reflects directional changes, neuronal manipulations (in addition to those of pre-motor interneurons described in the previous section) reveal instructive functions in directional control for interneurons directly downstream of sensory neurons, such as AIZ, AIY, AIA, AIB and RIB (Chalasani et al., 2007; Kato et al., 2015; Kawano et al., 2011; Li et al., 2014; Schrödel et al., 2013; Tsalik and Hobert, 2003; Wakabayashi et al., 2004). Based on these studies, a subset of inter- and motor neurons can be classified into interneurons promoting either forward movement (runs) or reorientation maneuvers (reversals or omega turns) (Faumont et al., 2012). The AIY interneuron pair promotes forward run duration and locomotion speed and suppresses reorientations, while its neural activity reflects the animal's speed during forward locomotion. It relays signals onto AIZ and RIB interneurons. AIZ promotes reversals

while RIB promotes forward movement and locomotion speed, and reflects forward speed similarly to AIY. Similar to AIZ, AIB neurons promote reorientations and inhibit run duration, while AIA suppresses reorientations.

Interestingly, a big portion of the *C. elegans* nervous system reflects and might be involved in the switches between forward and reverse movement (Schrödel et al., 2013; Kato et al., 2015). This regulation is essential for klinokinesis (Pierce-Shimomura et al., 1999) and proper execution of locomotion strategies such as local search vs. dispersal off food or roaming vs. dwelling on food (Gray et al., 2005; Tsalik and Hobert, 2003; Wakabayashi et al., 2004).

Area-restricted or local search after removal from food involves the sensory neurons AWC (sensitive to odorants) and ASK (sensitive to tastants), which are both activated upon removal of food. Both neurons stimulate the AIB interneurons resulting in an increase of reorientations (reversals and omega turns). AIY neurons are suppressed via AWC during that time. The dispersal behavior after 15-30 minutes off food is based on a release of AIY suppression and inhibition of AIB, resulting in longer runs and reduction of reorientations (Gray et al., 2005; Wakabayashi et al., 2004). This is mediated partially via the ASI sensory neurons that signal increasing starvation via the monoamine serotonin and a TGF-*β* molecule (Ren at al., 1996; Sawin et al., 2000).

Furthermore, regulation of area-restricted search after food removal involves dopamine from the dopaminergic sensory neurons ADE, PDE and CEP (Hills, 2004; Sulston et al., 1975). The dopaminergic signaling has been proposed to enhance glutaminergic signaling, possible at the pre-motor interneurons, to promote reversals and high-angle turns (Brockie et al. 2001; Hills, 2004). Dopamine might also extra-synaptically regulate excitatory and /or inhibitory VNC motor neurons, which express the dopamine receptors *dop-1* and *dop-3* (Chase et al., 2004). This pathway has been shown to be important for the opposite paradigm, when animals encounter food ('basal slowing response'). Here, dopamine is secreted when the sensory neurons mechanically sense the presence of food dependent on the mechano-sensitive channel *trp-4* (Kang et al., 2010; Li et al., 2006). This likely induces slowing by activating DOP-3 receptors on excitatory VNC motor neurons, which causes a decrease in cholinergic transmission at the neuromuscular junctions. However, this pathway can be antagonized by the DOP-1 receptor within the same cholinergic cells increasing cholinergic NMJ signaling. Moreover DOP-3 receptor activation on inhibitory VNC motor neurons could also induce slowing (Allen et al., 2011; Chase et al., 2004). Given this complex signaling pathways, dopamine signaling might take part in both reduction of speed when encountering food and increasing turning when leaving food

by altering synaptic transmission at the VNC NMJs. However, it is unclear how dopamine secretion is evoked by both the encounter and sudden absence of food.

Another possible target of dopaminergic signaling is the DVA interneuron. It expresses the receptor *dop-1*, receives many synaptic inputs from the dopaminergic sensory neurons PDE, and stimulation via dopamine increases its secretion of NLP-12 peptides (Bhattacharya et al., 2014). NLP-12 signaling is important for up-regulation of the body amplitude and high-angle turning after removal from food and also promotes locomotion speed off food (Bhattacharya et al., 2014; Hu et al., 2011) which could explain the increased speed generally observed after removal from food (Gray et al., 2005). These effects might be exerted via increasing cholinergic transmission at NMJs (synaptically or extra-synaptically), but DVA also connects to nerve ring interneurons such as AVA, AVE, AVB, AIZ involved in the regulation of reversals and turning. The *nlp-12* dependent pathway or the direct dopaminergic signaling onto VNC motor neurons could serve to maintain a steady speed level. The mechano-sensitive PDE neurons have neural processes along the entire body length and are proposed to become stimulated during worm movement to secrete dopamine (Omura et al., 2012).

As described in section 2.3.3, worms switch between roaming and dwelling states on food by controlling reorientations, which are mainly reversals. The regulation of the transition between the two states depends on extra-synaptic modulation. The monoamine serotonin promotes dwelling behavior, while PDF neuropeptides (pigment dispersing factor) support roaming behavior (Flavell et al., 2013). Interestingly, motor neurons are the source of serotonin and interneurons the source of PDF. The two modulators mainly target two distinct sets interneurons. In the absence of either modulator, animals are still able to perform roaming and dwelling behaviors, but the duration of the respective promoted state is reduced. Thus, the neuromodulators are not part of the neural mechanisms defining the individual motor patterns (runs and reversals), but constitute upstream regulators that adjust execution of the motor patterns. The two antagonizing pathways modulating roaming and dwelling states are orthogonal to the synaptic connections and not in the classical order sensory > interneuron > motor neuron.

FLP-1 neuropeptides are involved in the regulation of locomotion on food. They have been identified as critical for attenuation of body wave amplitude and locomotion speed on food. *flp-1* is reported to be expressed in several nerve ring interneurons, AVA, AVE, AIA, AVK, AIY, RIG (Nelson, 1998), partially already known for their roles in the regulation of directional locomotion. However, which of these neurons secrete

FLP-1 to regulate locomotion is not known. Aldicarb resistance (a pharmacological assay to measure signaling at NMJs) of animals carrying a *flp-1* mutation indicates that FLP-1 neuropeptides promote activation and contraction of body wall muscles (Sieburth et al., 2005), which could be via increasing excitatory acetylcholine signaling at NMJ. Alternatively, this could be equivalent to a decrease of inhibitory GABAergic signaling at NMJs. In fact, FLP-1 peptides have been implicated in the suppression of the locomotor circuit by modulating GABAergic signaling at the neuromuscular junctions (Stawicki et al., 2013).

Another interesting regulation of locomotion behavior is the transition between crawling and swimming. As mentioned in section 2.3.3, it is debated whether the two patterns constitute two discrete gaits with different underlying neural circuits, or whether the worm uses one shared locomotion circuit that adapts motor output in response to the external forces. The two biogenic amines serotonin and dopamine have been implicated in the regulation of the transition between the two behaviors. While dopamine is essential and sufficient to induce changes from swimming to crawling when animals exit water, the same is true for serotonin and the transition to swimming (Vidal-Gadea et al., 2011). It is not clear however, whether the dopamine and serotonin pathways constitute two separate locomotion circuits or whether the signaling molecules mediate the perception of the mechanical load of the environment and serve to modulate the same locomotion circuit.

How the worm adapts its undulatory motions in order to steer, i.e. change direction during forward movement is not well understood. Course corrections important for klinotaxis or area-restricted search are believed to be executed by biasing motor outputs during sinusoidal forward movement into dorsal or ventral direction. One theory is that steering is mainly executed via head muscles, innervated by head motor neurons. Head motions initiate and direct the furrow within which the worm moves through the environment. The body might simply follow along this pre-defined furrow. Body muscles and VNC motor neurons would serve only to generate the force necessary to push the worm along the substrate. The idea about two separable motor modules is supported by the fact that most interneurons that signal to motor neurons have their major connections within the nerve ring, i.e. they eventually control predominantly movements of the head. As mentioned previously, when VNC motor neurons are ablated, this strongly impairs thrust generation required for progression along the substrate (Chalfie et al., 1985). But even in this case or when all pre-motor interneurons, the main input into VNC motor neurons, have been manipulated, animals

can slowly move forward solely via the head motor system (Kawano et al., 2011; Zheng et al., 1999), suggesting an independent head motor pool.

Head motor neurons are important for strong directional changes during omega turns. SMD motor neurons innervate much of the muscles in the anterior part of the head, and display neural calcium level fluctuation in correlation with head movements (Hendricks et al., 2012) and strong activities in the ventral SMD neurons occur during ventral head bends after reversals (Kato et al., 2015). When all SMD neurons are ablated, the amplitude of turns after reversals is strongly reduced.

While most nerve ring motor neurons have dorsal and ventral members, the paired motor neurons RIV innervate only ventral neck muscles and have been shown to convey a ventral bias to turns following reversals. Despite perturbation of turns after resumption of forward movement, SMD and RIV head motor neurons seem not important for normal (forward and backward) locomotion, i.e. thrust generation. Ablating only ventral neurons of head motor neurons with dorsal and ventral members (SMD, RMD, or SMB) has been shown to cause gentle bias to one side during forward locomotion (Gray et al., 2005). All these findings support the idea about separate motor modules of head and body, with head motions controlling directional changes (steering and turning) during forward movement.

Contrarily, biases of head bending used for steering might also be actively transmitted into biased bending of the whole body by signaling to VNC motor neurons. Likewise, steering could be simultaneously initiated in the head and body through parallel signals to nerve ring and VNC motor neurons. The neural wiring provides support for that, because pre-motor interneurons (signaling to VNC motor neurons) are connected via chemical and electrical synapses to inter- and motor neurons of the nerve ring. Consistent with an interaction between head and body motor system, ablation of RMD or SMD head motor neurons increases the frequency of reversals (Gray et al., 2005). Another class of head motor neurons, SMB, innervates head and neck muscles. Their ablation causes increased amplitudes not only of dorsoventral head swings and but also of sinusoidal body bends. Strong body bends during omega turns might not be solely initiated by head motions but involve body bending control. Acute interference with the activity of either ventral or dorsal GABAergic VNC motor neurons is able to evoke strong, biased body bends and omega turns. Ablation of either VD or DD neurons causes a dorsally or ventrally biased course during forward movement, respectively (Donnelly et al., 2013).

In analogy to interneurons promoting either runs or reversals, there could also be interneurons promoting steering. AIZ nerve ring interneurons are good candidates

because their ablation impairs gradual steering during klinotaxis (Iino and Yoshida, 2009). AIY nerve ring interneurons were also recently reported to be important for steering in salt chemotaxis (Satoh et al., 2014). When moving about perpendicular to the direction of a gradient, animals can detect concentration changes of the sensory cue due to sinusoidal movements of the head. A study made use of this assumption and mimicked this effect through artificial activation of these two interneuron classes (Kocabas et al., 2012): Asymmetric optogenetic activation of channelrhodopsin-expressing neuron classes (light-gated cation channel depolarizing cells upon activation) was achieved by light-stimulation selectively during either dorsal or ventral head bends. Asymmetric activation of either AIY or AIZ interneurons caused the worm to correct its course toward the side of stimulation. These same results were achieved by asymmetric stimulation of cholinergic head motor neurons SMB, while stimulation of GABAergic RME consistently caused steering towards the opposite side of stimulation. Interestingly, symmetrically stimulating AIY neurons (light during ventral and dorsal head swings) evoked increased reversals frequency and no gradual turning. Moreover, AIB stimulation (both asymmetric and symmetric) only affected reversal frequency but not steering. This means that steering was specific to a set of inter- /motor neurons.

In summary, worms can effectively steer by activating head inter- and /or motor neurons. However, it is not clear whether the activation causes additional changes of neural activities in the VNC and employs body adjustments for steering. Given the manipulation of D-type VNC motor neurons, the VNC neural circuits and body muscles might well be contributing to steering.

2.3.6 Characteristics of worm undulations

C. elegans navigates through its environment via undulatory locomotion, which is a means of self-propulsion that relies on generation and propagation of waves along the longitudinal body. These body waves can be characterized in terms of the bending frequency of dorsoventral alternations and their waveform, i.e. amplitude and wavelength (Figure 2.1). Further the worm can modulate the regularity of its body pattern by adjusting the coordination of different body parts.
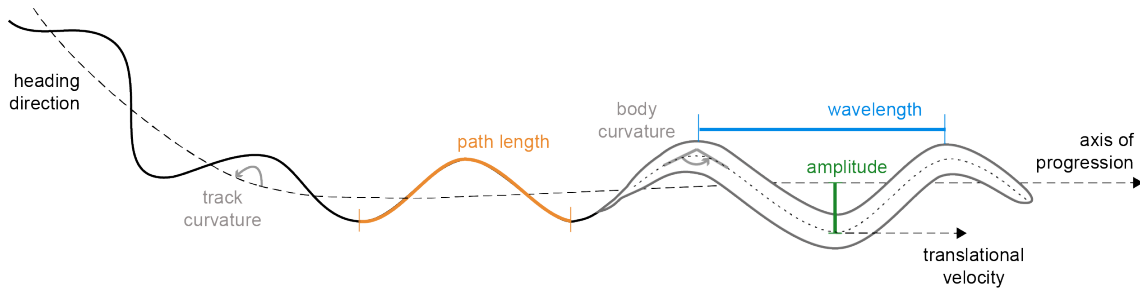
Figure 2.1. Characteristic parameters of undulatory movement.
Wavelength and amplitude describe the worm's waveform. Related to waveform is the body curvature, which can be measured as inter-segment angles. Every point of the worm's body moves along the sinusoidal trajectory, which is characterized by the path length. The effective displacement of the worm is along the axis of progression (instantaneous heading direction). Translational velocity measures speed of effective displacement along this axis. Track curvature measures the change of heading direction.

The wave frequency determines how fast each point along the body alternates between dorsal and ventral sides, or how fast the ventral and dorsal body wall muscles switch between contraction and relaxation. Higher bending frequency should lead to faster progression. Consistently, locomotion speed and bending frequency correlated change in a correlated manner in various mutant worm strains (Cronin et al., 2005; Yemini et al., 2013).

Waveform (amplitude and wavelength) is modified over a wide range when worms experience a range of different mechanical loads from the environment (Berri et al., 2009; Fang-Yen et al., 2010). Under constant external forces, adjustments of waveform are less well studied. However, it was shown that both parameters show a certain degree of variation during movement. Investigation of several mutations affecting locomotion speed reveal changes of wave amplitude in a similar direction as speed while leaving wavelength rather constant (Cronin et al., 2005). Wavelength during forward and backward locomotion is very similar on average, and decreases only slightly during pauses. Wave amplitude is increased during backward movement and during pauses (Cohen et al., 2012; Cronin et al., 2005). Waveform changes might predominantly concern amplitude and to a lesser extent wavelength under constant environmental forces. Nevertheless, both parameters can affect speed by changing the force applied against the substrate. Increasing body curvature should lead to higher local curvature changes along the body, which causes greater thrust (Gray, 1953; Gray and Lissmann, 1964). With constant wavelength, body curvature increases with increasing wave amplitude. On the contrary, higher wavelength decreases thrust by lowering curvature. Taken together, worms might use down-regulation of wavelength and /or up-regulation of wave amplitude in order to promote locomotion speed, at least within a certain range. While wave amplitude is increased, locomotion speed is reduced during backward movement compared to forward movement (Cohen

et al., 2012). With increasing wave amplitude the path length of the sinusoidal track, which every body point travels along, also increases. This means that the increased thrust will increasingly contribute to push the body from side to side and less to promote translational velocity along the axis of progression.

Wave amplitude and frequency have been shown to linearly correlate over a range of environments of different viscosities, evoking different waveforms and bending frequencies (Berri et al., 2009). As increasing contractile force of body wall muscles might likely promote amplitude and frequency of bending, the two parameters might be co-regulated. In mutants with locomotion phenotypes, amplitude and frequency are often, but not always, altered in a correlated manner (Cronin et al., 2005; Yemini et al., 2013). It is not clear yet, to what degree the two parameters can be regulated independently.

In order to dissect the regulation of worm undulatory locomotion one can quantify changes of frequency, wavelength, wave amplitude and /or body curvature. Worm postures are not always perfectly regular wave patterns, but frequently constitute more complex irregular postures. A precise description of worm postures thus requires quantifications of body curvature from a set of segments along the length of the worm. The more segments one measures, the more precise is the posture description. But it is questionable how great *C. elegans'* fine-control over its body postures is, i.e. how many dimensions the nematode regulates to control its locomotion patterns.

To investigate this question, Stephens *et al.* have analyzed the covariance structure of 100 equally spaced segment angles along the worm body length (Stephens et al., 2008). They have found a high degree of correlation between individual body segments, making it possible to reduce the dimensionality of worm locomotion into just four basic shapes. These shapes, termed eigenworms (they are the eigenvectors of the segment angle covariance matrix), dominate the posture repertoire of *C. elegans*, so that different combinations of four eigenworms almost suffice to reconstruct any posture the worm adopts. In other words, the first four eigenworms capture over 95% of postural variance (the order of eigenworms arises from their individual variance contribution) and one can quantify worm locomotion in terms of the projections along just these four dominant shapes, instead of the curvature of all determined body segments.

The authors have also shown that combinations of only the first two eigenworms form a quadrature pair: Their projection amplitudes roughly oscillate with a 90˚ phase shift.

Thus plotting the projection amplitudes against each other yields a ring-like structure and observed combinations of amplitudes describe different phases of the wave along the worm's body. The speed of rotation along the ring correlates with the actual locomotion speed of the worm, while the direction of rotation corresponds to the direction of locomotion. In summary, the first two eigenworms capture the pattern, the direction and the frequency of the sinusoidal wave, with which the worm crawls into forward and backward direction. Finally, increases of projections along the third eigenworm associate with large-angle omega turns and more gradual turns, which correspond to changes in heading direction and worm postures that deviate from the sinusoidal wave pattern.

Another study has investigated the underlying basic shapes of a variety of mutant worms with defects in body posture and locomotion phenotypes (Brown et al., 2013). Eigenworms derived from these defective worms are similar to the eigenworms derived from wild type animals. Consequently, different postures of mutant worms arise from different combinations of the (nearly) same basic shapes. The results of the two studies together suggest that *C. elegans* coordinates its body parts to regulate its postures and locomotion behavior by controlling the combination of a few fixed shapes. This means that the nematode might control only a few relevant behavioral dimensions. Behavioral regulation is executed rather by altering the individual contributions of the basic shapes (eigenworms) than by altering the actual shapes themselves.

2.4 Aims of this study

Locomotion strategies are widely being studied by analyzing the frequency and duration of motor programs (e.g. run duration, turn frequency and direction) and their temporal sequences (e.g. forward propulsive movement followed by asymmetrical body contractions). The results of many studies lead to a continuously better understanding of when and why animals make strategic decisions, how they are being executed on the motor level and how this leads the animals toward their goal like a food patch. Other studies focus on how particular movements such as locomotion are being generated through coordination of multiple body parts. Concepts of higher-level organization of motor programs suggest that the combination of pre-defined coordinated motion patterns (neural modules, muscle synergies) might underlie motor behavior regulation.

It would be very appealing to bring these two research fields together, and investigate how multiple patterns themselves are employed and coordinated with each other to yield complete motor programs /locomotion strategies. Yet, little is known about how animals control the employment of particular motion types to execute distinct locomotion strategies such as traveling and local search. Travel to relocate between habitats is usually faster and more directed movement compared to local search. Therefore travel behavior probably implements more stereotypic and regular motions that are coherent across the whole body, whereas local exploration of a habitat comprises less regular but more flexible motions that allow more detailed probing of the environment. But studies analyzing these distinct motion types during free locomotion are lacking.

Therefore, I aimed to investigate how animals employ stereotypic and more flexible motions and how they coordinate (combine or switch between) the different motion types to yield distinct locomotion strategies. I used the undulatory locomotion of *C. elegans* as a model. The nematode's locomotion parameters can be tracked easily and precisely, and it is possible to simultaneously stimulate a population of animals to switch locomotion strategy in a controlled manner.

With a computational decomposition approach, I dissected locomotion into regular and flexible motions, quantified their contributions to travel and local search behaviors and concluded how their regulation related to changes in locomotion strategy. By studying mutant animals with altered postures I aimed to identify parts of the neural control system regulating the employment of the two distinct motion types. Neural activity of identified neurons was studied by calcium imaging and related to features of the two different motion types.

Contributions

I generated most transgenic worm strains used in this study, designed and performed experiments (worm population assays and freely moving calcium-imaging experiments), wrote analysis codes (body wave decomposition of worm population data and imaging experiments, all further analyses of extracted and decomposed behavioral data and neural activity data) and analyzed all data.

Eviatar Yemini shared and adapted Matlab-based codes used in (Yemini et al., 2013) for segmentation and skeletonization of infra-red videos of freely moving imaging experiments.

Saul Kato wrote codes for generating worm shape reconstructions from decomposed motion patterns in Figure 3.6.

Saul Kato and Manuel Zimmer initiated the approach to decompose worm locomotion into crawling and steering motions.

Richard Latham generated transgenic DVA ablation and DVA imaging line and performed AVK imaging in microfluidic device (Figure 3.22 B).

Movie analysis from worm population assays extracting worm tracks and determining speed, reversals and omega turns, was performed using MATLAB-based tracking software described previously (Chalasani et al., 2007; Ramot et al., 2008; Zimmer et al., 2009), which had been optimized for our purposes by Michael Sonntag.

Analysis codes for skeletonization and inter-segment angle extraction were written by Manuel Zimmer, Saul Kato, Julia Riedl and myself.

Harris Kaplan wrote analysis codes to extract fluorescence intensities from calcium imaging recordings of freely moving imaging experiments.

3 Results

3.1 Worms change their locomotion strategy from travel to local search after oxygen-sensory stimulation

I performed behavioral studies on wild type *C. elegans* worm populations (lab strain N2) after one hour of food (bacteria) deprivation. The animals were moving freely on food-free NGM assay plates and perceived oxygen concentration changes in a flow control arena. 10 Hz high-resolution recordings enabled tracking the animals and quantifying behavioral features such as locomotion speed, directional changes and worm posture via MATLAB-based analyses. The delivery of a sudden oxygen downshift from atmospheric (21%) to intermediate (10%) levels resulted in a drastic behavioral change, which could be interpreted as a change of locomotion strategy, as explained in the following sections.

3.1.1 Description of representative single worm behavior

At constant atmospheric levels of 21% oxygen, 1h food-deprived worms predominantly moved fast with regular sinusoidal body undulations and travelled across distances. To introduce the observed locomotion characteristics, a typical single worm from a population assay is described: A representative video frame at 21% oxygen illustrates the regular wave-like body posture of the animal (Figure 3.1 A, t1). During a longer period at 21% oxygen the worm pursued a rather straight path with occasional subtle course corrections, which enabled it to travel a certain distance (Figure 3.1 B). After stimulation with an oxygen downshift to 10%, worm postures deviated from the previous regular sine-like shapes. During an initial pause, when the animal stopped moving, the bending amplitude was severely reduced (Figure 3.1 A, t2). The worm subsequently resumed slower locomotion while adopting much more flexible and irregular postures that often resulted in steering and turning maneuvers (Figure 3.1 A, t3-4). These rather subtle or stronger changes in the animal's heading direction (steering or turning, respectively) together with more frequent periods of backward-directed movement (designated as reversals) enabled the worm to stay within a restricted area and to locally explore the environment. This was reflected in the worm's path changing from rather straight to more curved (Figure 3.1 B). The effective displacement at 10% oxygen was much smaller than during the travel at 21%, even though in the displayed example the time spent at 10% was twice the time spent at 21%. Overall, the locomotion strategy changed from directed travel promoting dispersal during constant 21% oxygen to local exploratory search after stimulation by shifting to 10%.
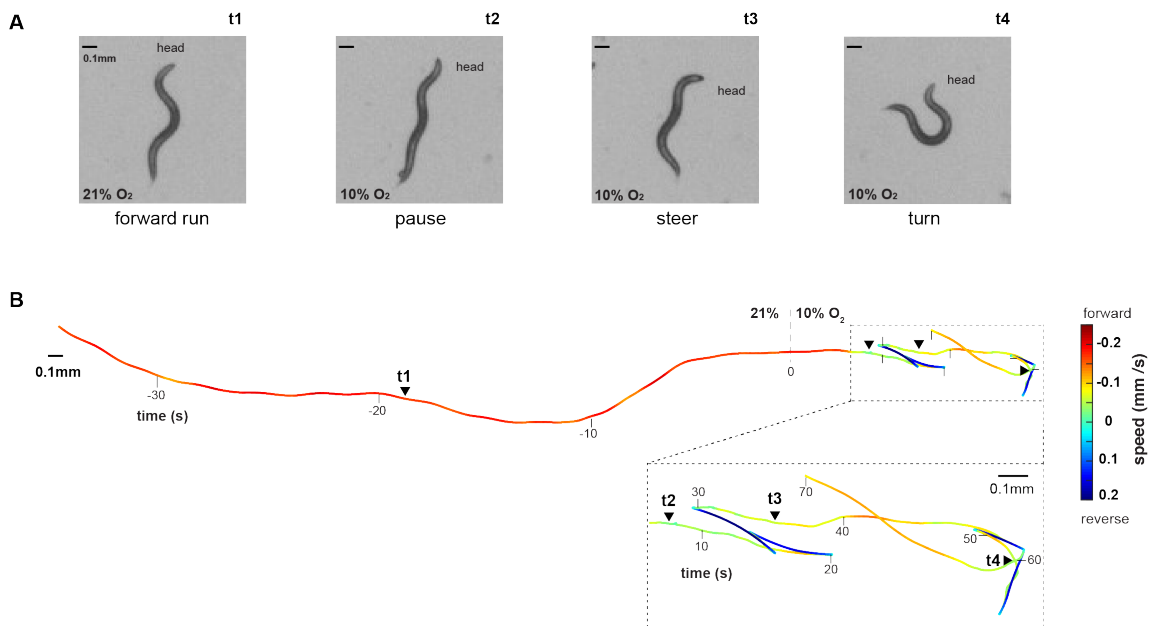
Figure 3.1. An exemplary wild type (N2) *C. elegans* worm changes from fast and directed travel to area-restricted movement after oxygen-sensory stimulation.
(**A**) Representative video frames displaying behavioral changes: (t1) forward run at 21% oxygen, (t2) pause after oxygen downshift to 10%, (t3) steering maneuver and (t4) deep turning maneuver. Time points t1-4 indicated in B. Scale bars are 0.1mm.
(**B**) Path of worm centroid position for 35s at 21% and 70s at 10% oxygen, respectively. Color code displays locomotion speed; reverse movement is shown as negative speed. Time is relative to oxygen downshift from 21% to 10%. Time points of images from A are labeled t1-4. Inset shows most of the path after the downshift. Scale bars are 0.1mm.

To quantify the postural changes and the associated behavioral alterations underlying the distinct strategies, I investigated the worms' body curvatures by measuring 24 inter-segment angles of equally spaced segments along the worms' skeletons from head to tail (Figure 3.2 A). The kymograph shows all segment angles over time, a representation of the worm's body wave (Figure 3.2 B). It illustrates how the fast and regular waves at 21% oxygen become slower and more variable postures after the downshift. The increased irregular character of body waves can be well observed in the time course profile of an individual mid-body angle (Figure 3.2 C). The simultaneous capture of the worm's translational locomotion speed, which measures the instantaneous displacement of its centroid position along the axes of progression, depicts the slow-down of locomotion after the oxygen-sensory stimulation as well as the increased number of reversals (Figure 3.2 D). Locomotion strategy changed from fast and regular travelling with a coherent wave pattern along the body to slow exploratory movement with more complex and irregular postures after oxygen-sensory stimulation.
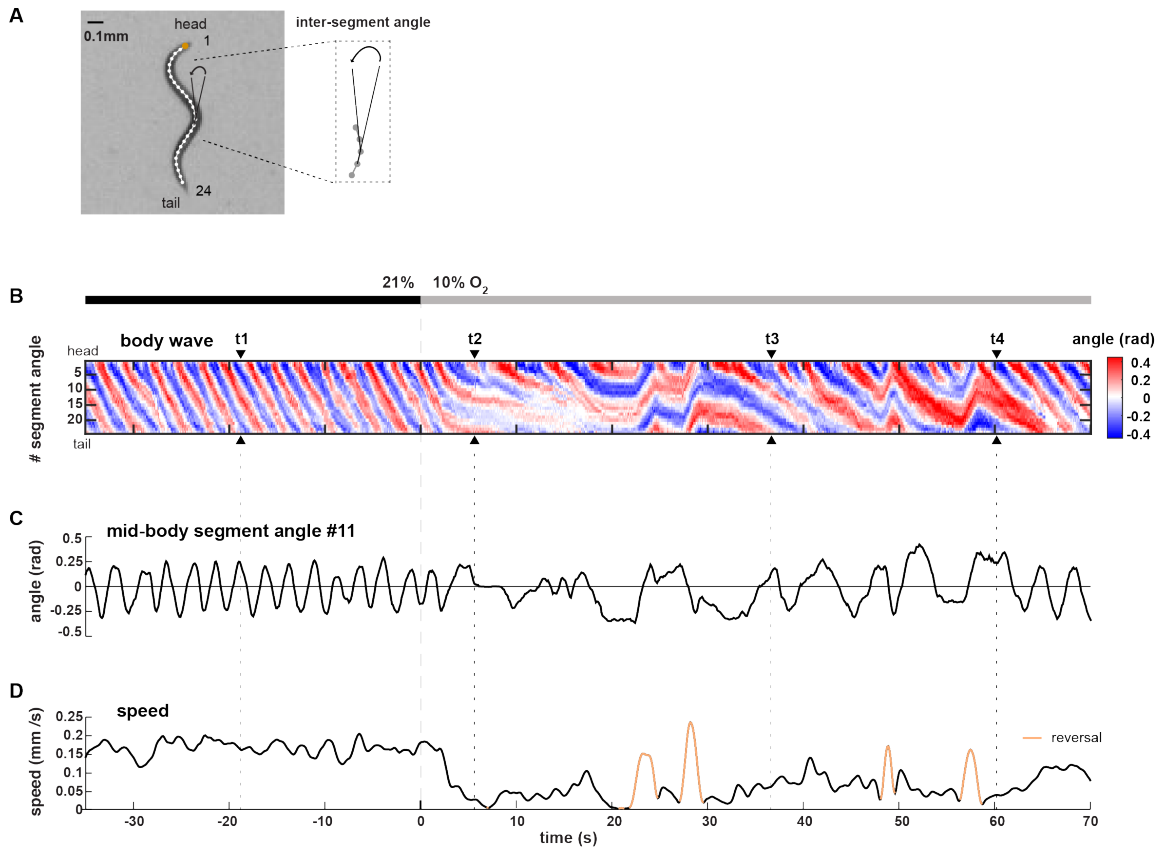
Figure 3.2. Worm body waves become slow and less regular after an oxygen downshift.
(**A**) Worm image overlaid with its traced skeleton composed of 26 points yielding 24 inter-segment angles from head to tail. Exemplary inter-segment angle is shown in inset.
(**B-D**) Quantified locomotion parameters over time of exemplary wild type (N2) *C. elegans* worm perceiving an oxygen downshift. Same animal and time interval as in Figure 3.1. Arrowheads / dashed lines indicate time points t1-4 of worm images from Figure 3.1A. Time is relative to oxygen downshift. Oxygen levels are indicated with a gray bar.
(**B**) Kymograph of 24 segment angles from head (1) to tail (24), displaying the worm's body wave.
(**C**) Time course of mid-body angle #11.
(**D**) Translational speed of the worm's centroid. Reverse movement is indicated by color.

3.1.2 Analyses of worm population behavior

The transition of locomotion strategy from travel to local search became very evident from the trial-averages of the worm population assays. After the oxygen stimulation animals exhibited a strong reduction of translational forward locomotion speed and an increased curvature of their tracks during forward movement (Figure 3.3 A-B), reflecting a rise in number and strength of heading direction changes. Very deep bends strongly changing the heading direction, so-called omega turns, and reversals were identified and displayed elevated frequencies after the oxygen downshift (Figure 3.3 C-D). Overall these behavioral modifications resulted in a drastic decline of the animals' effective displacement (Figure 3.3 E). With increasing time spent at 10% oxygen after the downshift, animals gradually sped up again and decreased reorientation maneuvers.

In summary, worm populations stimulated with an oxygen downshift altered fast and fairly directed dispersal (travel) towards a slow locomotion strategy with increases in subtle and strong directional changes (local search). The two strategies are similar to previously reported behaviors. Travel matches dispersal behavior, which is initiated after 15-30 minutes off food and consists of fast and straight movement with low number of reorienting events (reversals, omega turns). Directly after removal from food animals perform an area-restricted search with frequent reorientation maneuvers (Gray et al., 2005; Hills, 2004; Wakabayashi et al., 2004), similar to the oxygen-induced local search. The strategy change after oxygen decrease was initiated through the sensory neuron pair BAG, which is activated by decreases in ambient oxygen concentration and is required for associated behavioral changes (Zimmer et al., 2009). BAG-ablated animals barely altered any locomotion parameters in response to the oxygen concentration change (Figure 3.3 A-E).
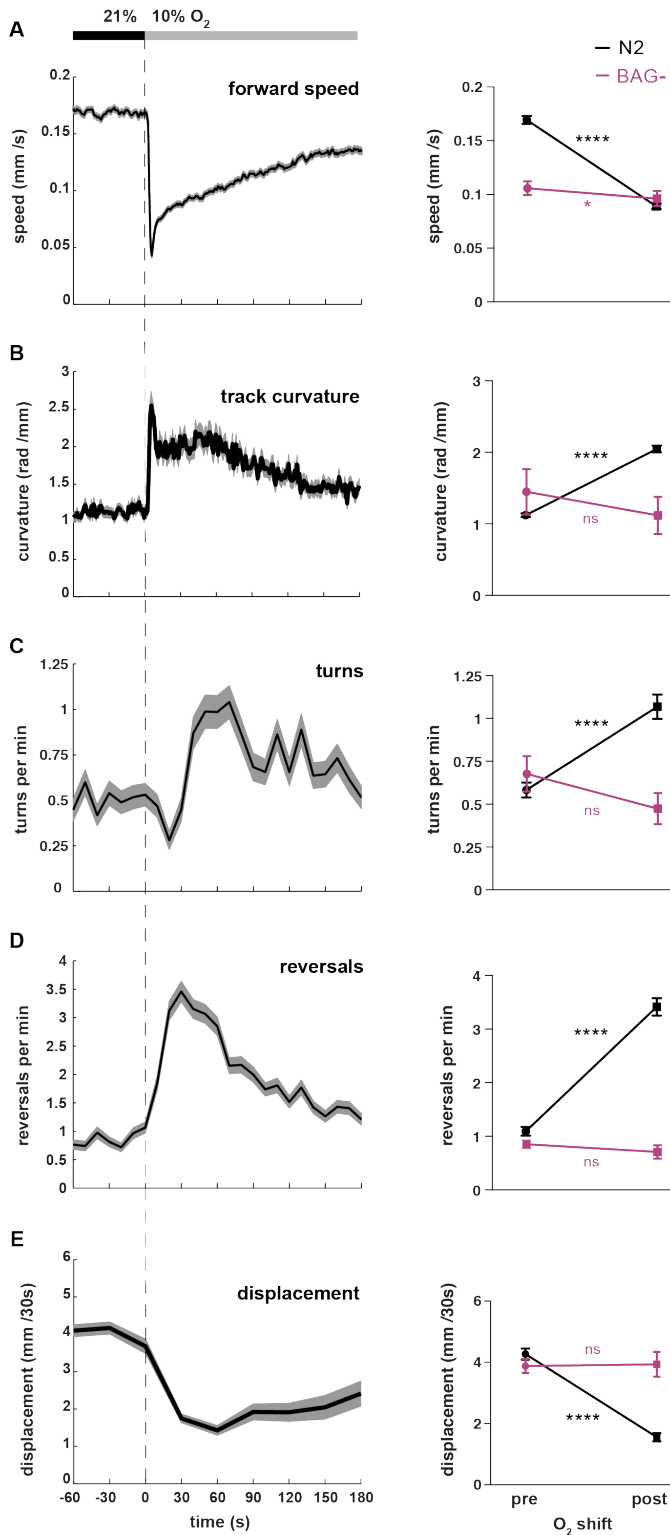
Figure 3.3. Average locomotion parameters from population assays of worms perceiving oxygen downshift from 21% to 10%.
Left: Mean ± SEM in gray of all wild type (N2) worms from 36 populations assays (~25 animals per assay) over time relative to downshift (dashed line). Oxygen levels as shown by bar on top.
Right: Quantifications show means ± SEM of 60s intervals pre- and post-downshift from population assays of wild type N2 (n=36) or BAG- (genetic cell ablation, n=6) worms. Significance values were determined by paired t-tests (**** p ≤ 0.0001, * 0.01 < p ≤ 0.05, ns p > 0.05).
(**A**) Translational forward speed. (**B**) Curvature of worm tracks during forward movement. (**C**) Frequency of deep (omega) turns per animal. (**D**) Frequency of reversals per animal. (**E**) Effective displacement during 30s intervals.

Forward locomotion speed and the animals' track curvature were inversely related, which was revealed by plotting track curvature over speed (Figure 3.4 A). This demonstrates that speed and alteration in heading direction are adjusted in a coordinated, antagonistic manner to control the exertion of locomotion strategies. This observed relation is similar to reported findings under different conditions: On food, animals move more slowly in general and switch between two distinct states, dwelling and roaming, consisting of very slow movement with high track curvature or faster movement with low track curvature, respectively (Ben Arous et al., 2009; Fujiwara et al., 2002).

In the starved off-food paradigm used in this study, the profiles extracted from data before and after oxygen downshift were very similar, implicating that the coordination of speed and directional change was regulated similarly during non-stimulated and stimulated conditions. I plotted the two variables against each other in a 2D density map using a 3-minute interval after the oxygen downshift (Figure 3.4 B), during which a diverse range of locomotion speed was captured (compare to Figure 3.3 A). In contrast to the two separable on-food states roaming and dwelling, which could be discriminated in the corresponding 2D map (Ben Arous et al., 2009), no clear threshold between fast & low-curved movement (travel) and slow & high-curved movement (local search) became evident.
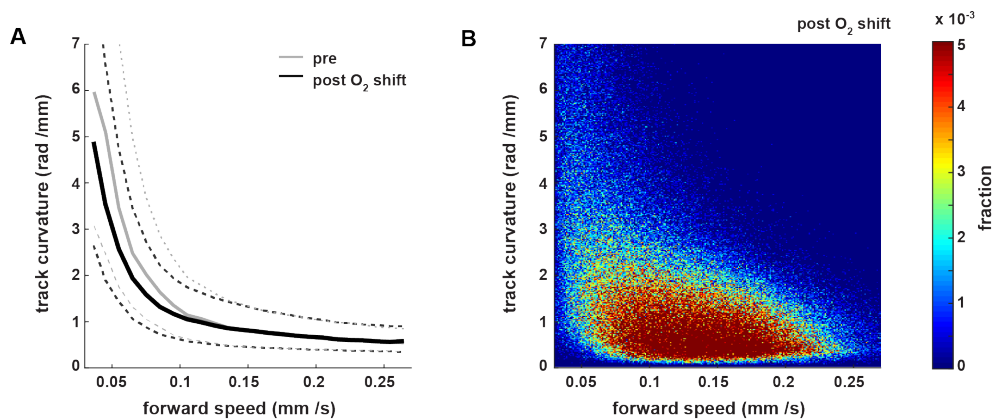
Figure 3.4. Locomotion speed and track curvature are inversely regulated.
(**A**) Median (solid lines) and interquartile range (dashed lines) from all wild type N2 worms of 36 assays (~25 animals per assay) sorting track curvature over median of forward locomotion speed bins (size = 0.01 mm/s). 3min intervals pre- (gray) and post- (black) oxygen downshift were analyzed.
(**B**) Density map showing 2D-histrogram of forward locomotion speed against track curvature, post oxygen downshift. Speed range is cut off due to track curvature artifacts below 0.03mm/s or data sparseness above 0.27mm/s, respectively. Very high track curvature values (>7 rad /mm) are not shown due to data sparseness.

Taken all behavior observations together, wild type worms effectively switched from fast and directed travel to local search in a controlled manner after oxygen-sensory

stimulation, which resembled rather gradual behavioral adaptions than switching between two discrete behavior states.

3.2 Worm locomotion can be described as superposition of crawling and steering motions

To better understand how locomotion strategy was modified after the oxygen-sensory stimulation, I aimed for a method that quantitatively captured the specific behavioral features of worm postures that were up- or down-regulated, respectively: posture flexibility versus regularity, which either restricted animals within a certain area or drove animals forward.

Note that previously reported high-frequency "nose" wiggling (~5 Hz), so-called foraging movements (Hart et al., 1995; Huang et al., 2008; Kaplan and Horvitz, 1993), were not captured under the conditions (temporal and spatial resolution) and thus not included in this study.

3.2.1 Decomposition of the worm's body wave based on eigenworm shapes into crawling and steering waves

I built on a previously reported approach that reduces the dimensionality of worm locomotion (Stephens et al., 2008). Stephens *et al*. showed that undulatory movement of *C. elegans* can be nearly completely described as different combinations of only a few dominant shapes, so-called eigenworms. These shapes describe the correlated motion between segments. Instead of measuring the 95 individual body wall muscles or the curvature of all determined body segments, adding together the projections along four underlying worm shapes almost suffices to reconstruct the worm's full repertoire of postures. Further, the authors showed that combinations of only the first two eigenworms describe a regular wave along the worm's body that corresponds to forward and backward locomotion, while increases along the third eigenworm associate with changes of heading direction.

After extracting time series of 24 segment angles from the N2 wild type population assays, I retrieved 24 eigenworms (EW) by principle components analysis (PCA) as previously reported (Stephens et al., 2008). PCA can identify patterns in data by analyzing the covariance structure of the data. By extracting the principal directions in which the data varies, the description of the data via potentially correlated variables, here the 24 segment angles, is transformed into a description via new uncorrelated variables, in this case the eigenworms. These so-called principal components (PCs) capture, in descending order, the variation present in the data and can be used instead

of the original variables to specify the data by means of projection amplitudes along the PCs.

Before decomposing worm behavior based on the underlying worm shapes, I compared eigenworms derived from the (non-stimulated) travel phase at 21%, or the (sensory stimulated) local search phase at 10% oxygen by using pooled data from 60-second intervals directly before or after the oxygen downshift, respectively. The individual eigenworms looked strikingly similar (Figure 3.5 A) implying that postures during spontaneous travel and oxygen-induced local search relied on a shared space of dominant shapes. Under our analysis and assay conditions (1 hour food-deprivation and off-food recording), the first six eigenworms accounted for 93% of the variability of all worm postures, which was the case for both pre- and post-stimulation phases (Figure 3.5 B). However, variance contributions of individual eigenworms changed: those of EW 1 and 2, which have the highest contribution to the data variation, decreased, while those of EW 3-6 increased after the downshift, when regular travel behaviors were down-regulated and more flexible local search behaviors were up-regulated.
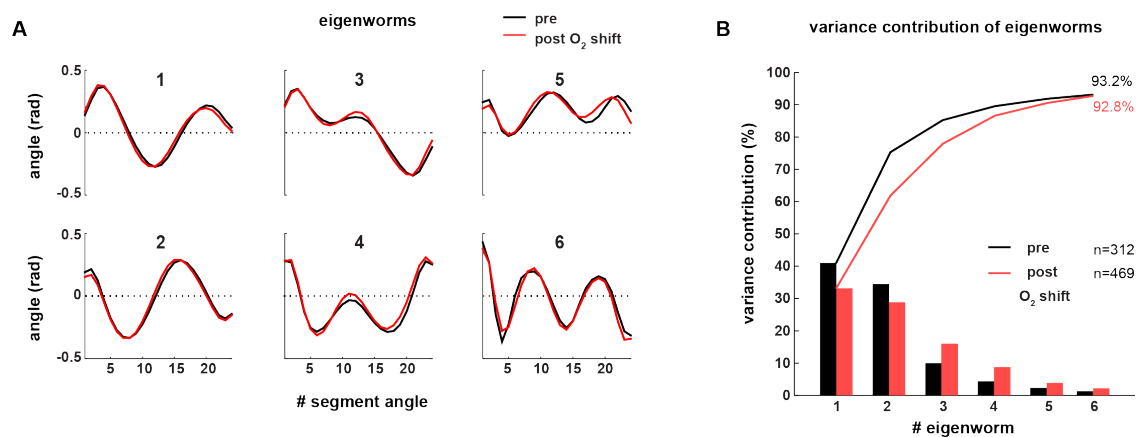
Figure 3.5. First six of 24 eigenworms of wild type N2 worms before and after stimulation with an oxygen downshift
Eigenworms are dominant worm shapes underlying all worm postures. They were calculated by principal components analysis of pooled time series of wild type (N2) worm segment angles, spanning a 60s interval directly pre- (black, n=312) or post- (red, n=469 worms) oxygen downshift.
(**A**) Eigenworms, describing correlated motion along the body. E.g. EW1 indicates that motions of anterior and posterior body are correlated with each other and both are anti-correlated to motions of the mid body.
(**B**) Relative variance contribution to total worm posture. Bars show individual and lines show cumulative variances. Note the similarity of individual eigenworms pre- and post-shift, but a change in their respective variances. The first six eigenworms explain ~ 93% of total variance of worm postures both pre- and post-stimulation.

For further analyses I used eigenworms calculated from all pooled N2 wild type data, which means including pre- and post-stimulation phases, as the derived respective eigenworms were nearly identical. By projecting worm segment angles (the correlated

variables) along the retrieved eigenworms (the new uncorrelated variables) and using the amplitudes of those projections to describe worm postures, it is possible to reduce the dimensionality of worm movement. That is the case when selecting only those eigenworms that significantly contribute to behavioral variance (>90-95% of total data variability), i.e. the first four eigenworms as previously done (Brown et al., 2013; Stephens et al., 2008) or, for these data, the first six eigenworms.

Projecting worm segment angles along all 24 eigenworms and adding all of these projections together fully reconstructs each instantaneous worm posture and their time series (body waves) because no variables are omitted, i.e. 100% of the captured data variability is retained (example kymograph in Figure 3.6 A). But this approach naturally does not reveal anything new. However, building on the finding that the first two eigenworms delineate a regular wave matching the worm's crawling speed (Stephens et al., 2008), I projected the segment angles along only the first two eigenworms, which accounted for over 70% of the behavioral variance, and added the projections together. This approach reconstructed motion patterns similar to the original body waves, with highly regular undulations going along the worms' bodies from head to tail during forward movement and occasionally from tail to head during reverse movement, reflecting how animals crawled to advance across distances. An exemplary worm track was plotted for visualization (Figure 3.6 B). This pattern was accordingly termed 'crawling wave'.

Correspondingly, by projecting the segment angles along the remaining eigenworms 3-24, all residual motions not captured by the regular crawling wave were reconstructed, which yielded surprisingly structured motion patterns (example in Figure 3.6 C). The pattern, which was termed 'steering wave', displayed lower-amplitude and less regular waves during non-stimulated movement and gained strength after the oxygen downshift when the animals adopted more irregular postures, resulting in steering and turning maneuvers (Figure 3.6, t3 and t4). The steering wave could be understood as a second, parallel motion pattern controlling the animal's steering on top of the crawling wave, which promoted displacement.

The concept of two parallel motion patterns superimposed to define the final posture becomes very convincing when graphically reconstructing worm shapes from the individual waves (Figure 3.6 D). Examples illustrate that during fast travel (Figure 3.6, t1) the animal's regular postures are mainly reflected by strong and very regular crawling waves while steering motions are marginal. When the animal pauses and reduces body bending, amplitudes of both crawling and steering waves are kept low

(t2). During steering (t3) and turning maneuvers (t4) in the local search phase, crawling waves similar to those during travel (t1) underlie even those flexible and less regular postures. The strong overlaid steering waves determine the postural outcome and therefore the change of direction.

While the crawling wave shapes during t3 and t4 have very similar magnitudes and the same sign of their segment angles, the parallel steering wave shapes display differences in magnitude and an opposite sign of the segment angles (t3: blue, t4: red in kymograph). Thus very similar crawling waves can be combined with varying steering waves, so that a certain body part of crawling and steering wave shapes, for example the mid-body, can be bent into the opposite (t3) or same direction (t4).
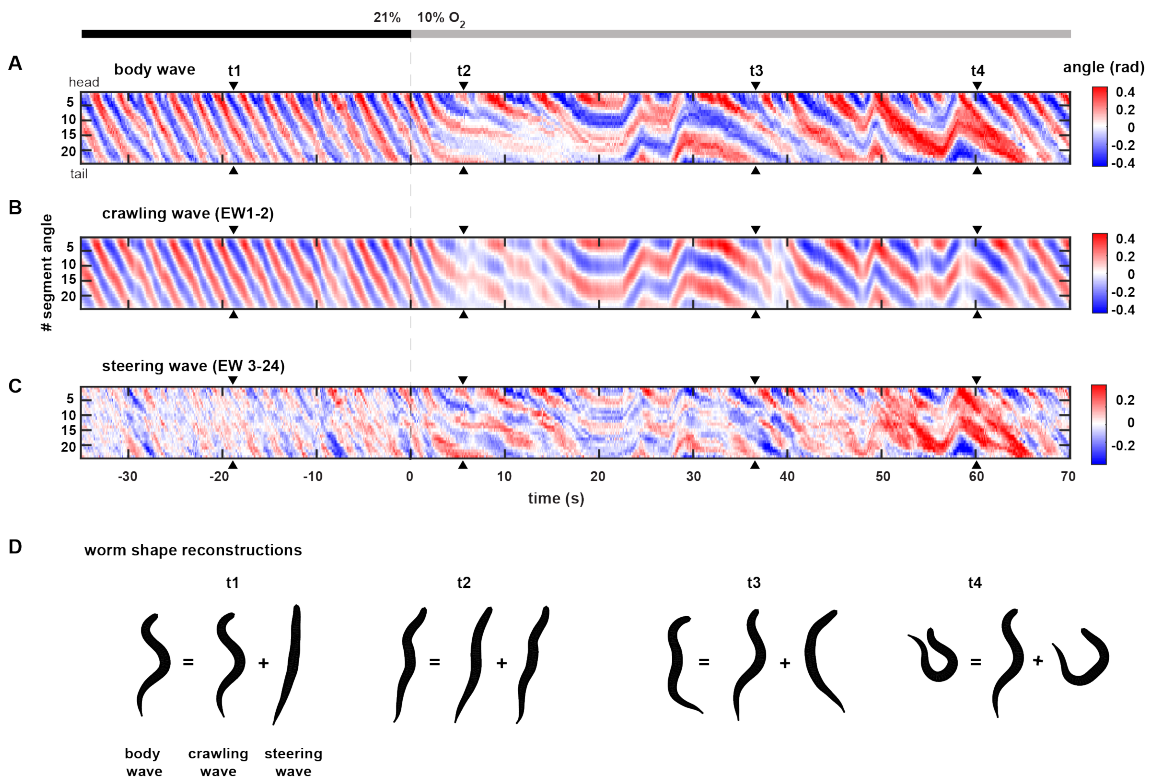
Figure 3.6. Decomposition of the worm's full body wave into a crawling and a steering wave
Eigenworms were calculated by principal components analysis of all pooled time series of wild type (N2) worm segment angles and an individual worm track was projected onto these.
(**A-C**) Kymographs of 24 segment angles over time of an exemplary wild type (N2) *C. elegans* worm perceiving an oxygen downshift. Same animal and time interval as in Figures 3.1 and 3.2 with arrowheads indicating the same time points t1-4. Time is relative to oxygen downshift. Oxygen levels are indicated with a gray bar.
(**A**) Total body wave (same as Figure 3.2 A), identical to projecting the segment angles onto all eigenworms.
(**B**) Crawling wave was derived by projecting the segment angles onto eigenworms 1-2.
(**C**) Steering wave was derived by projecting the segment angles onto the remaining eigenworms 3-24.
(**D**) Graphically reconstructed worm shapes from the individual waves at time points t1-4. (t1) Forward run at 21% oxygen, (t2) pause after oxygen downshift to 10%, (t3) steering maneuver and (t4) deep turning maneuver. From left to right: reconstructions from total body wave, crawling and steering wave.

3.2.2 Characterization of crawling and steering waves

To further characterize the two additive motion patterns, I performed signal cross-correlation analysis (Figure 3.7). Regarding the crawling wave, head inter-segment angle 2 swings in anti-phase with the mid-body segment angle 11 (negative peak value), and in perfect phase with segment angle 19 of the posterior body (positive peak value). In other words, at any time point anterior and posterior parts of the body bend in the same (ventral or dorsal) direction and opposite to mid-body. The cross-correlation structure with maximum peak flanked by smaller valleys and peaks emphasizes the regularity of the crawling wave signal over time. Maximum absolute values very close to 1 highlight the extremely regular wave-like postures of the crawling wave at any time point (Figure 3.7 A-B).

The steering wave segment angles show a positive or negative maximum correlation of the head to mid-body or posterior body, respectively, illustrating how head and mid-body simultaneously bend in the same direction and opposite to the posterior body. This indicates a different waveform compared to the crawling wave (compare to Figure 3.6 D t3 and t4). The values are smaller than 1, due to the less regular character of the steering wave per time point. The wave signal over time also shows less regularity, as regions flanking the peak are close to zero (Figure 3.7 C-D). Interestingly, the lag times of highest correlation of both waves are zero, suggesting that different segments along the worm are controlled simultaneously to generate crawling or steering motions.

Correlating crawling and steering wave against each other (Figure 3.7 E-F) reveals that crawling motions change on average 0.6-0.7 seconds ahead of steering motions, which corresponds to about a quarter of a full undulation cycle (at average speed). The absolute values of peak correlation are relatively low arguing for rather differential regulation of crawling and steering waves; as mentioned before, the two waves can have the same or opposite orientation (Figure 3.6 D t3 versus t4). Nevertheless, steering motions do not occur uncoupled but are phase-locked to crawling motions, similar to the previously reported coupling between the wave described by eigenworms 1-2 and the projection amplitude along eigenworm 3 (Stephens et al., 2008). The fact that head segment angles of the two waves are negatively correlated, while mid-body segment angles are positively correlated, further emphasizes that the two wave patterns are quite distinct from each other.

I further plotted the absolute values of the maximum correlations extracted from cross-correlations performed between the head segment angle 2 and all individual 24 segment angles, and the associated absolute lag times (Figure 3.7 G-H). The crawling wave displays two points along the body (besides the autocorrelation against segment 2 itself) that show perfect correlation (absolute value very close to 1) with the head: namely mid-body (#11) and posterior body (#19). In between these points the correlation is still strong but slightly lower (minimum 0.8). The absolute lag times are minimal (0 s) concomitant with the highest correlation and highest (0.6 s) at segments with lowest correlation. Regarding the steering wave, the same two points along the body correlate best with head motions, although motions of the posterior body correlate better than motions of the mid-body. In between these points the correlation drops to a minimum absolute of 0.2. Similar to the crawling wave profile, the absolute lag times of the steering wave are lowest (0 s) at points of highest correlation and vice versa. Highest lag time is 1 second, i.e. different from crawling wave lag times.
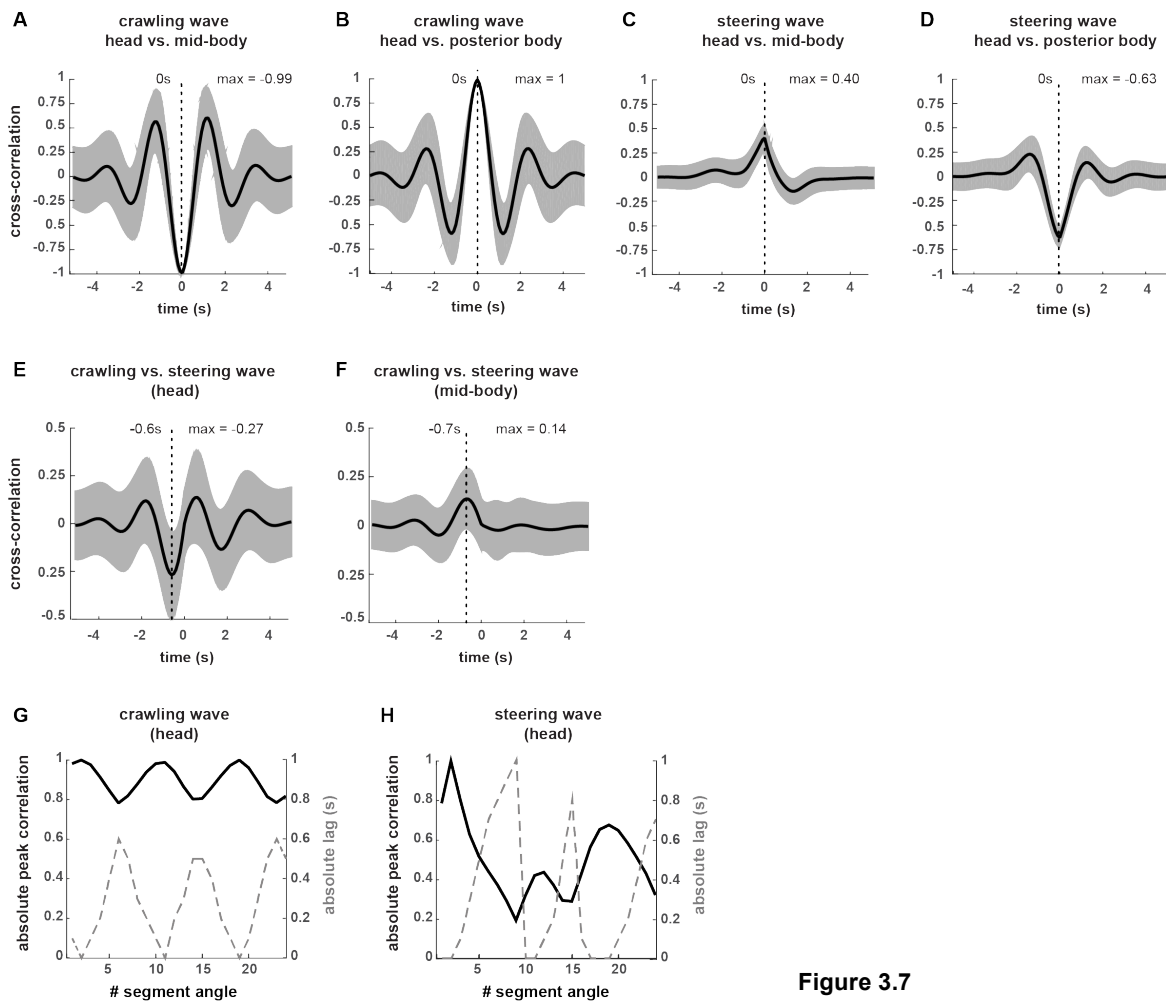
Figure 3.7

Figure 3.7. Cross-correlation analyses of crawling and steering wave
Crawling and steering waves from all wild type N2 time series (>= 20s duration, n=9358) were analyzed by cross-correlation.
(**A-D**) Intra-wave cross-correlation for (**A, B**) crawling or (**C, D**) steering wave between segment angles of head #2 and mid-body #11 (**A, C**) or head #2 and posterior body #19 (**B, D**).
(**E-F**) Inter-wave cross-correlation between crawling and steering wave for (**E**) head #2 and (**F**) mid-body # 11 segment angle. Maximum (absolute) correlation and corresponding lag times indicated.
Displayed is mean ± standard deviation in A-F.
(**G-H**) Cross-correlation of head segment angle #2 against all 24 segment angles during periods of forward movement of all pooled wild type time series during a 3min interval at 21% oxygen. Absolute peak correlation (black solid line) and respective absolute lag between the segment angles (gray dashed line) of (**G**) crawling wave and (**H**) steering wave.

In conclusion, crawling and steering wave both display inter-segmental coordination along the body, but the two motion patterns are quite distinct from each other. The crawling wave is highly regular with a different waveform than the much less regular steering wave. A subset of points along the worm body appear to be controlled simultaneously to generate crawling or steering motions, while others might be adjusted with a time delay.

Next, I analyzed the relation between the individual waves and the locomotion parameters track curvature and locomotion speed, which had been employed initially to characterize travel and local search behavior (section 3.1). Therefore, I calculated the wave power by summing the absolutes of all 24 segment angles per time point. An inter-segment angle of zero should ideally result from zero bending strength of the adjacent segments. The more the angle deviates from zero, the higher the bending strength. In order to capture the whole-worm absolute bending strength exerted by the respective wave, the sum of all segment angle absolutes thus represents a good measure. Moreover, I focused on the predominant forward locomotion and excluded reverse locomotion from my further analyses because forward and reverse locomotion exhibit differences in terms of mechanism and neural control: The worm's body wave inverses its direction and many neurons show distinct activities during forward and reverse locomotion (see section 2.3.5 and Kato et al., 2015). Importantly, steering and turning maneuvers as part of forward movement were not excluded.

I plotted the individual wave powers over track curvature, which indicates changes in heading direction, during forward locomotion for 3-minute intervals before or after the oxygen downshift, respectively (Figure 3.8). The total body wave power was continuously rising along increasing track curvature during the non-stimulated phase at 21% oxygen (Figure 3.8 A gray line). This relation weakened after oxygen-sensory

stimulation (black line) when track curvature was on average higher (Figure 3.3 B). Events leading to strong directional changes (>2 rad /mm) in the local search phase depended on less strong body wave bends than during the travel phase. The crawling wave power displayed less meaningful relations to track curvature (Figure 3.8 B). Yet, after the oxygen downshift, crawling tended to decrease along increasing changes of direction. The steering wave, which had shown relatively stronger values during steering and turning maneuvers (Figure 3.6 t3 and t4), indeed exhibited a positive relation to track curvature, both before and after oxygen-sensory stimulation (Figure 3.8 C). Plotting the steering wave power on top of worm trajectories (Figure 3.8 D) further illustrates how events of solid directional change coincide with a powerful steering wave signal, which is consistent with the previously reported association between turning and projection of worm postures along the third eigenworm (Stephens et al., 2008).
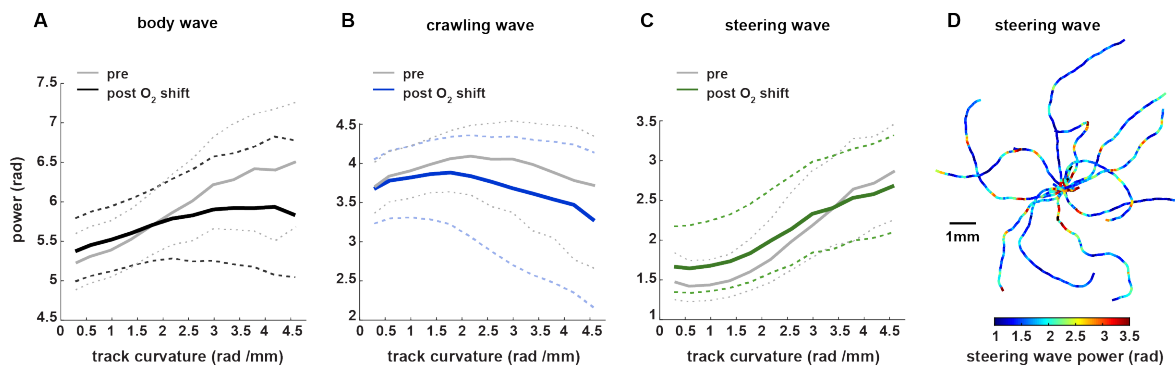
Figure 3.8. Relations between wave powers and track curvature
(**A-C**) Median (solid lines) and interquartile range (dashed lines) from all wild type N2 worms of 36 assays (~25 animals per assay) sorting the different wave powers over median of track curvature bins (size = 0.4 rad /mm). 3min intervals pre- (gray) and post- (black or color) oxygen downshift were analyzed. Power is the sum of absolutes of all segment angles and represents a measure of the worm's overall bending magnitude.
(**A**) Total body wave, (**B**) crawling wave and (**C**) steering wave. Very high track curvature values (>4.7 rad /mm) are cut off due to data sparseness.
(**D**) Exemplary worm trajectories during the 10% oxygen interval aligned at their starting points with color code indicating power of the steering wave.

In conclusion, adjustments of worm heading direction (steering) correspond to up-regulation of the steering wave, justifying its name. This positive relationship is reflected in the total body wave's association to track curvature, especially for non-stimulated animals. After stimulation, crawling motions are slightly down-regulated during stronger changes in heading direction. Therefore the increase of total body wave power is milder along increasing directional change.

Next, I plotted the individual wave powers over locomotion speed during forward movement, separately for 3-minute intervals before or after the oxygen downshift (Figure 3.9 A-C). Total body wave power appeared to be only marginally regulated over the locomotion speed range, with a downward trend along increasing speed. Crawling wave power showed a steady increase along a speed range from 0 to ~0.15 mm /s, after which it remained constant, indicating a role in promoting crawling speed until this threshold. Steering wave power displayed a reciprocal relation with locomotion speed, concordant with the inverse relation between speed and track curvature (Figure 3.4). The associations are tighter, i.e. display lower variance, at higher locomotion speeds. Thus, fast travel is achieved by execution of strong crawling motions and repression of steering motions.

The two parallel waves display a meaningful inverse relation themselves (Figure 3.9 D): When animals are executing powerful crawling during travel, they down-regulate steering motions. While performing strong steering, they decrease their crawling power. The steering wave can be understood as the local search-promoting motion pattern being up-regulated when animals move with slower speed and stronger changes in heading direction. The crawling wave on the contrary is driving traveling behavior, with its frequency being a significant determinant of locomotion speed (Figure 3.9 E). The strength of crawling motions consistently displayed a similar relation to crawling wave frequency as to locomotion speed (Figure 3.9 F).

It is interesting to note that the observed relations were very similar pre- and post-stimulation (during non-stimulated travel and stimulus-induced local search), implying that the motion patterns and locomotion speed were continuously co-regulated in the same manner.
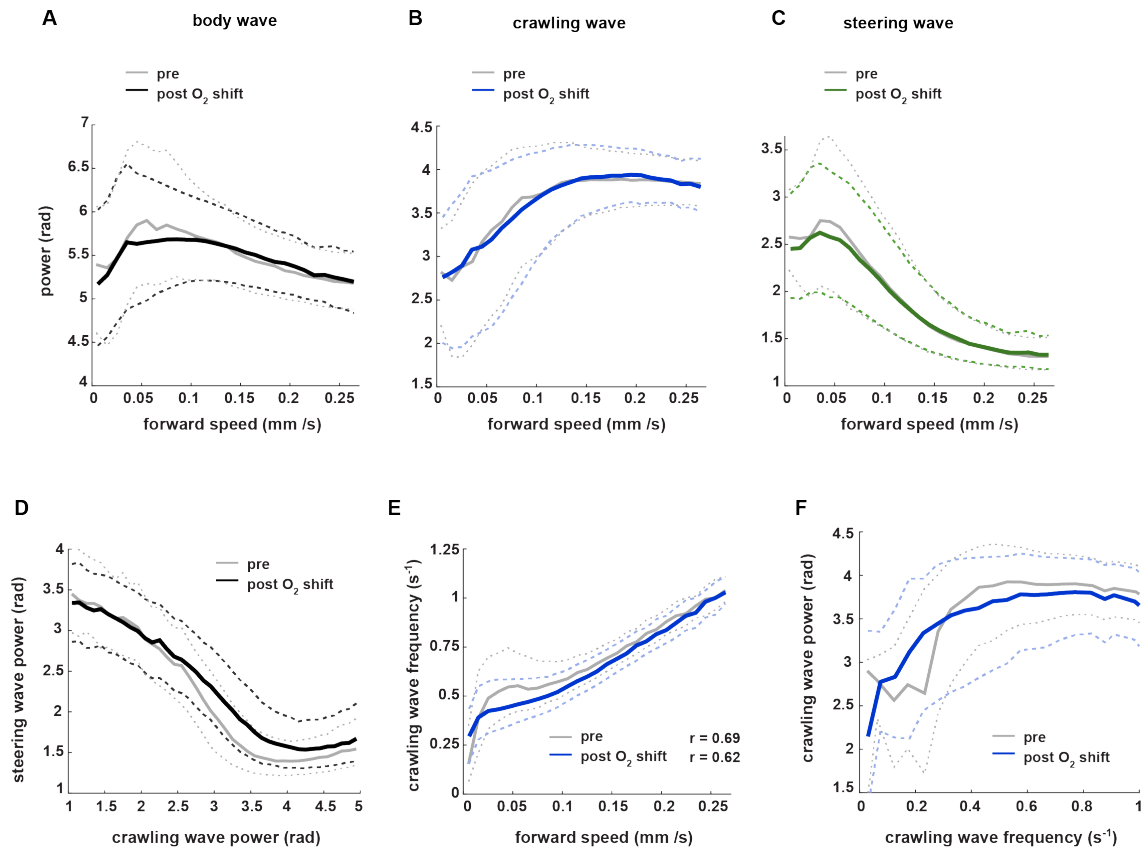
Figure 3.9. Relations between wave features and forward locomotion speed
(**A-C**) Median (solid lines) and interquartile range (dashed lines) from all wild type N2 worms of 36 assays (~25 animals per assay) sorting the different wave powers over median of locomotion speed bins (size = 0.01 mm /s) during forward movement. 3min intervals pre- (gray) and post- (black or color) oxygen downshift were analyzed. (**A**) Total body wave, (**B**) crawling wave and (**C**) steering wave.
(**D-F**) Median and interquartile range from all wild type N2 worms (during forward movement) sorting
(**D**) steering wave power over median of crawling wave power bins (size = 0.1 rad),
(**E**) crawling wave frequency over median of locomotion speed bins (size = 0.01 mm /s),
(**F**) crawling wave power over median crawling wave frequency (size = 0.05 s^{-1}).
Frequency is measured as ventral or dorsal bends (half an undulation cycle) of mid-body segment angle #11 per second. Respective linear correlation coefficient r is indicated.
Very high values of x-axis (> 2.7 mm /s or 5 rad or 1s^{-1}) are cut off due to data sparseness.

Overall, decomposition of worm locomotion into crawling and steering waves results in two meaningful parallel motion patterns, which quantitatively capture the distinct flexible or regular motion features either restricting animals within a certain area or driving them forward. These motion patterns appear to be inversely co-regulated, and each coordinated with locomotion speed, which overall defines the animals' locomotion strategy.

3.3 Adjustments of crawling and steering motions facilitate strategy change from travel to local search after oxygen-sensory stimulation

Employing the power of crawling and steering waves as a measure of their respective strength reduced the description of worm behavior to two dimensions. By this means I could further study the differential regulation of crawling and steering motions and the adjustment of locomotion strategies after oxygen-sensory stimulation. Initially, I analyzed the responses of the wild type N2 worm populations.

3.3.1 Crawling and steering waves change antagonistically after sensory stimulation

The inverse relationship between crawling and steering waves (Figure 3.9 D) could also be observed in the time course averages from the oxygen-stimulation population assays. Mean crawling wave power decreased after the oxygen downshift (Figure 3.10 A), when worms reduced traveling behavior. This was reflected in the similarity between the time courses of crawling wave power and forward speed (Figure 3.3 A). Meanwhile, when local search patterns became more prominent, the steering wave power increased (Figure 3.10 A), resembling the track curvature time course (Figure 3.3 B). Similar to the time-course of speed and track curvature, with increasing time spent at 10% oxygen after the downshift, both wave powers gradually returned toward levels observed during traveling.

The total body wave power, which is exactly the same as the sum of the two parallel patterns, presented a bi-sequential course, which can be better understood when interpreted as the superposition of the crawling and steering signals. It initially declined when the crawling wave down-regulation exceeded the steering wave up-regulation, and eventually moderately rose when steering wave changes dominated.

I extracted the relative distribution functions of the individual wave powers, which showed non-symmetrical distributions especially in the case of crawling and steering wave (Figure 3.10 B). The drop of crawling wave power after the sensory stimulation was caused by a gain of the left tail of its distribution, which constitutes a relative increase of low-power bends. The opposite, a relative gain of high-power bends, was uncovered for the steering wave power, whereas the total body wave (again as a result of the addition of the two individual patterns) exhibited moderate relative increases in high- and low-power bends.

In conclusion, steering or crawling waves quantitatively captured the respective flexible or regular motions that were up- or down-regulated in response to oxygen-sensory stimulation.
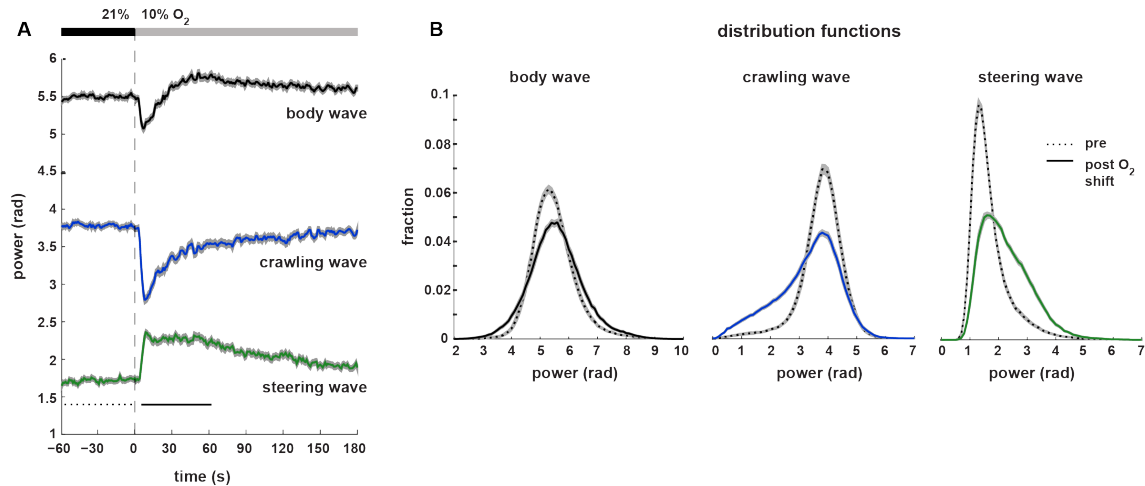
Figure 3.10. Antagonistic responses of crawling and steering wave to oxygen downshift
Behavioral responses of worm body wave (black), crawling wave (blue) and steering wave (green) to an oxygen downshift from 21% to 10%. Forward locomotion was analyzed in 36 population assays of wild type (N2) worms (~25 animals per assay).
(**A**) Mean ± SEM in gray of all worms from populations assays over time relative to oxygen downshift (dashed line). Oxygen levels are indicated by gray bar.
(**B**) Mean (± SEM in gray) of relative distribution functions derived per assay (n=36) of 60s intervals pre- (dashed) and post- (solid line) downshift. Intervals are indicated with horizontal lines in A.

3.3.2 Crawling and steering waves are gradually regulated by sensory input

I performed similar population assays stimulating worms with an oxygen ramp decreasing from 21 to 4%. The average time courses showed more gradual behavioral changes elicited by the gradual stimulus (Figure 3.11 A). Positive changes of steering wave dominated the negative changes of crawling wave over the whole ramp, as the total body wave demonstrated no fall but only a subtle rise over its baseline. The distribution functions of crawling and steering wave power from short intervals during the first half of the ramp, when animals continuously adjusted locomotion, indicated that the oxygen-evoked motion pattern changes were indeed gradual (every interval differed from the others) instead of abrupt adjustments (Figure 3.11 B-C).
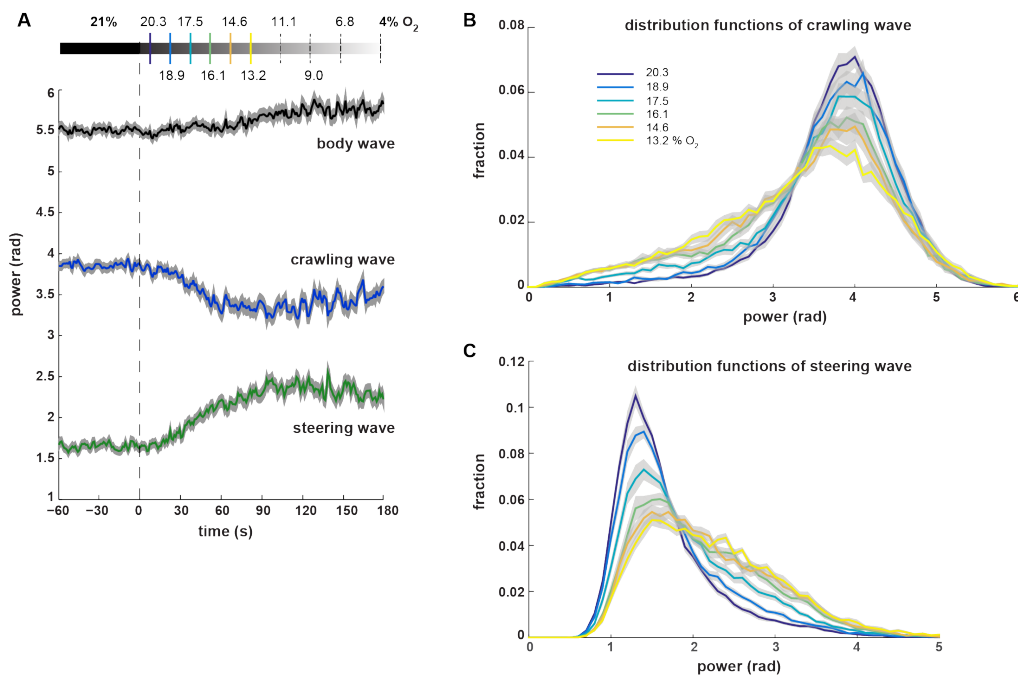
Figure 3.11. Gradual changes of crawling and steering wave in response to an oxygen ramp
Behavioral responses during forward movement to a decreasing oxygen ramp from 21 to 4% were analyzed in 15 population assays of wild type (N2) worms (~25 animals per assay).
(**A**) Mean ± SEM in gray of worm body wave (black), crawling wave (blue) and steering wave (green) of all worms from populations assays over time relative to oxygen ramp onset (dashed line). Oxygen levels are indicated by gray bar.
(**B-C**) Mean (± SEM in gray) of relative distribution functions derived per assay (n=15) of (**B**) crawling and (**C**) steering wave power over 15-second consecutive intervals during first half of the decreasing ramp. Colors indicate oxygen concentration of interval centers and are indicted in the oxygen bar in A.

3.3.3 Travel and local search behaviors appear as extremes of one continuous locomotion mode.

In analogy to the 2D density map of speed versus track curvature, which did not reveal discrete behavioral states (Figure 3.4 B), density maps plotting speed versus steering wave power also appeared to display one continuous locomotion mode (Figure 3.12). As the relations were not affected by the sensory stimulation (Figure 3.9 C), I combined a 1-minute period before and a 3-minute period after the stimulus to ensure sampling over wide ranges of the respective behaviors. I investigated the distribution for the oxygen downshift and oxygen ramp assays. In both paradigms, there were gradual drifts from fast & low steering to slow & strong steering. These data suggest that animals were not switching states between a fast crawling and a slow steering mode, and instead support the concept that travel and local search behaviors are extremes of one continuous locomotion mode in food-deprived worms. Again, this is in contrast to the two discrete alternative behavioral states, roaming and dwelling, observed in animals moving on a bacterial food lawn (Ben Arous et al., 2009; Fujiwara et al., 2002).
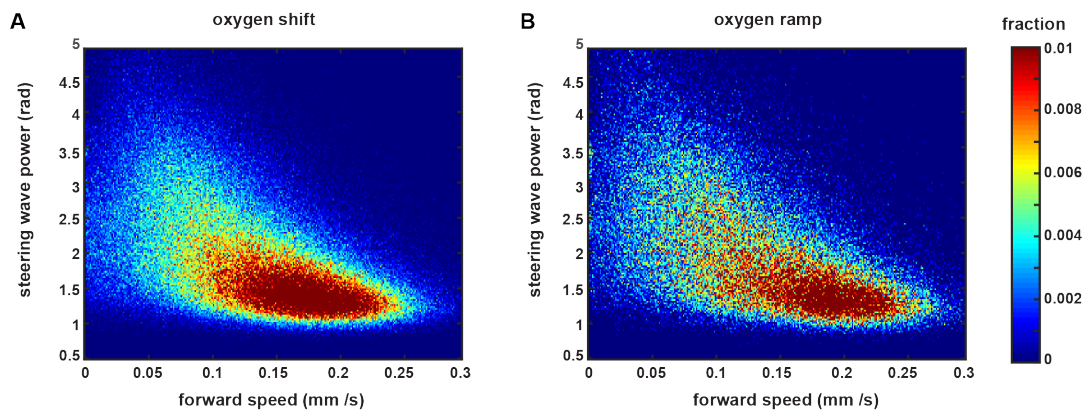
Figure 3.12. Inverse adjustments of locomotion speed and steering wave appear gradual.
Density maps showing 2D-histrogram of forward locomotion speed against steering wave power from all wild type N2 worms of 36 assays (~25 animals per assay), including periods before (1min) and after (3min) the oxygen downshift to ensure sampling over a wide range of each parameter. Very high values of speed (> 0.3mm/s) or steering wave (>5 rad) are not shown due to data sparseness.
(**A**) Oxygen downshift from 21% to 10% and (**B**) oxygen ramp from 21% to 4%.

3.4 Locomotion strategies are controlled through antagonistic peptidergic interneurons

To uncover parts of the underlying neural systems controlling crawling and steering motions that determine locomotion strategies, I investigated manipulated worm strains that were partially already known for their posture defects.

3.4.1 Peptidergic signaling from two interneurons regulates worm posture and locomotion speed

FLP-1 neuropeptides have been identified as critical for attenuation of body curvature on food (Nelson, 1998), while the single tail interneuron DVA, involved in mechanosensory integration and reported to function as a proprioceptive stretch-sensor, was revealed to promote body curvature (Li et al., 2006; Wicks and Rankin, 1995). NLP-12 neuropeptides were shown to be exclusively released from DVA, with secretion enhanced by muscle contraction, leading to increased synaptic transmission at cholinergic neuromuscular junctions and positive effects on locomotion speed (Hu et al., 2011; Janssen et al., 2008). During the course of my study, NLP-12's role in producing higher body curvature directly after removal from food was demonstrated (Bhattacharya et al., 2014).

I confirmed the roles of these curvature regulators also in the food-deprived, off-food paradigm with the addition of another interneuron class, the left-right pair AVK situated in the ventral head ganglion. AVK is an identified source of FLP-1 neuropeptides amongst other interneuron classes (Nelson, 1998), relatively rich in gap junctions (Varshney et al., 2011; White et al., 1986) and so far only known to have a function in gustatory associate learning via neuropeptides encoded from the *ntc-1* gene (Beets et al., 2012). Mutations in *flp-1* or genetic ablation of AVK interneurons caused exaggerated body curvatures and thus largely increased body wave power during forward locomotion at 21% oxygen. On the contrary, mutations in *nlp-12* or genetic ablation of DVA yielded low-magnitude bending worms with significantly reduced body wave power (Figure 3.13 A-B). Combined manipulations, i.e. *flp-1; nlp-12* mutant worms or ablations of AVK and DVA, resulted in intermediate phenotypes different from single manipulations and more similar to wild type, suggesting a parallel antagonistic control system to adjust body curvature.

The *flp-1* high-curvature phenotype could be restored to wild type levels by expression of functional *flp-1* under the endogenous *flp-1* promoter, but also by specific expression in the AVK interneuron pair only, or by separate expression from other *flp-1* expressing interneurons (AVA, AVE, RIG, AIY). However, a fluorescent reporter

construct under the control of the *flp-1* locus indicated strongest endogenous FLP-1 expression from AVK (not shown), strengthening its role in FLP-1 signaling to repress body curvature. *nlp-12* expression under its endogenous promoter, active solely in DVA as intensively evidenced recently (Bhattacharya et al., 2014; Hu et al., 2011; Janssen et al., 2008), rescued the *nlp-12* mutant phenotype (Figure 3.13 C). Importantly, AVK and DVA neurons send out processes along the whole ventral nerve cord of the worm (illustrated in Figure 3.13 D).
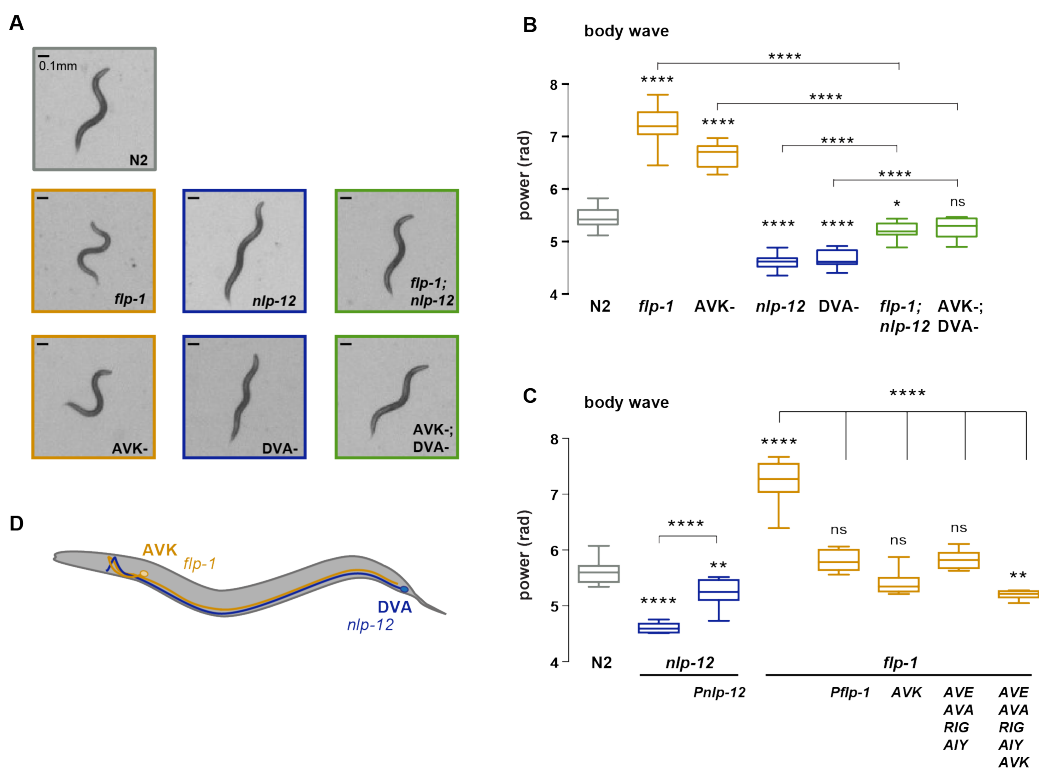
Figure 3.13. AVK and DVA interneurons regulate worm posture with the help of FLP-1 and NLP-12 neuropeptides.
(**A**) Representative video frames during forward motion at 21% oxygen of wild type (N2) and manipulated worms (neuropeptide mutant or genetic cell ablation) illustrating effects on body curvature. Heads are pointing upwards. Scale bars are 0.1mm.
(**B-C**) Boxplots of total body wave power (during forward locomotion) measured during a 4min interval at 21% oxygen. (**B**) Body curvature mutants and (**C**) rescue lines.
Boxplots display median, interquartile range and 5-95 percentile whiskers. All strains were compared to wild type N2, and rescue strains against respective mutant or selected genotypes as indicated, using one-way-ANOVA with Sidak's correction and calculated with n = number of experiments (~25 animals per assay): (B) N2 n=36, *flp-1* n= 29, AVK- n=21, *nlp-12* n=21, DVA- n=13, *flp-1; nlp-12* n=12 and AVK-; DVA- n=10. (C) N2 n=10, *nlp-12* n=6, *nlp-12* rescue under *Pnlp-12* n=11, *flp-1* n=11, *flp-1* rescues *Pflp-1* n=10, *AVK* n=9, *AVE,AVA,RIG,AIY* n=9 and combination *AVK* plus *AVE,AVA,RIG,AIY n=9.* Reported expression of endogenous promoters: DVA only for *Pnlp-12* and AVK, AVA, AVE, AIY, RIG, RMG, AIA and M5 for *Pflp-1*. (**** $p \leq 0.0001$, *** $0.0001 < p \leq 0.001$, ** $0.001 < p \leq 0.01$, * $0.01 < p \leq 0.05$, ns $p > 0.05$).
(**D**) Worm scheme illustrates structure of interneurons AVK and DVA, and the expressed respective neuropeptide gene *flp-1* or *nlp-12*.

In addition to effects on worm postures, the identified regulators also affected forward locomotion speed (Figure 3.14 A-C). Activity of AVK, independent of FLP-1 signaling, and NLP-12 signaling proved important in maintaining a high locomotion pace during non-stimulated travel at 21% oxygen. Full capacity to down-regulate locomotion speed to properly transit from fast to slow motion after the oxygen stimulation was dependent on the presence of AVK and FLP-1. Interestingly, additional manipulations of *flp-1* or DVA partially relieved the lower-speed phenotype of single manipulated *nlp-12* or AVK-ablated animals, respectively, arguing for a speed-repressive role of functional FLP-1 or DVA, which is only revealed in slow animals. Overall, this characterized regulatory system (with the exception of DVA) was essential for efficient displacement during non-stimulated travelling and a proper reduction of displacement after the oxygen stimulation (Figure 3.14 D-E). Displacement is the combined result of diverse locomotion features. Naturally it is supported by high speed and restricted directional changes, i.e. low steering and low numbers of reversals.

The impaired speed change after stimulation of *flp-1* mutants could be restored by expression under its endogenous promoter, by expression in the AVK interneuron pair only, or in other *flp-1* expressing interneurons (AVA, AVE, RIG, AIY). Interestingly, combined reconstituted expression in AVK and AVA, AVE, RIG, AIY by crossing both rescue lines together, might have yielded artificially high FLP-1 levels resulting in a speed-repressive effect during non-stimulated travel. *nlp-12* expression in DVA under its endogenous promoter partially rescued the low-speed phenotype of *nlp-12* mutants at 21% oxygen, however without fully restoring wild type levels (Figure 3.15 A-C). Effective displacement phenotypes of *nlp-12* mutants could not be rescued from expression under its endogenous promoter, while *flp-1* displacement impairments could be restored by FLP-1 expression from AVK or the other interneurons AVA, AVE, RIG, AIY, but not by their combination (Figure 3.15 D-E).
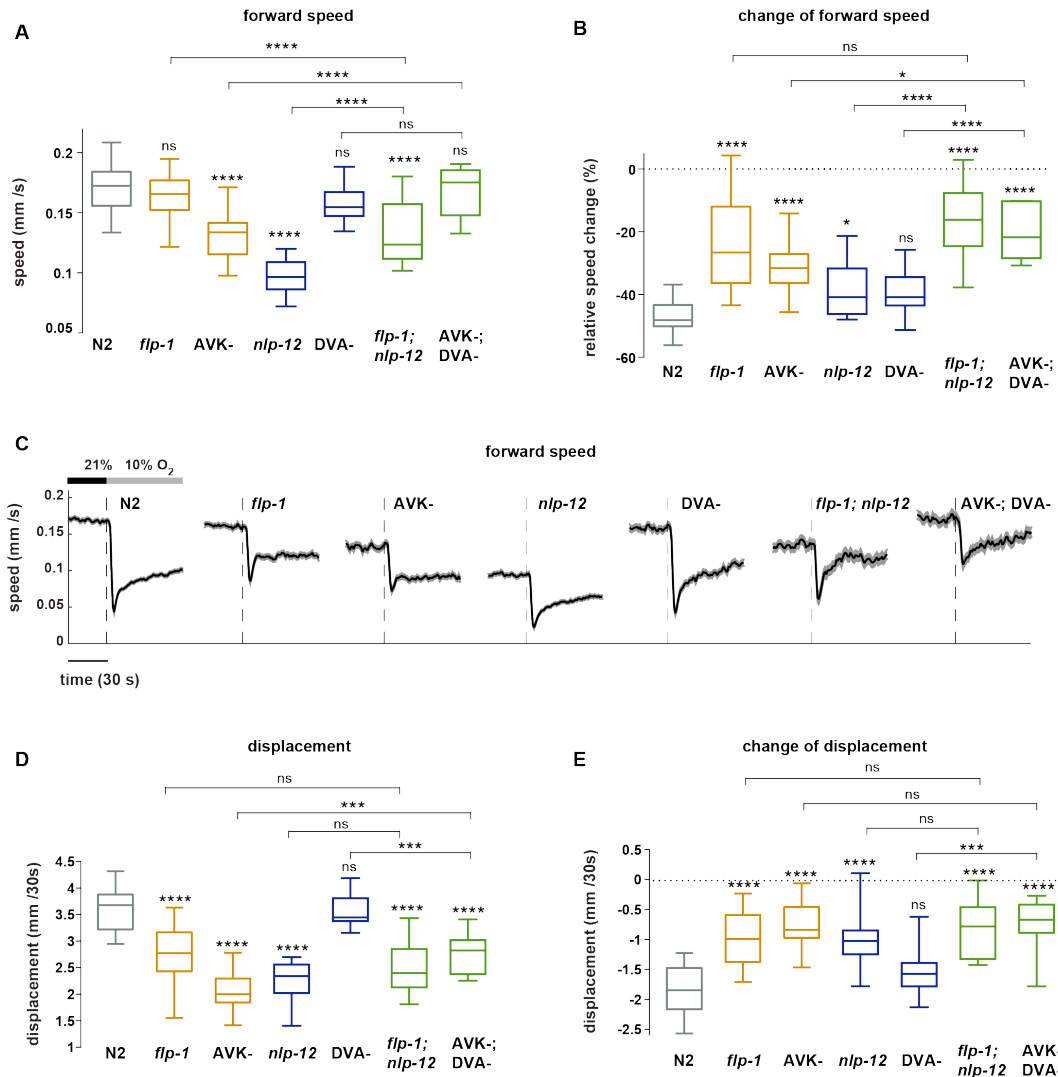
Figure 3.14. Locomotion speed and displacement regulation by AVK and DVA interneurons and neuropeptides FLP-1 and NLP-12

(**A-B**) Boxplots of translational forward locomotion speed (**A**) measured during a 4min interval at 21% oxygen and (**B**) of the behavioral change in response to the oxygen downshift, quantified as the relative difference between 60s intervals pre- and post-downshift, normalized to the interval pre-downshift.

(**C**) Mean ± SEM in gray shows translational forward speed of all worms of population assays (~25 animals per assay) over time. Gray bar indicates oxygen concentration and dashed lines the downshift.

(**D-E**) Boxplots of effective displacement per 30 seconds (**D**) measured during a 3min interval at 21% oxygen and (**E**) of the behavioral change in response to the oxygen downshift, quantified as the difference between 60s intervals pre- and post-downshift. Boxplots display median, interquartile range and 5-95 percentile whiskers. All strains were compared to wild type N2, and selected genotypes as indicated, using one-way-ANOVA with Sidak's correction and calculated with n = number of experiments (~25 animals per assay): N2 n=36, *flp-1* n= 29, AVK- n=21, *nlp-12* n=21, DVA- n=13, *flp-1; nlp-12* n=12 and AVK-; DVA- n=10. (**** $p \leq 0.0001$, *** $0.0001 < p \leq 0.001$, ** $0.001 < p \leq 0.01$, * $0.01 < p \leq 0.05$, ns $p > 0.05$).

Figure 3.15. Rescue studies on locomotion speed and displacement phenotypes caused by neuropeptide mutants *flp-1* and *nlp-12*

(**A-B**) Boxplots of translational forward locomotion speed (**A**) measured during a 4min interval at 21% oxygen and (**B**) of the behavioral change in response to the oxygen downshift, quantified as the relative difference between 60s intervals pre- and post-downshift, normalized to the interval pre-downshift.

(**C**) Mean ± SEM in gray of translational forward speed of all worms of population assays (~25 animals per assay) over time. Gray bar indicates oxygen concentration and dashed lines the downshift.

(**D-E**) Boxplots of effective displacement per 30 seconds (**D**) measured during a 3min interval at 21% oxygen and (**E**) of the behavioral change in response to the oxygen downshift, quantified as the difference between 60s intervals pre- and post-downshift.

Boxplots display median, interquartile range and 5-95 percentile whiskers. All strains were compared to wild type N2, and rescue strains against respective mutant as indicated, using one-way-ANOVA with Sidak's correction and calculated with n = number of experiments (~25 animals per assay): N2 n=10, *nlp-12* n=6, *nlp-12* rescue under *Pnlp-12* n=11, *flp-1* n=11, *flp-1* rescues *Pflp-1* n=10, *AVK* n=9, *AVE,AVA,RIG,AIY* n=9 and combination *AVK* plus *AVE,AVA,RIG,AIY n=9*. Reported expression of endogenous promoters: DVA only for *Pnlp-12* and AVK, AVA, AVE, AIY, RIG, RMG, AIA and M5 for *Pflp-1*. (**** $p \leq 0.0001$, *** $0.0001 < p \leq 0.001$, ** $0.001 < p \leq 0.01$, * $0.01 < p \leq 0.05$, ns $p > 0.05$).

3.4.2 Mutant postures are based on eigenworm shapes similar to wild type

To understand how impaired postures of manipulated worms affected crawling or steering motions, their body waves had to be decomposed in the same way as the wild type N2 data. However, the postural changes due to manipulation might also affect the underlying dominant shapes of the worms. This aspect had already been addressed previously: A variety of mutants with defects in body posture had been shown to give rise to similar eigenworms as wild type animals in an on-food paradigm (Brown et al., 2013). I could confirm this important aspect for my data acquired under starved / off-food conditions. Therefore I derived eigenworms via PCA from all pooled segment angle time series of two mutants with either increased (*flp-1* mutants) or decreased (*nlp-12* mutants) body curvature (Figure 3.16). Indeed, the extracted underlying shapes were similar to N2-derived eigenworms. But, eigenworms derived from high-curvature *flp-1* mutants displayed marginally increased wavelengths, while eigenworms underlying *nlp-12* mutant low-curvature postures displayed somewhat shorter wavelengths (especially eigenworm 1 and 2).
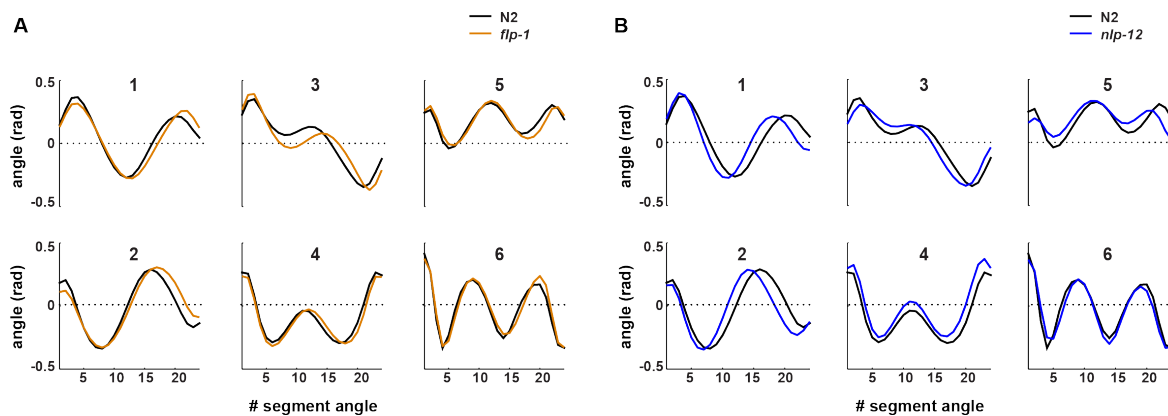
Figure 3.16. First six of 24 eigenworms from posture mutants and comparison to wild type eigenworms
Eigenworms were calculated by principal components analysis of all pooled time series (>= 20s duration) of worm segment angles of (**A**) *flp1* or (**B**) *nlp-12* and compared to wild type N2 eigenworms.

3.4.3 Regulation of crawling and steering motions through the peptidergic interneurons

Next, I performed body wave decomposition of manipulated worm strains by projecting their segment angles along the 24 wild type-derived eigenworms, as mutant-derived eigenworms did not differ greatly. This assured that crawling and steering motions of all strains were classified based on the same criteria (respective identical shapes EW1-2 or EW3-24) and enabled me to directly compare the distinct strains. By using the two-dimensional description of the body curvature-defective worms in terms of power of crawling and steering motions, the roles of peptidergic interneurons in adjusting locomotion strategies could be dissected into detail.

During non-stimulated travel behavior at 21% oxygen, low body wave power in *nlp-12* mutants and DVA-ablated animals resulted from deficient promotion of crawling waves while steering waves were not affected (or even slightly increased in *nlp-12* mutants). Exaggerated body wave power in *flp-1* mutants and AVK-ablated animals was caused by combined defective repression of crawling and steering waves. However, depletion of *flp-1* yielded more extreme crawling wave power, while AVK-ablation led mainly to disinhibition of steering motions (Figure 3.17 A-B). *flp-1* phenotypes could be restored to normal locomotion by specific expression in the AVK interneuron pair only, but also by separate expression from other *flp-1* expressing interneurons (AVA, AVE, RIG, AIY). *nlp-12* expression solely in DVA rescued *nlp-12* mutant phenotypes (Figure 3.18 A-B). The combined manipulation of *flp-1; nlp-12* mutant worms resulted in no effect on steering motions and an intermediate crawling phenotype compared to the single mutants at 21% oxygen, supporting the idea of two opposing parallel signals of FLP-1 and NLP-12. DVA ablation effects however, dominated the crawling phenotype of double-ablated (AVK-; DVA-) animals while steering motions of those animals were between the levels of the respective single ablations, revealing a role of DVA to support steering motions in the absence of AVK neurons (Figure 3.17 A-B).
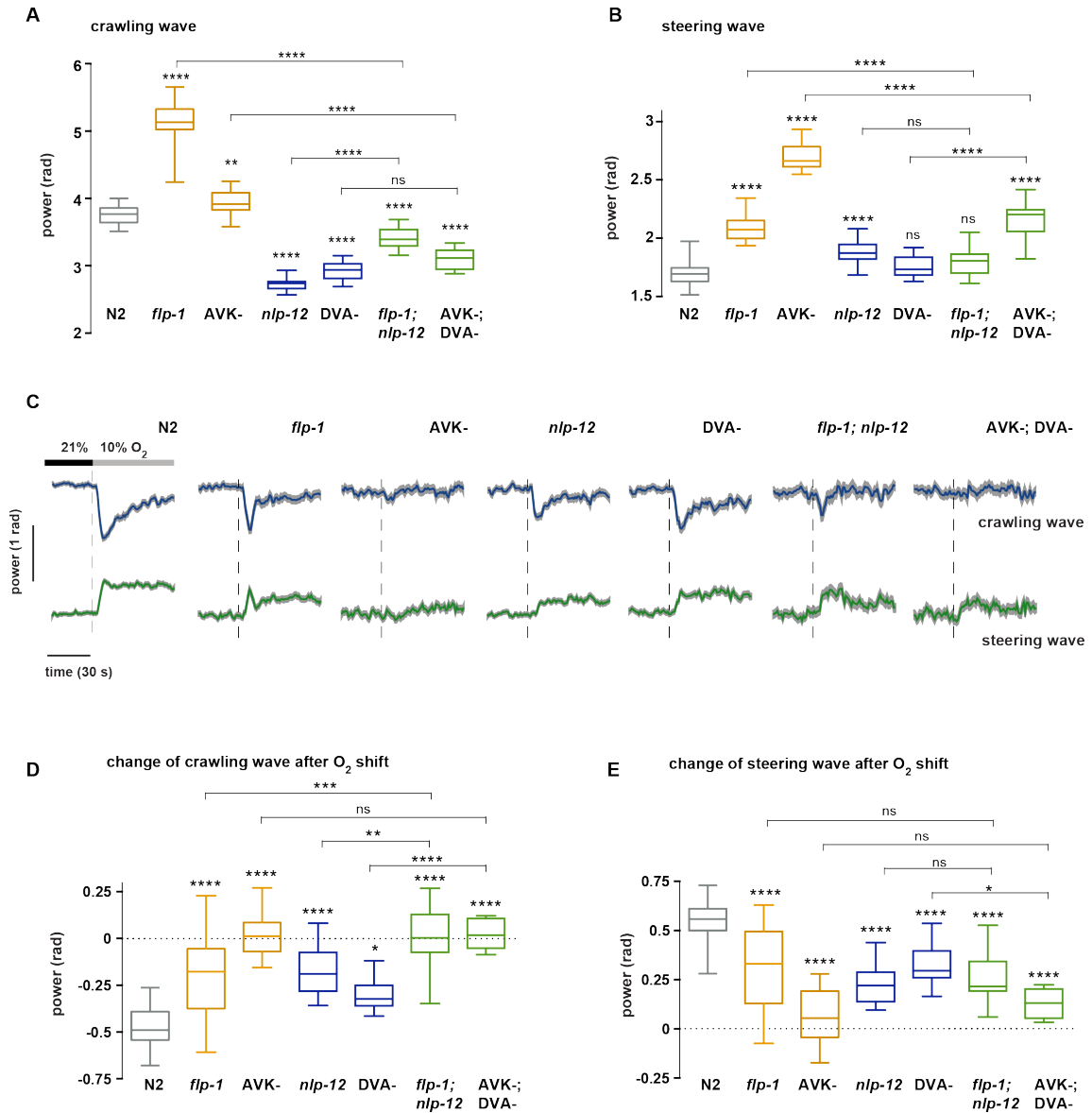
Figure 3.17. Regulation of crawling and steering motions by AVK and DVA interneurons and their neuropeptides FLP-1 and NLP-12

Boxplots of (**A**) crawling wave power and (**B**) steering wave power during forward locomotion measured within a 4min interval at 21% oxygen.

(**C**) Mean ± SEM in gray of all worms of population assays (~25 animals per assay) over time displaying the power of crawling wave (blue, top line) and steering wave (green, bottom line). Gray bar indicates oxygen concentration and dashed lines the downshift. Absolutes of traces are vertically aligned to emphasize differences in behavioral responses. (**D-E**) Boxplots of changes of (**D**) crawling wave power and (**E**) steering wave power in response to the oxygen downshift, quantified as the difference between 60s intervals pre- and post-downshift.

Boxplots display median, interquartile range and 5-95 percentile whiskers. All strains were compared to wild type N2, and selected genotypes as indicated, using one-way-ANOVA with Sidak's correction and calculated with n = number of experiments (~25 animals per assay): N2 n=36, *flp-1* n= 29, AVK- n=21, *nlp-12* n=21, DVA- n=13, *flp-1; nlp-12* n=12 and AVK-; DVA- n=10. (**** $p \leq 0.0001$, *** $0.0001 < p \leq 0.001$, ** $0.001 < p \leq 0.01$, * $0.01 < p \leq 0.05$, ns $p > 0.05$).

To elucidate effects on the transition between travel and search, I investigated the differences in crawling and steering wave power before and after oxygen downshift (Figure 3.17 C-E). I observed that any manipulation in the regulatory system of AVK – FLP-1 and DVA – NLP-12 caused deficiencies in accurately decreasing crawling motions or increasing steering motions, respectively.

The neuropeptide mutant phenotypes could be (partially) rescued by expression in the respective single interneurons (Figure 3.18 C-E). This implied a significant role of FLP-1 and NLP-12 neuropeptide signaling in altering the locomotion strategy from travel to local search following the oxygen downshift.

It was very interesting that the neuropeptide double mutant *flp-1; nlp-12* exhibited crawling and steering wave powers not too different from wild type levels during the 21% oxygen period. Thus, these worms could perform nearly normal traveling. However, they severely failed to transit into the searching mode after stimulation.

Figure 3.18. Rescue studies on crawling and steering phenotypes caused by neuropeptide mutants *flp-1* and *nlp-12*

Boxplots of (**A**) crawling wave power and (**B**) steering wave power during forward locomotion measured within a 4min interval at 21% oxygen.

(**C**) Mean ± SEM in gray of all worms of population assays (~25 animals per assay) over time displaying the power of crawling wave (blue, top line) and steering wave (green, bottom line). Gray bar indicates oxygen concentration and dashed lines the downshift. Absolutes of traces are vertically aligned to emphasize differences in behavioral responses.

Boxplots of changes of (**D**) crawling wave power and (**E**) steering wave power in response to the oxygen downshift, quantified as the difference between 60s intervals pre- and post-downshift.

Boxplots display median, interquartile range and 5-95 percentile whiskers. All strains were compared to wild type N2, and rescue strains against respective mutant as indicated, using one-way-ANOVA with Sidak's correction and calculated with n = number of experiments (~25 animals per assay): N2 n=10, *nlp-12* n=6, *nlp-12* rescue under *Pnlp-12* n=11, *flp-1* n=11, *flp-1* rescues *Pflp-1* n=10, *AVK* n=9, *AVE,AVA,RIG,AIY* n=9 and combination *AVK* plus *AVE,AVA,RIG,AIY* n=9. Reported expression of endogenous promoters: DVA only for *Pnlp-12* and AVK, AVA, AVE, AIY, RIG, RMG, AIA and M5 for *Pflp-1*. (**** $p \leq 0.0001$, *** $0.0001 < p \leq 0.001$, ** $0.001 < p \leq 0.01$, * $0.01 < p \leq 0.05$, ns $p > 0.05$).

The importance of FLP-1 and NLP-12 became even more evident when I stimulated *flp-1; nlp-12* double mutant worms with a gradual decreasing oxygen ramp. Crawling and steering wave power barely changed in response to the oxygen sensory stimulation (Figure 3.19 – compare to wild type in Figure 3.11).

In conclusion, the system of AVK and DVA interneurons signaling via the neuropeptides FLP-1 and NLP-12 was proven important in adjusting the strength of crawling and steering motions to facilitate a controlled change of strategy from travel to local search after oxygen-sensory stimulation. AVK activity was especially important to reduce steering motions whereas DVA activity mainly promoted crawling.
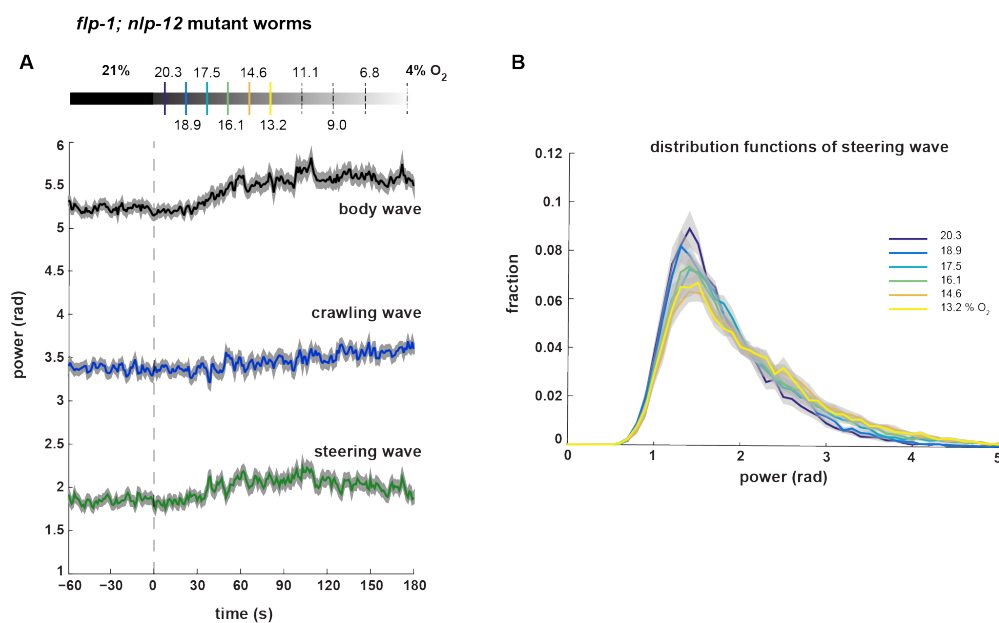
Figure 3.19. Gradual behavioral changes in response to an oxygen ramp depend on FLP-1 and NLP-12 neuropeptides.
Behavioral responses of *flp-1;nlp-12* mutant worms during forward movement to a decreasing oxygen ramp from 21 to 4% were analyzed in 15 population assays (~25 animals per assay).
(**A**) Mean ± SEM in gray of worm body wave (black), crawling wave (blue) and steering wave (green) of all worms from populations assays over time relative to oxygen stimulation onset (dashed line). Oxygen levels are indicated by gray bars.
(**B-C**) Mean (± SEM in gray) of relative distribution functions derived per assay (n=15) of (**B**) crawling and (**C**) steering wave power over 15-second consecutive intervals during the first half of the decreasing ramp. Colors indicate oxygen concentration of interval centers and are indicated in the oxygen bar in A.

One more aspect important for proper execution of locomotion strategies was the regulation of crawling frequency, which is tightly associated with locomotion speed (Figure 3.9 E). Thus the speed phenotypes observed in curvature mutants (Figure 3.14 A) were reflected in the respective bending frequencies of crawling waves (Figure 3.20) rather than their power (Figure 3.17 A). Importantly, the neuron DVA and neuropeptide FLP-1 each appeared to regulate only the power but not the frequency of crawling motions, implying that the two features can be regulated separately.
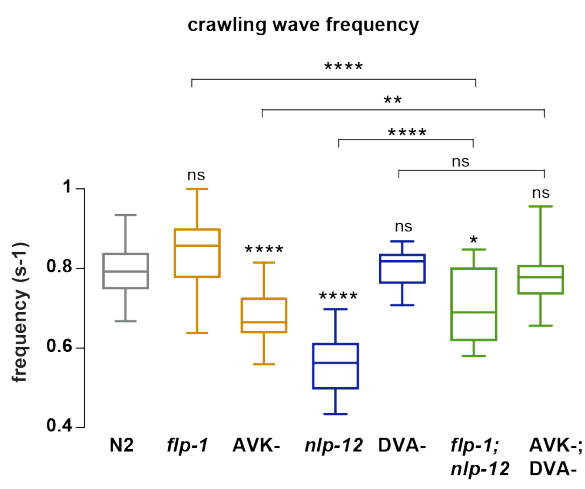
Figure 3.20. Regulation of crawling wave (bending) frequency
Frequency is measured as ventral or dorsal bends (half an undulation cycle) of mid-body segment angle #11 per second. Boxplots of crawling wave power frequency during forward locomotion measured within a 4min interval at 21% oxygen.
Boxplots display median, interquartile range and 5-95 percentile whiskers. All strains were compared to wild type N2, and selected genotypes as indicated, using one-way-ANOVA with Sidak's correction and calculated with n = number of experiments (~25 animals per assay): N2 n=36, *flp-1* n= 29, AVK- n=21, *nlp-12* n=21, DVA- n=13, *flp-1; nlp-12* n=12 and AVK-; DVA- n=10. (**** $p \leq 0.0001$, *** $0.0001 < p \leq 0.001$, ** $0.001 < p \leq 0.01$, * $0.01 < p \leq 0.05$, ns $p > 0.05$).

3.4.4 Body wave decomposition into crawling and steering waves based on mutant eigenworms

Mutant and wild type eigenworms were quite similar (Figure 3.16). Still, they displayed slight differences including distinct wavelengths. I wanted to investigate whether body wave decomposition of posture-defective worms based on their own respective eigenworms would yield similar results regarding the regulation of crawling and steering motions. Therefore I tested two mutant strains, with either increased (*flp-1* mutants) or decreased (*nlp-12* mutants) body curvature and compared body wave projections onto wild type and mutant derived eigenworms (Figure 3.21). For the high-curvature mutant *flp-1*, no significant differences in crawling and steering wave power were observed between the two different sets of eigenworms, during both non-stimulated travel and in response to stimulation. The low-curvature mutant *nlp-12* displayed the same crawling wave power during travel as wild type, and similar changes of both waves after sensory stimulation. However, its steering wave power based on the mutant eigenworms showed lower levels (more similar to wild type) compared to slightly increased power when calculated based on wild type eigenworms.

The overall results drew the same picture: In the absence of sensory stimulation, FLP-1 neuropeptides served to reduce crawling and steering motions whereas NLP-12 neuropeptides mainly (or only) functioned to promote crawling motions. After stimulation, both neuropeptides were essential to properly alter both types of motion.
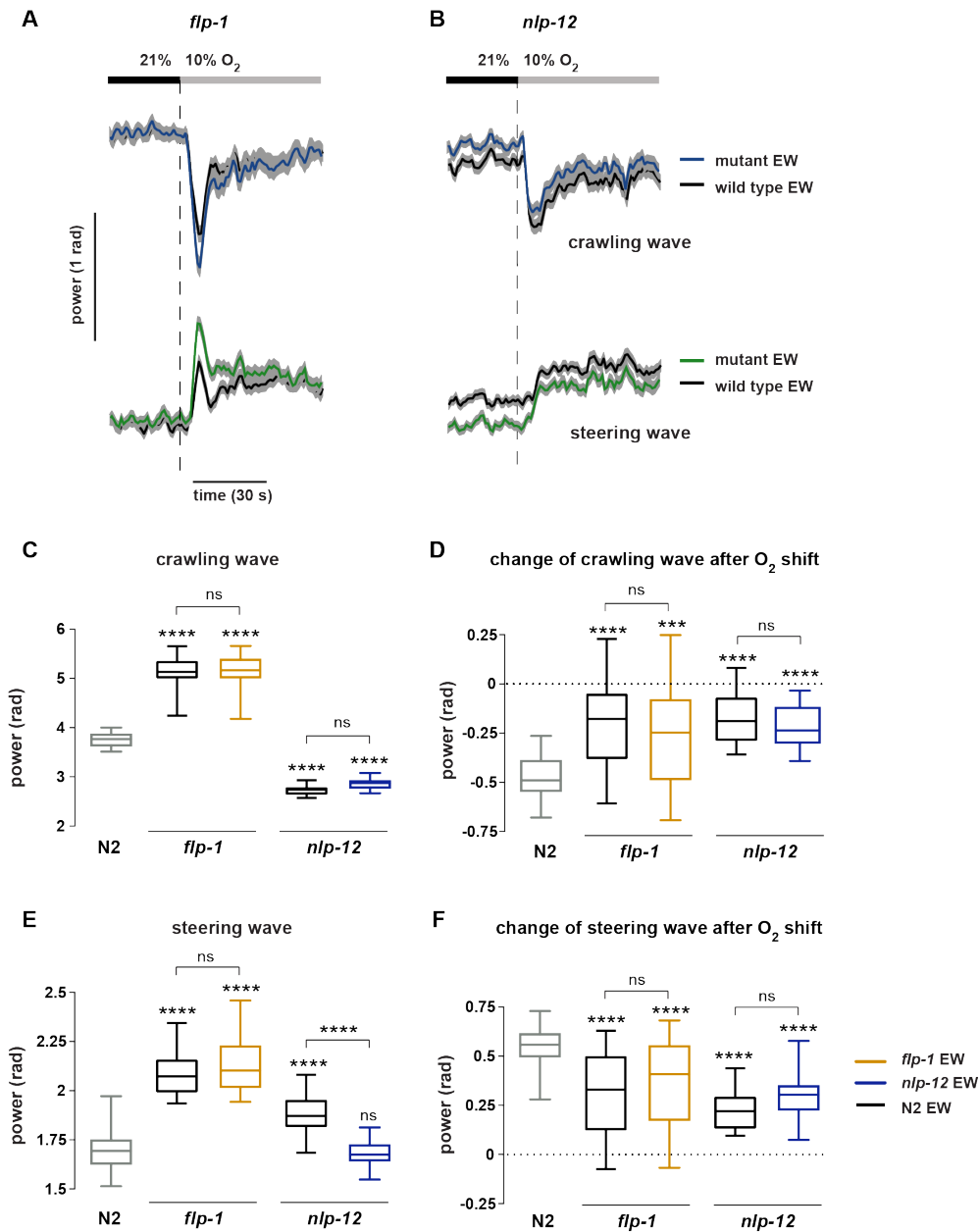
Figure 3.21. Crawling and steering wave derived from mutant eigenworms.
(**A-B**) Mean ± SEM in gray of all worms of population assays (~25 animals per assay) over time displaying the power of crawling wave (top line) and steering wave (bottom line). Gray bar indicates oxygen concentration and dashed lines the downshift. Absolutes of traces are vertically aligned to highlight behavioral responses. Colored or black traces are derived from respective mutant or wild type N2 eigenworms (EW), respectively. (**A**) *flp-1* and (**B**) *nlp-12* mutant animals.
(**C-F**) Boxplots of (**C-D**) crawling and (**E-F**) steering wave power during forward movement measured within a 4min interval at 21% oxygen (**C, E**) or (**D, F**) changes in response to the oxygen downshift, quantified as the difference between 60s intervals pre- and post-downshift. Colored or black boxplots display results from mutant or wild type N2 eigenworms (EW), respectively.
Boxplots display median, interquartile range and 5-95 percentile whiskers. Mutant strains were compared to wild type N2, and selected genotypes as indicated, using one-way-ANOVA with Sidak's correction and calculated with n = number of experiments (~25 animals per assay): N2 n=36, *flp-1* n= 29, *nlp-12* n=21. (**** $p \leq 0.0001$, *** $0.0001 < p \leq 0.001$, ** $0.001 < p \leq 0.01$, * $0.01 < p \leq 0.05$, ns $p > 0.05$).

3.5 Neural activity of interneuron AVK reflects locomotion speed and repression of steering motions

Having dissected the effects of cellular ablation on worm locomotion behavior, I sought to analyze how the neural activities of AVK and DVA neurons fit their roles in controlling worm postures during travel and local search behaviors. Therefore I performed high-magnification GCaMP fluorescence calcium-imaging of each neuron's cell body simultaneously with infrared behavioral recording of worms freely moving on agarose (Faumont et al., 2011) in an oxygen flow arena (1 hour starvation and off-food conditions). All recordings were done in a ratiometric fashion with a parallel calcium-insensitive mCherry fluorophore and the GCaMP /mCherry ratio was measured to assure the observed signals did not arise due to movement artifacts.

3.5.1 AVK neural activity reflects locomotion speed

Averaging multiple recordings of AVK neural activity revealed a depression of calcium signal after an oxygen downshift from 21% to 10%, when animals slowed down and increased their steering wave power (Figure 3.22 A). This significant depression in neural activity could not be detected when animals perceived the same stimulus but were immobilized in a microfluidic chip (Figure 3.22 B, D). The GCaMP /mCherry ratio change was not an artifact of animal movement as freely moving imaging experiments with worms expressing calcium-insensitive GFP and mCherry did not reveal ratio changes in response to oxygen stimulation (Figure 3.22 C, E).

AVK calcium transients reflected the locomotion speed on a single-animal basis, including movement in forward and reverse direction (Figure 3.23 A). Indeed signal cross-correlation analysis indicated a positive correlation between speed and AVK activity over a relatively long time scale peaking at r=0.35 with an average 1.7-second delay time of AVK signals lagging behind the animal's speed (Figure 3.23 B). After compensating for this lag time, I sorted all pooled AVK calcium signals over locomotion speed, which highlighted the positive relation between the two signals and was not seen in the GFP-expressing control animals. This was additionally confirmed by the calculation of linear correlation coefficients per animal (Figure 3.23 C-E). The positive correlation was persistent both before and after the oxygen downshift, indicating no modulation of this relationship by sensory stimulation or changes in locomotion strategy. Further, locomotion speed reflections in AVK activity were independent of movement direction (Figure 3.23 F-G), which had not been observed so far for *C. elegans* interneurons related to movement. For example the measured activity of the

interneuron pair RIB strongly correlates with speed only during forward and not during reverse movement (Kato et al., 2015, Li et al., 2014). Moreover a very recent study identifies that the activities of many interneurons reflect switches between forward and reverse movement, but show decent correlations to locomotion speed only in one direction (Kato et al., 2015).
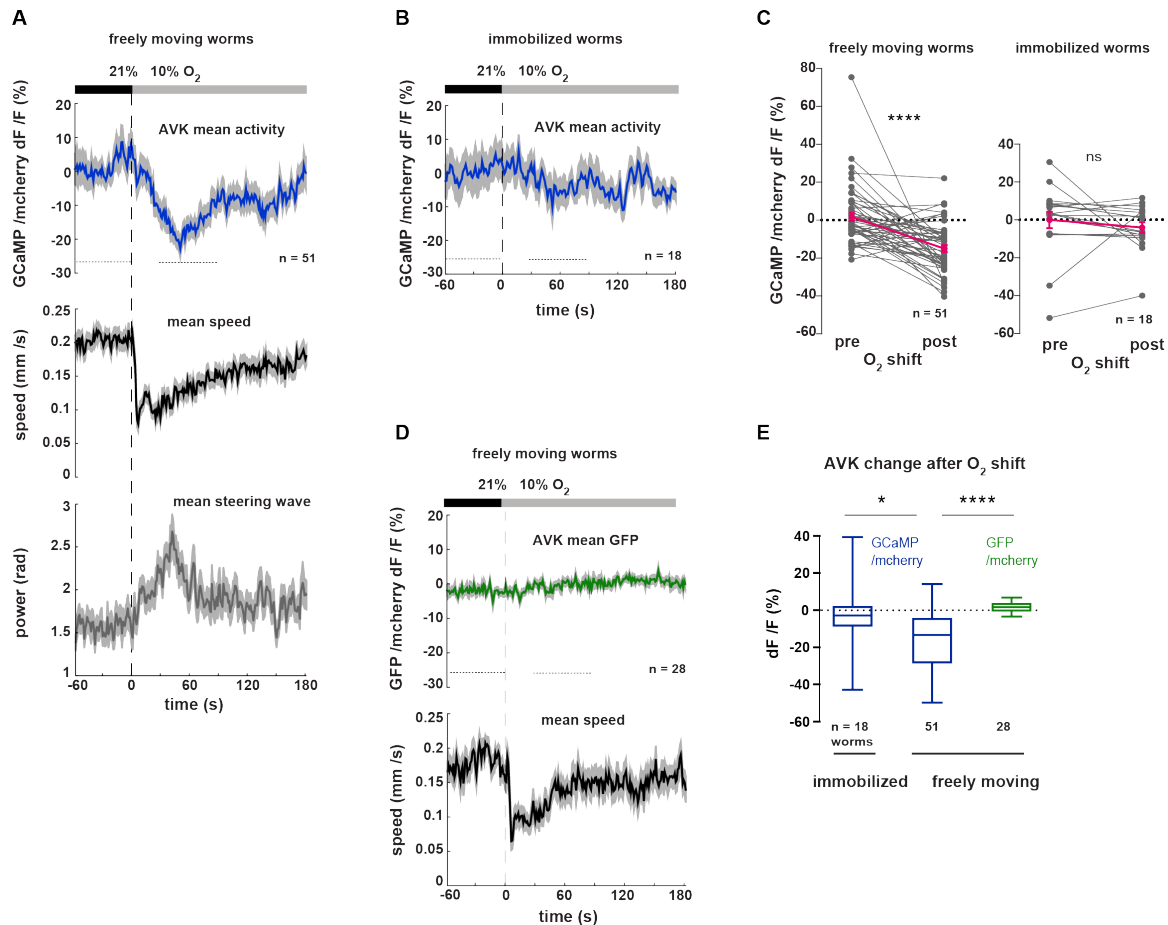
Figure 3.22. Neural activity of interneuron AVK reflects behavioral changes.
Neural activity of AVK neurons was measured by calcium imaging and is displayed as normalized ratio of GCaMP5K /mCherry fluorescence or for control calcium-insensitive GFP /mCherry. Worms were stimulated with an oxygen downshift from 21% to 10%.
(**A-C**) Trial-averaged mean ± SEM in gray over time relative to the shift (dashed line). Oxygen levels are indicated by gray bar. (**A**) Neural activity and behavior were recorded simultaneously from GCaMP-expressing animals (n=51) freely moving in an oxygen flow arena. Top: Neural activity, middle: locomotion speed and bottom: steering wave power. (**B**) Neural activity of worms (n=18) immobilized in a microfluidic oxygen-controlled chip. (**C**) Neural activity and locomotion speed from GFP-expressing animals (n=28) freely moving in an oxygen flow arena.
(**D**) Quantifications of 60s intervals pre- and post- oxygen downshift, highlighted with horizontal lines in A, B. Single animals are in gray and mean ± SEM in magenta. AVK activity significantly decreased in freely moving animals (**** p ≤ 0.0001), but did not change in immobilized worms (ns, p = 0.34, paired t-test).
(**E**) Quantification of AVK ratio change after the oxygen downshift, using two 60s intervals pre- and post-downshift (as highlighted with horizontal lines in Figure A-C). By one-way-ANOVA with Dunnett's correction, immobilized worms showed a significantly smaller ratio change (*p = 0.015) than freely moving worms (both expressing GCaMP). Ratio change of control GFP-expressing worms clearly differed (****p < 0.0001) from GCaMP-expressing worms (both freely moving).
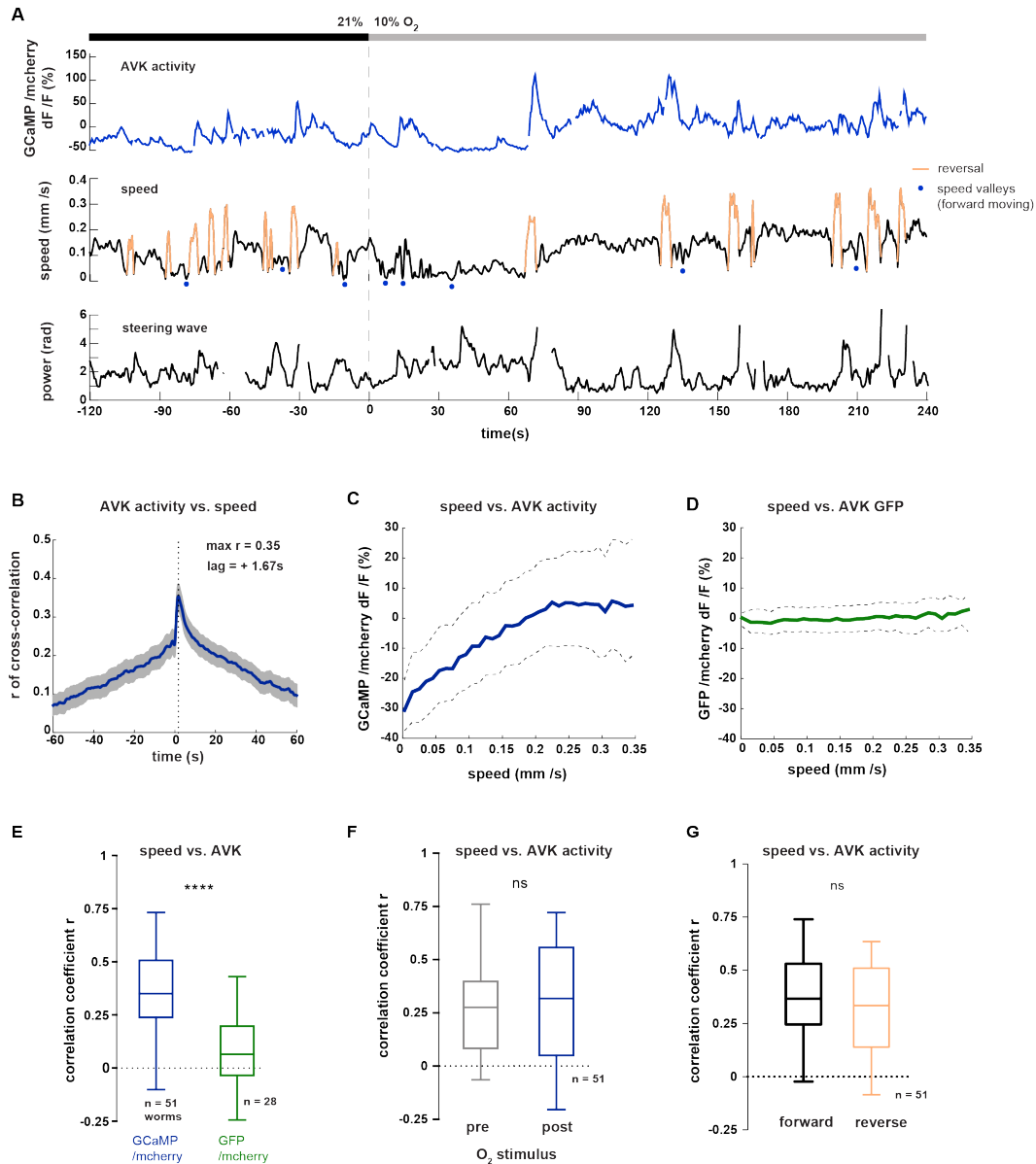
Figure 3.23. Neural activity of interneuron AVK correlates with locomotion speed.
Neural activity of AVK neurons was measured by calcium imaging and is displayed as normalized ratio of GCaMP5K /mCherry fluorescence or for control calcium-insensitive GFP /mCherry. Behavior was recorded simultaneously from animals freely moving in an oxygen flow arena and stimulated with an oxygen downshift from 21% to 10%.
(**A**) Exemplary recording displaying traces over time relative to downshift (dashed line) of neural activity (top), locomotion speed (middle) and steering wave power (bottom). Reverse movement is marked in color in the speed trace. Speed valleys during forward movement (see Figure 3.24) are marked by blue dots. Oxygen levels are indicated by gray bar.
(**B**) Cross-correlation function of AVK neural activity vs. locomotion speed, presented as mean ± SEM (n=51 worms). The correlation reaches its maximum when AVK activity lags 1.67s behind the speed. This lag time was compensated for in all following correlation analyses of speed vs. activity.
(**C-D**) Median and interquartile range from all pooled total recordings sorting AVK signal over median of locomotion speed bins (size= 0.01 mm /s). (**C**) GCaMP5K /mCherry and (**D**) control GFP /mCherry.
(**E-G**) Linear correlation coefficients between speed and AVK activity were calculated per worm. Boxplots display median, interquartile range and 5-95 percentile whiskers. Prior to calculations a lag time of 1.67s between the two signals was compensated for. (**E**) Total recordings of GCaMP-expressing worms showed significantly stronger correlation than GFP-expressing worms (unpaired t-test ****$p < 0.0001$). (**F**) Comparison of 120s intervals pre- and post-downshift. Paired t-test showed no significant difference ($p = 0.89$). (**G**) Comparison of forward and reverse locomotion. Unpaired t-test showed no significant difference ($p = 0.13$).

3.5.2 AVK neural activity is anti-correlated with steering motions

Consistent with AVK's role in suppressing steering wave motions, I noticed an inverse relation between AVK activity and steering wave power during forward motion, not present in the GFP-control animals, when sorting AVK signals over steering wave power or by calculating the linear correlation coefficients per animal (Figure 3.24 A-C). I analyzed only forward locomotion in analogy to the analyses of the worm population behavioral studies. As with the speed correlation, the negative correlation to steering motions was persistent both before and after the oxygen downshift, indicating no modulation of this relationship by sensory stimulation or change of locomotion strategy (Figure 3.24 D).

I investigated the relation of locomotion speed to AVK activity and steering motions further by calculating event-triggered averages aligning the data to speed valleys during forward locomotion (example events in Figure 3.23 A). Indeed, speed minima aligned with drops in AVK activity and peaks of steering wave power. Crawling and total body wave power showed no significant or smaller changes, respectively, in association with speed valleys (Figure 3.24 E-G). The AVK signal reduction was not an artifact caused by reduced motion as the GFP /mCherry ratio of control recordings did not change around the speed valley (Figure 3.24 H). Due to the importance of FLP-1 and NLP-12 neuropeptides in the regulation of steering motions, I investigated AVK neural activity in *flp-1; nlp-12* double mutants. The neuropeptides were not essential for AVK activity depression or for increases of steering motions when animals efficiently slowed down (Figure 3.24 I-L).

In conclusion, AVK interneurons reflect the animal's locomotion speed with a moderate delay of around 1.7 seconds, which is less than one undulation cycle (average ~2.5 seconds) but longer than pure GCaMP response kinetics (GCaMP5K: time to peak in response to action potential in mouse visual cortex (in vivo) was measured as t_{peak} = 0.06 seconds (Chen et al., 2013)). The absence of AVK depression in response to an oxygen downshift in immobilized worms indicates that AVK activity changes depend on or even monitor locomotion. Elevated activity of AVK suppresses steering motions during fast traveling movement whereas AVK down-regulation during slow movement facilitates steering important for local search strategy.
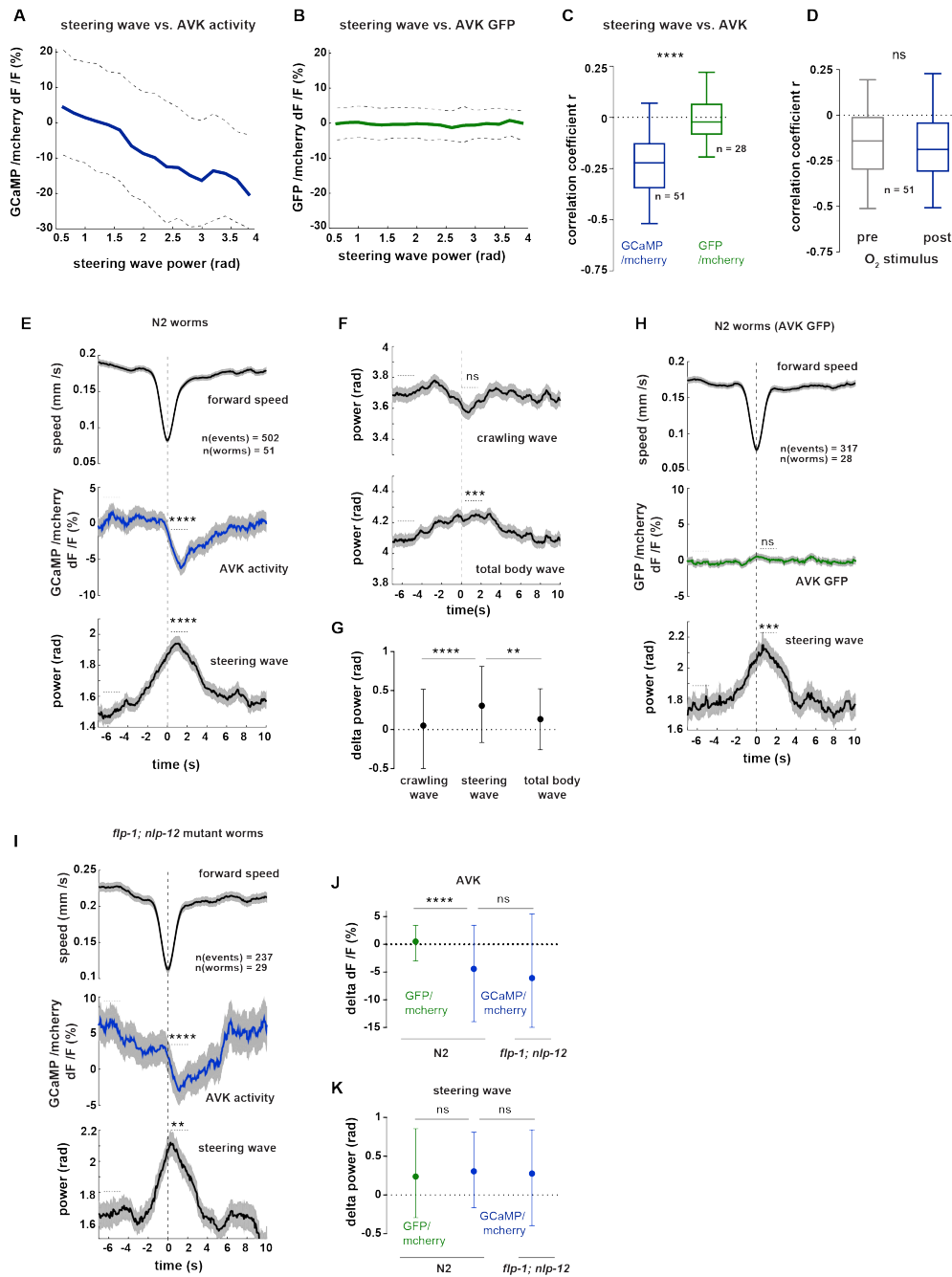
Figure 3.24. Neural activity of interneuron AVK is anti-correlated with steering motions.
Neural activity of AVK neurons was measured by calcium imaging and is displayed as normalized ratio of GCaMP5K /mCherry fluorescence or for control calcium-insensitive GFP /mCherry. Behavior was recorded simultaneously from animals freely moving in an oxygen flow arena and stimulated with an oxygen downshift from 21% to 10%.
(**A-B**) Median and interquartile range from all pooled total recordings sorting AVK signal over median of steering wave power bins (size = 0.2 rad) during forward locomotion. (**A**) GCaMP5K /mCherry and (**B**) GFP /mCherry.
(**C-D**) Linear correlation coefficients between steering wave power and AVK activity were calculated per worm. Boxplots display median, interquartile range and 5-95 percentile whiskers. (**C**) GCaMP-expressing worms had significantly stronger correlation than GFP-expressing worms (unpaired t-test **** p < 0.0001). (**D**) Comparison of 4min intervals pre- and post- oxygen downshift. Paired t-test showed no significant difference (p = 0.56).
(**E-K**) Alignment of AVK signal and indicated behaviors to speed valleys during forward movement (example events in Figure 3.23 A). (**E, F, H, I**) Event-triggered means ± SEM in gray with n = number of events as indicated. Wilcoxon matched-pairs signed rank tests compare 1.5s intervals pre- and post-event as indicated (**** p ≤ 0.0001, *** 0.0001 < p ≤ 0.001, ** 0.001 < p ≤ 0.01, * 0.01 < p ≤ 0.05, ns p > 0.05).

Figure 3.24. continued
(**E-F**) Wild type N2 worms expressing GCaMP, (**H**) wild type N2 worms expressing GFP and (**I**) *flp-1; nlp-12* mutant worms expressing GCaMP.
(**G**) Median and interquartile range from all events of wild type worms (data from E-F) comparing changes in power of the steering wave to crawling wave (p<0.0001) or total body wave (p=0.0011), respectively, via Kruskal-Wallis test with Dunn's correction. (**K-L**) Median and interquartile range from all events comparing changes of (**K**) AVK signal or (**L**) or steering wave power of GCaMP-expressing wild type worms to GFP-expressing wild type or GCaMP-expressing *flp-1; nlp-12* mutant worms (data from E, H, I) via Kruskal-Wallis test with Dunn's correction (ns p > 0.05 and **** p ≤ 0.0001).

3.6 Neural activity of interneuron DVA represents multiple behavior features

Next I investigated the neural activity from the single tail interneuron DVA in freely moving worms perceiving oxygen downshifts. DVA activity had been previously reported to represent dorso-ventral body-bending in tail-glued animals in a proprioceptive manner dependent on the pore-forming subunit *trp-4* of a stretch-sensitive channel (Kang et al., 2010; Li et al., 2006).

3.6.1 DVA neural activity does not continuously reflect a single behavior feature

I observed calcium fluctuations in DVA cell body, which were more complex than simple reflections of alternating dorso-ventral bends. An example recording illustrates calcium increases of varying magnitudes, occurring at 21% oxygen when the animals was rather fast and also after the stimulation with a downshift to 10% when the animal slowed down (Figure 3.25 A). Trial-averaging all recordings revealed a significant rise of DVA transients (Figure 3.25 B, D), when mean speed dropped and steering motions increased. This was not observed in control recordings of GFP /mCherry –expressing worms (Figure 3.25 C, E). Linear correlation coefficients calculated per animal between DVA activity and the investigated behavioral features yielded only very weak correlations. Consistent with the trial-averages, locomotion speed (during forward and reverse movement) or steering wave power displayed a weak negative or positive correlation, respectively, which was significantly greater than artificial relations extracted from control GFP-expressing worms (Figure 3.25 F). However, when I sorted all pooled DVA calcium signals over those two individual behavior features, the change of DVA signal over the range of the respective behavior was rather limited (Figure 3.25 G), arguing against an instantaneous behavior representation by DVA. Correlations calculated between DVA activity and the total body wave or crawling wave were not significantly different from GFP-controls (Figure 3.25 F). Using the instantaneous (signed or absolute) value or the amplitude of a single segment angle of head, mid-body or posterior body did not reveal higher correlation values for any of the waves (not shown). In conclusion, DVA neural activity did not reflect a single behavior feature over its range but appeared rather complex.
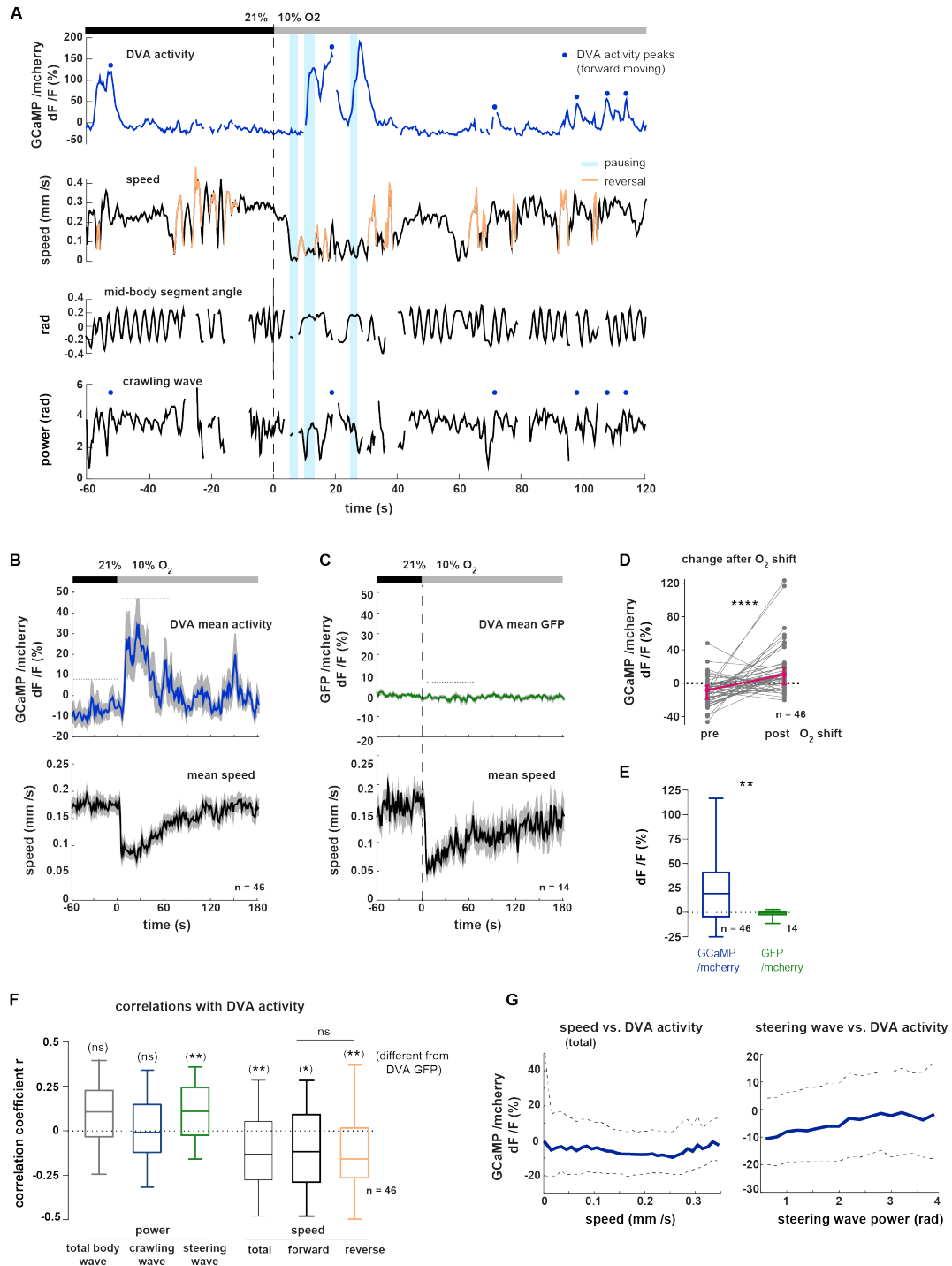
Figure 3.25. Neural activity of interneuron DVA does not reflect a single behavior feature.
Neural activity of DVA tail neuron was measured by calcium imaging and is displayed as normalized ratio of GCaMP5K /mCherry fluorescence or for control calcium-insensitive GFP /mCherry. Behavior was recorded simultaneously from animals freely moving in an oxygen flow arena. Animals were stimulated with an oxygen downshift from 21% to 10%.
(**A**) Exemplary recording displaying traces over time relative to downshift (dashed line) of neural activity, locomotion speed, mid-body segment angle #11 and crawling wave power. Reverse movement is marked in color in the speed trace, and blue shadings highlight phases when the animal paused. DVA transient peaks during forward movement (see Figure 3.27) are marked by blue dots. Oxygen levels are indicated by gray bar.
(**B-C**) Trial-averaged mean ± SEM in gray of neural activity or locomotion speed over time relative to the shift (dashed line). Oxygen levels are indicated by gray bar. (**B**) Recordings of GCaMP-expressing animals (n=46). (**C**) Recordings from GFP-expressing animals (n=14).

(**D-E**) Quantifications of 60s intervals pre- and post- oxygen downshift, highlighted with horizontal lines in B, C. (**D**) Single animals in gray and median + interquartile range in magenta. DVA transients significantly increased in GCaMP-expressing animals after the stimulus (**** $p < 0.0001$, Wilcoxon matched-pairs signed rank test). (**E**) Ratio change of GCaMP- and control GFP-expressing animals was significantly different, Mann-Whitney test (** $p = 0.003$).
 (**F**) Linear correlation coefficients between indicated behaviors and DVA activity were calculated per worm. Boxplots display median, interquartile range and 5-95 percentile whiskers. Statistical results compared GCaMP-expressing worms to control GFP-expressing worms (in parenthesis) or forward vs. reverse speed (as indicated) by one-way-ANOVA with Sidak's correction (** $0.001 < p \leq 0.01$, * $0.01 < p \leq 0.05$, ns $p > 0.05$).
(**G**) Median and interquartile range from all pooled total recordings sorting DVA ratio over median of (total) locomotion speed (size = 0.01 mm /s) or (total) steering wave power bins (size = 0.2 rad).

3.6.2 Reversals and pause phases associate with elevated DVA neural activity

The individual recordings indicated an accumulation of DVA activity increases around reversals. After the oxygen downshift, when DVA activity rose on average (Figure 3.25 B), animals increased movement in reverse direction (fraction of all recorded animals in Figure 3.26 A and compare reversal frequency in Figure 3.3 D). Aligning DVA activity to reversal starts indeed highlighted that reversals were associated with elevated DVA activity, which was not the case for GFP control worms (Figure 3.26 B-C). Naturally, the locomotion speed dropped at transitions from forward to reverse movement followed by acceleration. Further the total body wave power initially dropped after the transition, reflected in a drop of crawling wave power, and eventually rose over its previous baseline, which corresponded to an increase of steering wave power (Figure 3.26 D). Thus DVA neural activity resembled best the steering wave power changes around reversal starts.

Yet, the association of DVA activity and reversal onset was not very strict. First, their relative timing was not tight. On average DVA activity increased already 5-10 seconds before the reversal start (Figure 3.26 B). Second, the magnitude of DVA ratio increases varied strongly, implying a more complex DVA signal than a binary on-off representation of reversal state (see whiskers of boxplot in Figure 3.26 C and examples in Figure 3.25 A and 3.26 E). DVA activity simply showed a tendency to increase around phases of reverse movement. However, I could not observe reliable signaling of reversal onset as has been shown for other interneurons such as AVA, AIB, AIZ or RIM (Faumont et al., 2011; Kawano et al., 2011; Li et al., 2014; Piggott et al., 2011; Gordus et al., 2015; Kato et al., 2015).

I further noticed very strong DVA transient rises when the worms slowed down extremely and (nearly) completely stopped moving, i.e. paused (Figure 3.26 E). This happened often shortly after the oxygen downshift, but also occasionally during 21% oxygen (fraction of pausing animals in Figure 3.26 A). I identified pausing (or moving)

phases as short stretches of movement below (or above) a speed cutoff (0.05 mm /s). For animals that paused for at least 60s (interruptedly) over the total recording (usually 12 minutes), I could reveal an association of pause phases with relatively elevated mean DVA neural activity compared to moving phases (Figure 3.26 F). GFP-control recordings proved that this effect was not a movement artifact. As worms often remained in a bent posture during pausing, the power of crawling wave and total body wave did not significantly differ between pausing and moving phases. But animals increased their steering wave power during pausing postures (Figure 3.26 G and see examples in 3.26 E).

In summary, DVA neural activity was relatively increased during non-forward moving phases, i.e. reversals and pausing phases, during which animals increased the strength of their steering motions, indicative of a positive relation between DVA activity and steering motions.
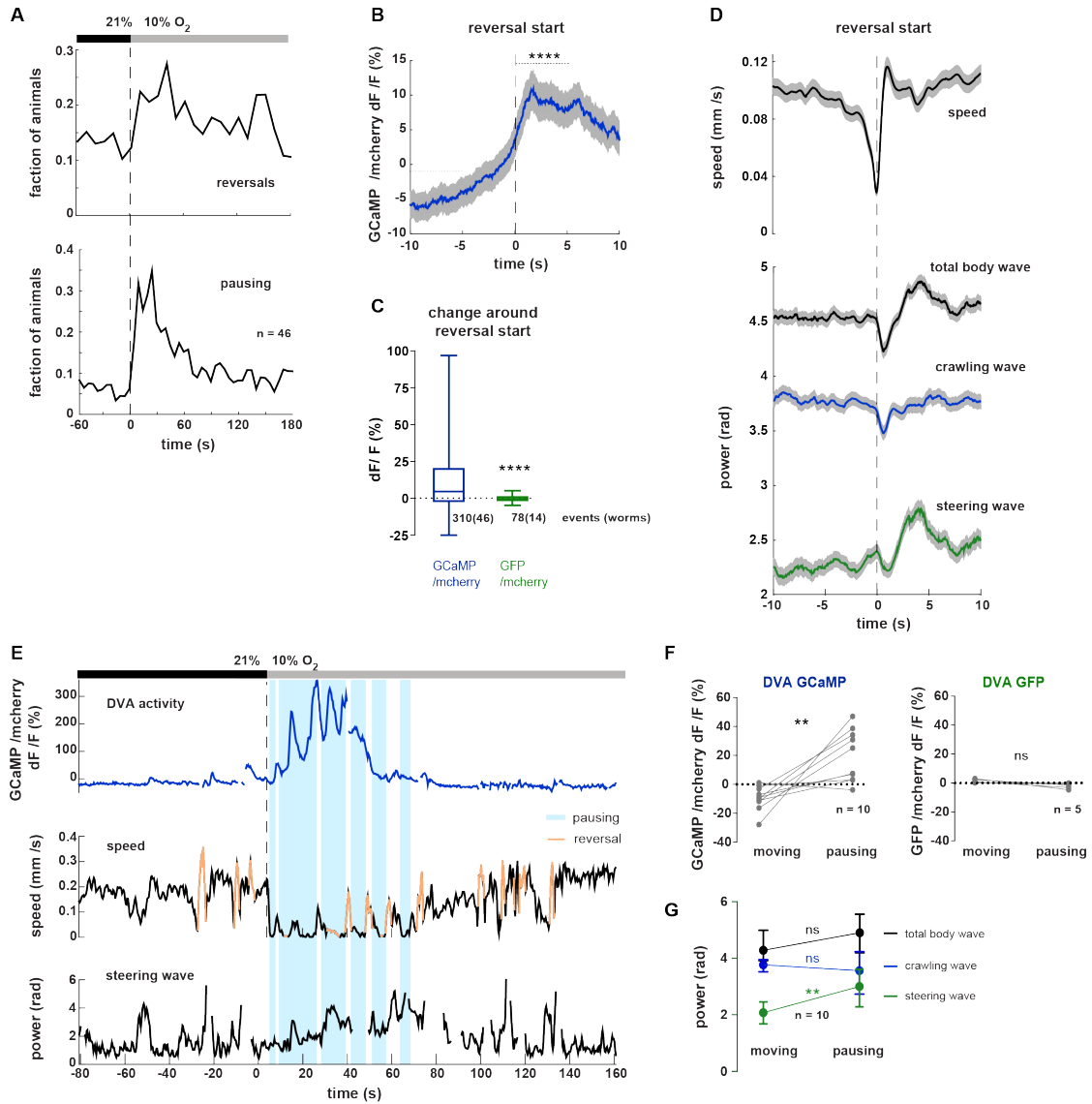
Figure 3.26. Neural activity of interneuron DVA indicates reversals and pause phases.
Neural activity of DVA tail neuron was measured by calcium imaging and is displayed as normalized ratio of GCaMP5K /mCherry fluorescence or for control calcium-insensitive GFP /mCherry. Behavior was recorded simultaneously from animals freely moving in an oxygen flow arena. Animals were stimulated with an oxygen downshift from 21% to 10%.
(**A**) Fraction of all recorded GCaMP-expressing worms (n=46, same animals as in Figure 3.25) reversing (top) or pausing (bottom) over time relative to the shift (dashed line). Oxygen levels are indicated by gray bar.
(**B-D**) Alignment of DVA transients and indicated behaviors to reversal starts occurring during a 4min interval at 21% oxygen. Event-triggered means ± SEM in gray of GCaMP-expressing worms showing (**B**) DVA transients or (**D**) locomotion speed and wave powers relative to reversal start. (**B**) Wilcoxon matched-pairs signed rank test compares DVA transients during 5s intervals before and after reversal start as indicated (**** p < 0.0001). (**C**) Ratio change after reversal start of GCaMP- and control GFP-expressing animals was significantly different, Mann-Whitney test (**** p < 0.0001).
(**E**) Exemplary recording displaying traces over time relative to downshift (dashed line) of neural activity (top), locomotion speed (middle) and steering wave power (bottom). Reverse movement is marked in color in the speed trace, and blue shadings highlight phases when the animal paused. Oxygen levels are indicated by gray bar.
(**F-G**) Comparison of mean levels of DVA ratio or wave power during moving and pausing phases from worms that were pausing at least 60s of the recording time (with interruptions). (**F**) GCaMP-expressing animals (n=10) increased DVA transients (** p < 0.0059) while control GFP-expressing animals did not (ns p = 0.0625, Wilcoxon matched-pairs signed rank tests).
(**G**) Median and interquartile range of wave power from same GCaMP-expressing worms (n=10) as in (F) (ns p > 0.05, ** p = 0.0020, Wilcoxon matched-pairs signed rank tests).

3.6.3 DVA neural activity increases correspond to gains in strength of forward crawling motion

The worm population behavioral studies of DVA-ablated animals had revealed a function of DVA to promote crawling motions during forward locomotion. The demonstrated increases of DVA activity in association with reversals and pauses might occlude a relation of DVA activity and forward crawling motions. Therefore, I next analyzed data during which animals were exclusively moving in forward direction (forward runs) after excluding reversals and pausing phases.

The oxygen downshift, which caused a slow-down of locomotion, did not evoke pausing in all animals (maximum fraction < 0.4, Figure 3.26 A). The locomotion speed of animals in forward runs still significantly decreased after the stimulation, in contrast to DVA activity, which did not significantly change during forward runs (Figure 3.27 A-B). This means that the calcium signal rise after stimulation indeed represented pausing phases and reversals but not behavioral changes during forward runs. Interestingly, the crawling wave power during forward runs did not significantly change after stimulation either, under the conditions of the freely moving calcium imaging experiments, and was in this way similar to DVA activity. Nevertheless, there was no continuous relation between crawling wave power and DVA activity during forward runs. Sorting DVA signals over crawling wave power or calculating linear correlation coefficients (in comparison to GFP-controls) displayed no meaningful association over the range of crawling motions (Figure 3.27 C-D).

The fact that DVA activity did not reflect crawling wave power in a continuous manner did not exclude a relation of strong calcium fluctuations and behavior. Thus, I calculated event-triggered averages aligning crawling wave power to DVA activity peaks during forward runs (example events in Figure 3.25 A). Increases of DVA activity in fact corresponded to gains of crawling wave power (Figure 3.27 E). Moreover, steering wave power was depressed during these events while the total body wave did not display significant changes. These alignments did not change between the different oxygen levels, i.e. during travel and local search phases (data not shown).

As FLP-1 and NLP-12 neuropeptides had been proven important for regulating crawling motions in the course of this study, I further investigated the relation of DVA activity and crawling in neuropeptide mutants. Absence of the DVA-specific NLP-12 peptides supporting crawling did not significantly interfere with this association, nor did the absence of crawling-repressive FLP-1 peptides (Figure 3.27 F-G). However, the

combined mutations in *flp-1; nlp*-12 mutant animals resulted in an impairment of this association.

In summary, increases in DVA activity during forward runs corresponded to gains of crawling motion strength, which might reflect an instructive role of DVA in promoting crawling dependent on the presence of NLP-12 and FLP-1 neuropeptides. While steering motions were rather inversely related to DVA activity during forward runs, they exhibited a positive association during reversals and pausing phases. Overall, DVA neural activity seems to represent multiple behavioral features of animal movement.
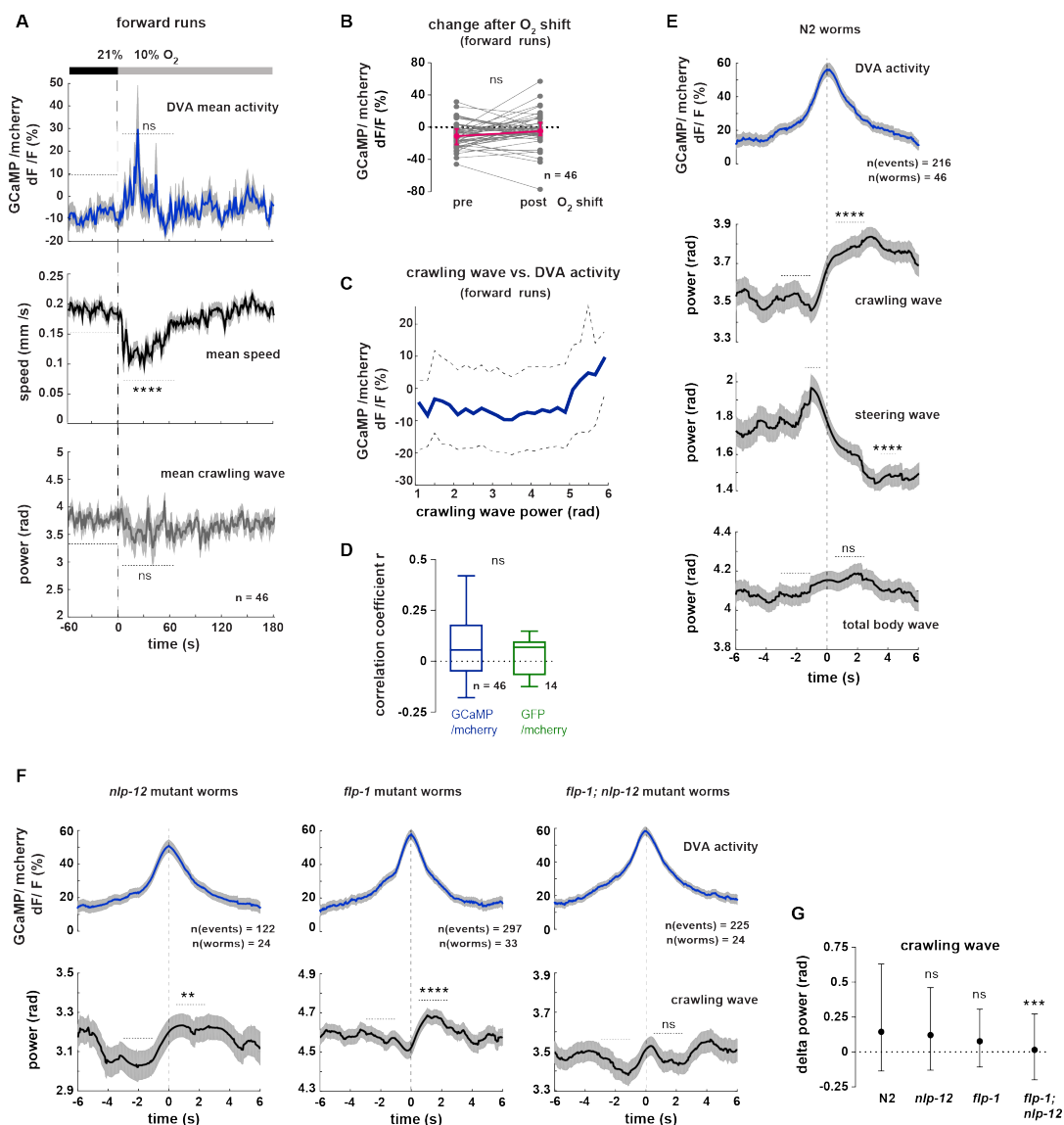
Figure 3.27. Gains of crawling motion strength align with DVA activity peaks during forward runs. Neural activity of DVA tail neuron was measured by calcium imaging and is displayed as normalized ratio of GCaMP5K /mCherry fluorescence or for control calcium-insensitive GFP /mCherry. Behavior was recorded simultaneously from animals freely moving in an oxygen flow arena. Animals were stimulated with an oxygen downshift from 21% to 10%.

Figure 3.27. *continued*
(**A**) Trial-averaged mean ± SEM in gray over time relative to the shift (dashed line) and comparisons of 60s intervals (horizontal lines) pre- and post-stimulus by Wilcoxon matched-pairs signed rank tests. Only data during forward runs are shown, i.e. reversals and pause phases were excluded (n=46, same animals as in Figure 3.25). Top: DVA neural activity (ns p=0.13), middle: locomotion speed (**** p<0.0001) and bottom: crawling wave power (ns p=0.053). Quantifications of neural activity of single animals are also shown in (**B**) in gray and median + interquartile range in magenta.
(**C**) Median and interquartile range from all pooled total recordings sorting DVA signal over median of crawling wave power bins (size= 0.2 rad) during forward runs, i.e. reversals and pause phases excluded.
(**D**) Linear correlation coefficients between crawling wave power and DVA activity were calculated per worm. Boxplots display median, interquartile range and 5-95 percentile whiskers. GCaMP-expressing worms did not exhibit significantly different correlation than GFP-expressing worms (unpaired t-test ns p=0.46).
(**E-F**) Alignment of indicated behaviors to DVA activity peaks during forward runs (example events in Figure 3.25 A). Event-triggered means ± SEM in gray with n = number of events as indicated. Wilcoxon matched-pairs signed rank tests compare 1s or 2s intervals pre- and post-event as indicated (**** p ≤ 0.0001, *** 0.0001 < p ≤ 0.001, ** 0.001 < p ≤ 0.01, * 0.01 < p ≤ 0.05, ns p > 0.05). (**E**) Wild type N2 worms and (**F**) mutant worms: *nlp-12*, *flp-1* and *flp-1; nlp-12*.
(**G**) Median and interquartile range from all events (data from E-F) comparing changes in crawling wave power of mutant and wild type worms via Kruskal-Wallis test with Dunn's correction (ns p > 0.05 and *** p = 0.009).

3.7 Role of mechano-transduction channel subunit TRP-4 in regulation of locomotion

Another previously reported gene involved in the regulation of worm body curvature is *trp-4*, which encodes a transient receptor potential (TRP) protein that is the pore-forming subunit of a stretch-sensitive channel (Kang et al., 2010). It is expressed in the dopaminergic mechanosensitive neurons PDE, ADE and CEP and in the interneurons DVC and DVA (Li et al., 2006). Its mutation leads to increased body curvature and this effect can be rescued by specific expression in DVA. This is very interesting, as DVA ablation in wild type and also in *trp-4* mutant animals causes the opposite phenotype. Further, *trp-4* has been shown to be essential for DVA calcium fluctuations caused by body bending in tail-glued animals and therefore has been proposed to serve a proprioceptive function in DVA (Li et al., 2006).

Due to the effects on worm posture and the link to DVA signaling, I investigated the role of TRP-4 in the regulation of locomotion strategies by performing worm population assays under oxygen stimulation with *trp-4* mutant animals. Through calcium imaging of DVA activity in freely moving *trp-4* mutant animals, I aimed to determine which features of DVA activity depended on the function of TRP-4.

3.7.1 TRP-4-dependent sensation converges onto NLP-12 signaling and is parallel to FLP-1 signaling

Exaggerated body curvatures and resulting increased body wave power of worms mutant for *trp-4* were also observed under 1-hour starvation conditions during forward locomotion at 21% oxygen (Figure 3.28 A-B). Otherwise these animals showed wild type levels of forward locomotion speed during the travel phase at 21% oxygen, a normal slowing response to the oxygen downshift and only very mild impairments of displacement rate (Figure 3.28 C-G). The neuropeptide mutant *flp-1* shared high body curvature and wild type traveling speed levels with the *trp-4* mutant. However, those two genes did not appear to share the same signaling pathway, as *flp-1; trp-4* mutant animals showed extremely high-curved body postures and body wave power different from each single mutant (Figure 3.28 A-B). Moreover, the combined mutations caused a significant reduction of locomotion speed during travel at 21% oxygen (possibly as a result of the extreme postures) and only a brief slow-down after stimulation. Thus the effective displacement was severely hampered and could be only weakly altered (Figure 3.28 C-G).

Mutation of *nlp-12* suppressed the *trp-4* mutant-dependent high-curvature phenotype towards levels of the *nlp-12* single mutant (Figure 3.28 A-B). Additionally, *nlp-12; trp-4* mutant worms reflected *nlp-12* single mutants in their inability to properly alter displacement after stimulation (Figure 3.28 G). Consistent with the reported action of TRP-4 and NLP-12 within DVA this suggests that TRP-4–mediated mechano-sensation converges onto NLP-12 signaling (at least) in terms of body curvature regulation. Yet, speed levels during travel of the double mutant were in between those of the respective single mutants (Figure 3.28 C, D). Thus, TRP-4 must be involved in restricting speed, mediated independent of NLP-12 signaling (which serves to promote speed). TRP-4–mediated regulation of bending frequency, and therefore speed, via the dopaminergic neurons ADE, CEP and PDE (which do not express NLP-12) had been previously reported, namely a speed-reducing function in animals moving on bacterial food lawns. Off-food, *trp-4* mutation did not affect bending frequency (Li et al., 2006). Finally, functional TRP-4 seems to further reduce locomotion speed in animals that are slow due to other reasons, i.e. wild type worms moving on food or *nlp-12* mutant worms moving off-food.

The receptor CKR-2 has been shown to bind NLP-12 neuropeptides, to mediate the NLP-12-dependent increase of synaptic transmission at cholinergic neuromuscular junctions and to exert similar effects on locomotion speed as NLP-12 (Hu et al., 2011;

Janssen et al., 2008). However, *ckr-2* mutants tested in the oxygen stimulation population assays did not exhibit *nlp-12*-like phenotypes but instead showed wild type postures and locomotion speed under off-food / starvation conditions. Thus, the NLP-12-dependent regulation of these behaviors must rely on other or at least additional receptors.
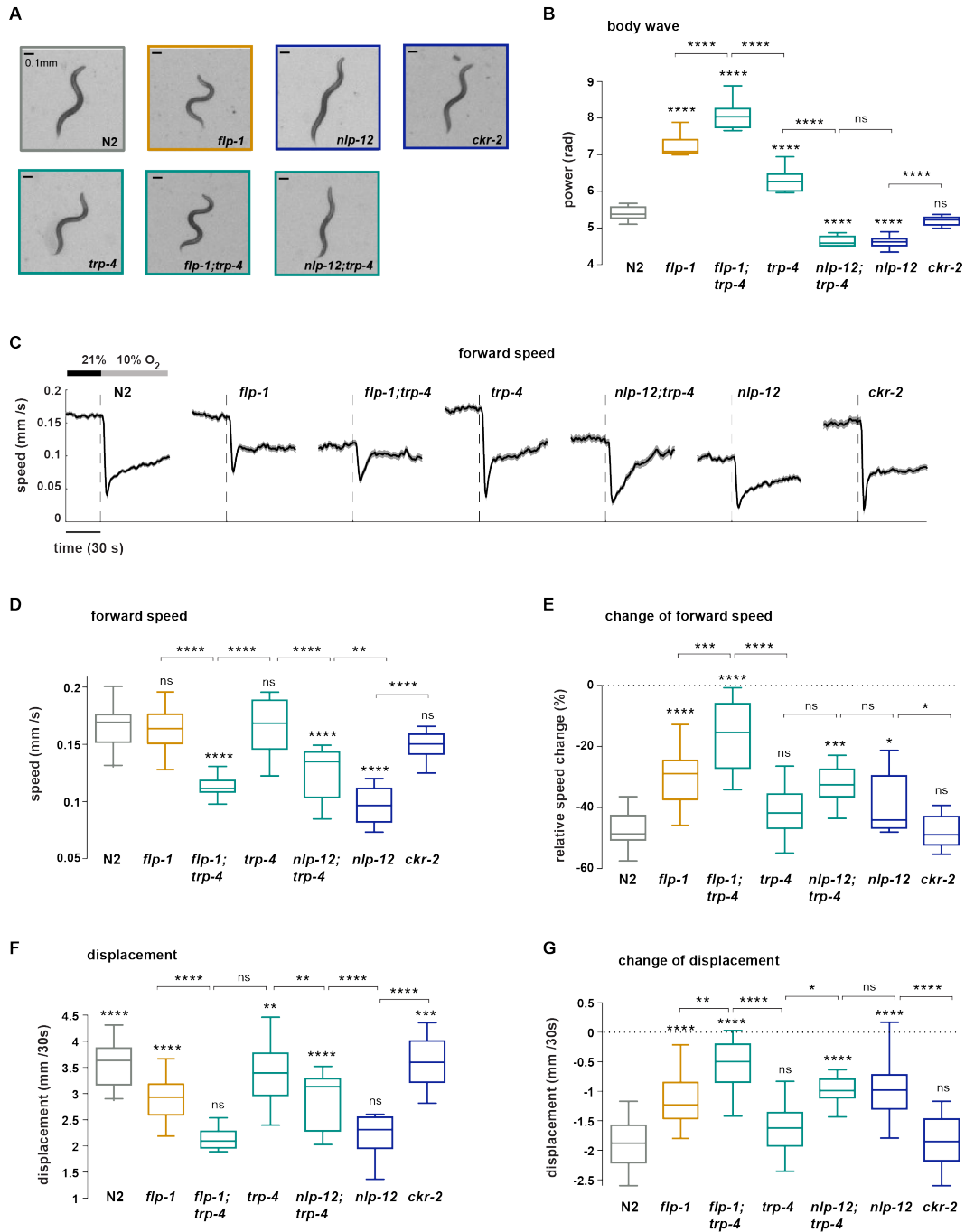
Figure 3.28

Figure 3.28. TRP-4 –dependent regulation of body posture and locomotion
(**A**) Representative video frames during forward motion at 21% oxygen of wild type (N2) and mutant worms illustrating effects on body curvature**.** Heads are pointing upwards. Scale bars are 0.1mm. (N2, *flp-1* and *nlp-12* images are the same as in Figure 3.13 A)
(**B**) Boxplots of total body wave power (during forward locomotion) measured during a 4min interval at 21% oxygen.
(**C**) Mean ± SEM in gray of all worms of population assays (~25 animals per assay) over time displaying translational forward speed. Gray bar indicates oxygen concentration and dashed lines the downshift.
(**D-E**) Boxplots of translational forward locomotion speed (**D**) measured during a 4min interval at 21% oxygen and (**E**) of the behavioral change in response to the oxygen downshift, quantified as the relative difference between 60s intervals pre- and post-shift, normalized to the interval pre-shift.
(**F-G**) Boxplots of effective displacement per 30 seconds (**F**) measured during a 3min interval at 21% oxygen and (**G**) of the behavioral change in response to the oxygen downshift, quantified as the difference between 60s intervals pre- and post-shift. Boxplots display median, interquartile range and 5-95 percentile whiskers. All strains were compared to wild type N2, and selected genotypes as indicated, using one-way-ANOVA with Sidak's correction and calculated with n = number of experiments (~25 animals per assay): (B) N2 n=26, *flp-1* n=18, *flp-1; trp-4* n=12, *trp-4* n=16, *trp-4; nlp-12* n=8, *nlp-12* n=15, *ckr-2* n=10. (**** $p \leq 0.0001$, *** $0.0001 < p \leq 0.001$, ** $0.001 < p \leq 0.01$, * $0.01 < p \leq 0.05$, ns $p > 0.05$).

The increased body wave power of *trp-4* mutant animals was decomposed into both enhanced crawling and steering wave power (Figure 3.29 A-B). Similar to the normal change of speed after oxygen-sensory stimulation, *trp-4* mutants were not impaired in altering crawling and steering motions (Figure 3.29 C-E). The extremely high-curved postures of *flp-1; trp-4* mutants, which were even stronger than those of each respective single mutant, were caused by strongly enhanced steering motions (Figure 3.29 B) while crawling motions were similar to those of *flp-1*. The change of crawling and steering wave power was severely diminished (Figure 3.29 C-E). Phenotypes of *nlp-12; trp-4* mutants resembled those of *nlp-12*. Thus, regulation of crawling and steering via TRP-4 likely converges onto NLP-12 signaling.

In summary, TRP-4-dependent mechano-sensory signaling involved in the regulation of crawling and steering motions appeared to be parallel to FLP-1 signaling and upstream of NLP-12 signaling. This supports the theory that FLP-1 and NLP-12 themselves are parallel regulators of posture and locomotion strategies instead of members of the same single pathway.
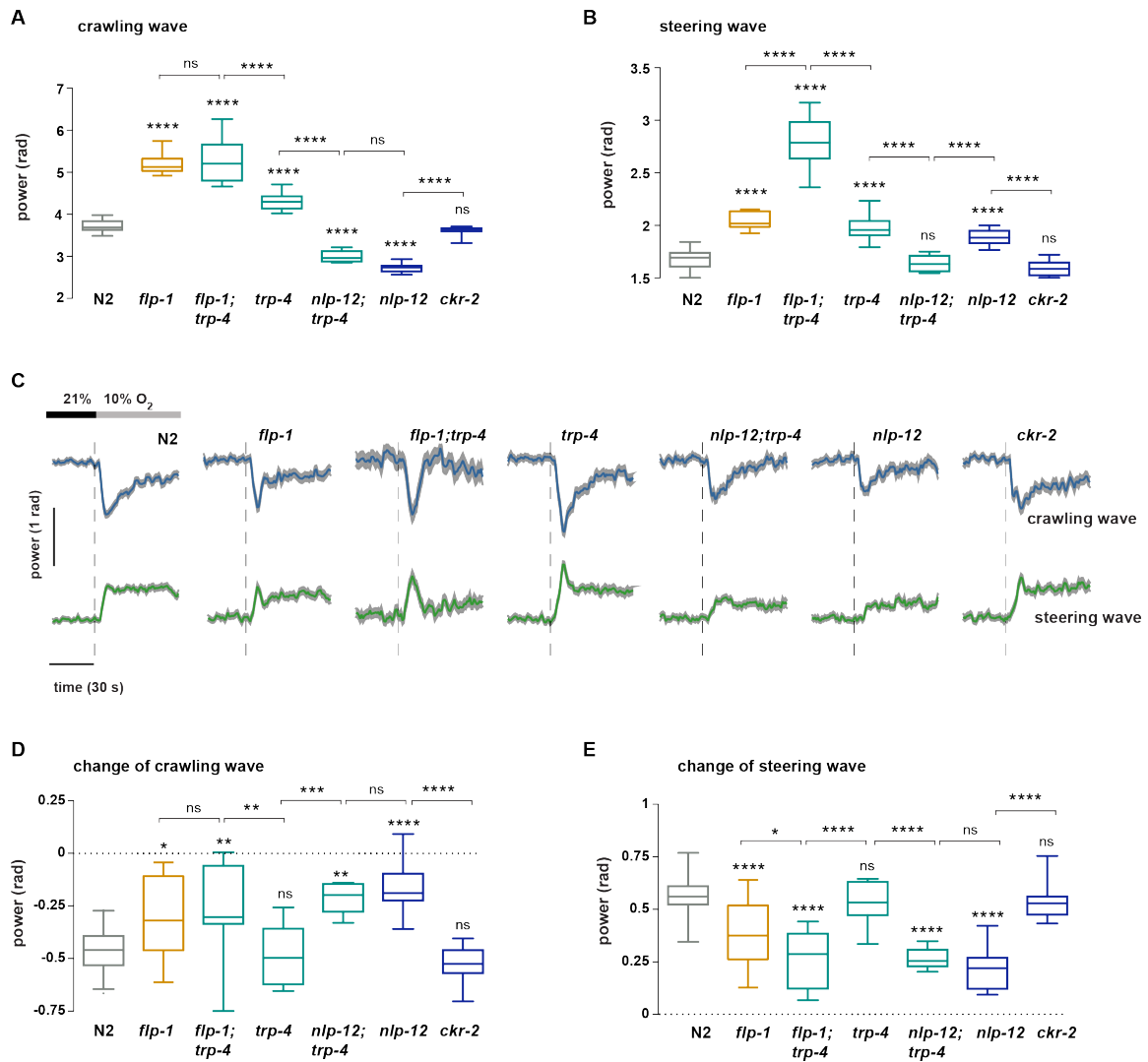
Figure 3.29. TRP-4 –dependent regulation of crawling and steering wave
Boxplots of (**A**) crawling wave power and (**B**) steering wave power during forward locomotion measured within a 4min interval at 21% oxygen.
(**C**) Mean ± SEM in gray of all worms of population assays (~25 animals per assay) over time displaying the power of crawling wave (blue, top line) and steering wave (green, bottom line). Gray bar indicates oxygen concentration and dashed lines the downshift. Absolutes of traces are vertically aligned to emphasize differences in behavioral responses.
(**D-E**) Boxplots of changes of (**D**) crawling wave power and (**E**) steering wave power in response to the oxygen downshift, quantified as the difference between 60s intervals pre- and post-shift. Boxplots display median, interquartile range and 5-95 percentile whiskers. All strains were compared to wild type N2, and selected genotypes as indicated, using one-way-ANOVA with Sidak's correction and calculated with n = number of experiments (~25 animals per assay): (B) N2 n=26, *flp-1* n=18, *flp-1; trp-4* n=12, *trp-4* n=16, *trp-4; nlp-12* n=8, *nlp-12* n=15, *ckr-2* n=10. (**** $p \leq 0.0001$, *** $0.0001 < p \leq 0.001$, ** $0.001 < p \leq 0.01$, * $0.01 < p \leq 0.05$, ns $p > 0.05$).

3.7.2 DVA neural activity during disrupted TRP-4 dependent proprioceptive signaling

The previously reported function of TRP-4 within DVA (in tail-glued animals) is to mediate proprioceptive responses to body bending (Li et al., 2006). However, under freely moving conditions, DVA activity did not simply reflect alternating body bends (see section 3.6). I sought to investigate TRP-4's role in DVA neural activity while animals were freely moving. Strong calcium transients were observed also in *trp-4* mutant worms (example in Figure 3.30 A). When animals occasionally paused, DVA activity was higher compared to phases when animals were moving (Figure 3.30 B). The association of DVA activity peaks and gains in crawling wave strength persisted also in the mutants (Figure 3.30 C-D). But DVA calcium transient increases associated with reversals were diminished in the absence of functional TRP-4, while steering wave power still properly increased during reversals (Figure 3.30 E-I). Despite a tendency of the mean DVA ratio to increase around the reversal start (Figure 3.30 E), a paired test of DVA ratio before and after the reversal start revealed no significant increase and the ratio changes accumulated around a median close to zero percent (Figure 3.30 F, H). In contrast, the DVA ratio increase in wild type worms was highly significant (Figure 3.26 B). This could suggest that DVA neural activity reflects increases in steering motions during reversals via TRP-4-mediated proprioceptive mechano-sensation.

In summary, DVA neural activity was not completely abolished by *trp-4* mutation, but instead I could not detect striking differences in calcium transients during forward movement or pausing phases. The only observed impairments concerned DVA signal increases associated with reversals.
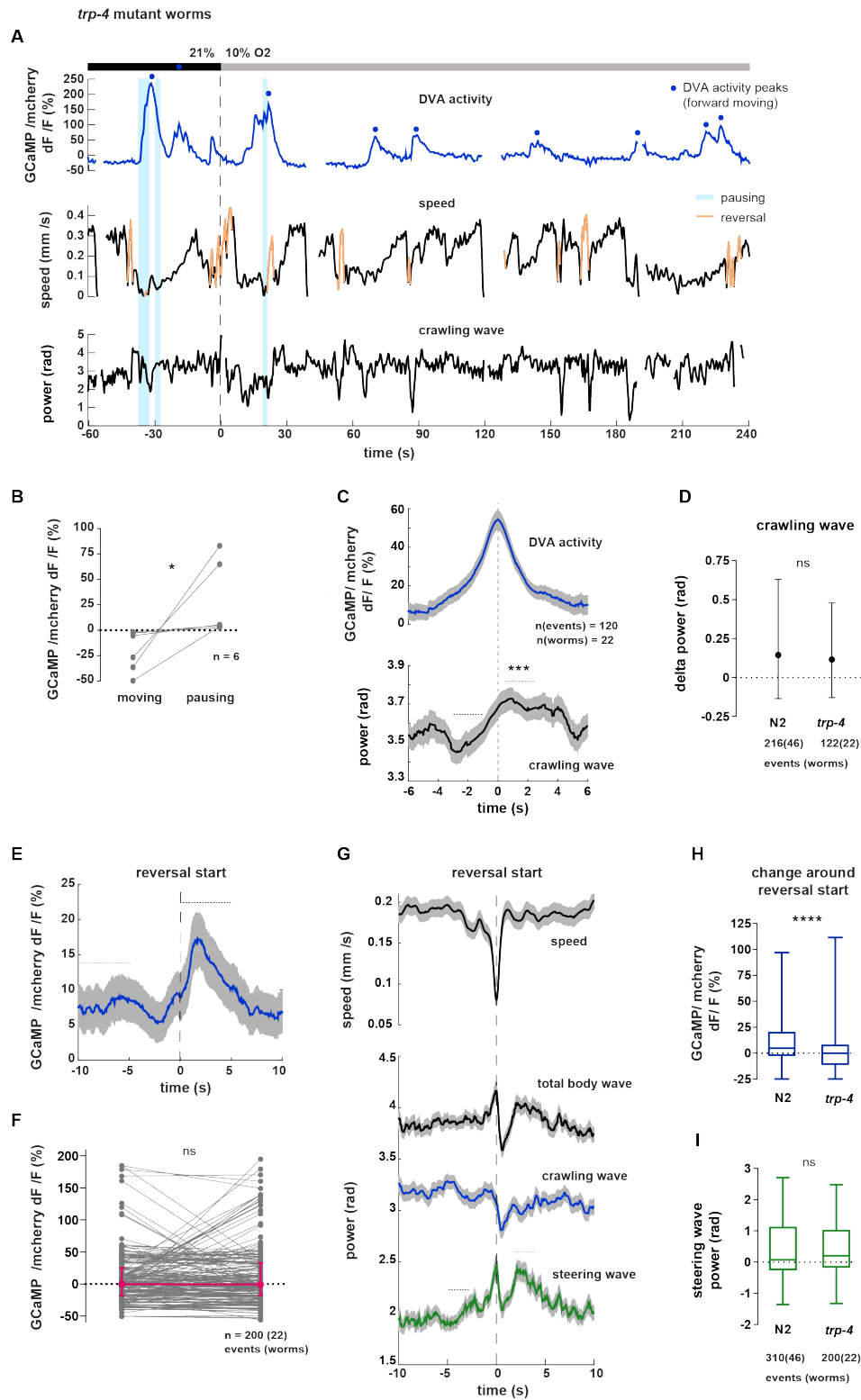
Figure 3.30. Neural activity of interneuron DVA in *trp-4* mutant worms
Neural activity of DVA neuron was measured by calcium imaging and is displayed as normalized ratio of GCaMP5K /mCherry fluorescence. Behavior was recorded simultaneously from animals freely moving in an oxygen flow arena. Animals were stimulated with an oxygen downshift from 21% to 10%. If not indicated otherwise, animals were mutant for mechano-transduction channel subunit *trp-4*.
(**A**) Exemplary recording displaying traces over time relative to downshift (dashed line) of neural activity (top), locomotion speed (middle) and crawling wave power (bottom). Reverse movement is marked in color in the speed trace, and blue shadings highlight phases when the animal paused. Oxygen levels are indicated by gray bar.

Figure 3.30 *continued*
(**B**) Comparison of mean levels of DVA ratio during moving and pausing phases from worms that were at least 60s of the recording time (with interruptions) pausing (* p = 0.031, Wilcoxon matched-pairs signed rank tests).
(**C**) Alignment of crawling wave power to DVA activity peaks during forward runs (example events in A). Event-triggered means ± SEM in gray with n = number of events as indicated. Wilcoxon matched-pairs signed rank tests compare 2s intervals pre- and post-event as indicated (*** p = 0.0005).
(**D**) Median and interquartile range from all events (data from C or wild type data from Figure 3.27E) comparing changes in crawling wave power of mutant and wild type worms via Kruskal-Wallis test with Dunn's correction (ns p > 0.99, test was performed with data of wild type and other mutants from Figure 3.27 G).
(**E-I**) Alignment of DVA transients and indicated behaviors to reversal starts occurring during a 4min interval at 21% oxygen. Event-triggered means ± SEM in gray of (**E**) DVA transients or (**G**) locomotion speed and wave powers relative to reversal start. (**F**) Wilcoxon matched-pairs signed rank test compares 5s intervals pre- and post- reversal start of DVA transients as indicated in E (ns p = 0.82). Change of (**H**) DVA ratio or (**I**) crawling wave power around reversal start of wild type (N2) and *trp-4* mutant worms. Comparison via Mann-Whitney test (**** p < 0.0001, ns p = 0.23).

4 Discussion

For efficient navigation through an environment most animals employ various locomotion strategies. To cover large distances, fast and regular movements are beneficial, while a more detailed exploration of the local environment often relies on flexible and less regular motions. This raises the questions of how animals control these distinct, stereotypic or more flexible motions and how they coordinate (combine or switch between) the different motion types to yield distinct locomotion strategies. I have addressed these questions using the undulatory locomotion of *C. elegans* as a model.

Initially, I showed that the food-deprived nematode travels distances along fairly straight paths by producing regular waves along its entire body (body wave). After oxygen-sensory stimulation, it switches to a local search strategy, which is characterized by slow movement and irregular postures, supporting frequent and flexible changes in heading direction in order to explore the local environment.

4.1 Superposition of crawling and steering motions can explain worm locomotion behaviors

Having observed the two distinct natures of the nematode's motions (regular vs. irregular) and building on previously reported low-dimensionality of worm postures (Stephens et al., 2008), I split the worm's body wave into two motion patterns: a regular crawling wave generating the thrust for forward (or backward) progression and an overlaid more flexible and irregular steering wave controlling steering and turning maneuvers to adjust the animal's heading direction (Figure 4.1). The decomposition illustrates that also strongly bent postures like deep omega turns have a crawling, i.e. thrust-producing motion pattern, to assure forward progression during the turn. It is the magnitude of the superimposed steering wave that determines the postural outcome and therefore the extent of directional change. Very powerful steering waves cause very deep bends that lead to drastic directional changes (turning) whereas subtler steering waves generate milder directional changes (steering maneuvers). However, there is no clear cut-off between steering and turning.

body   crawling steering
wave   wave   wave

{ = } + (
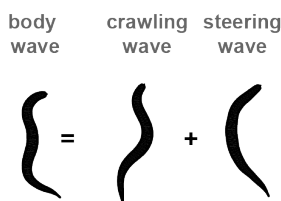
Figure 4.1. Concept of parallel crawling and steering waves
Worm body wave motions can be decomposed into parallel crawling and steering motions.

The decomposition method makes it possible to selectively and quantitatively capture the specific behavioral features of worm postures that are simultaneously up- or down-regulated, respectively, after sensory stimulation. Thereby it explains the relatively subtle changes reflected in the total body wave power accompanying the severe behavioral changes: The crawling wave decreases in strength while animals down-regulate traveling pace and regularity of postures. At the same time the steering wave increases in strength leading to more complex postures to better explore the local environment.

For the body wave decomposition, I built on the reported finding from Stephens *et al.* that combinations of the first two most dominant shapes underlying all worm postures (eigenworms, see sections 2.3.6 and 3.2.1) describe a regular wave along the worm's body that corresponds to forward and backward crawling, while increases along the third eigenworm associate with changes of heading direction (Stephens et al., 2008; 2010). Instead of describing worm postures via projection amplitudes along a subset of the derived eigenworms, I multiplied subsets (1-2 or 3-24) of projection amplitudes with their respective eigenworm shapes and summed them afterwards to retrieve descriptions via 24 segment angles. This decomposition approach therefore simply splits each of the measured 24 segment angles of the body wave into two additive angles by using the underlying eigenworms as criteria specifying crawling or steering motions.

The generated crawling wave patterns are very regular and the steering wave patterns also display a surprisingly organized structure (example in Figure 3.6). Cross-correlation between selected segment angles further strengthens the highly regular character of the crawling wave and shows that steering motions are also adjusted in a coordinated manner along the body. Interestingly, while crawling wave head and mid-body segments are bent into opposing directions (negatively correlate), steering wave head and mid-body segments are bent in the same direction (positively correlate). This implies that the two parallel motion patterns have different waveforms. The crawling wave constitutes a (sinusoidal) S-shape while strong steering waves often adopt a C-shape (reconstructed shapes in Figure 3.6). Although the two waves show quite distinct properties, they are not totally temporally uncoupled from each other, but display a phase-locked relation with adjustments of crawling motions ~0.6 seconds ahead of steering motions. This is consistent with the previously reported coupling between the wave described by projections along eigenworms 1-2 and the projection amplitude along eigenworm 3 (Stephens et al., 2008).

For further characterization of the two parallel waves I calculated the power as a measure of the wave's absolute strength along the whole worm body and thereby eventually employed two dimensions to specify worm body waves. Steering wave power is positively related to track curvature, which measures how strongly worms change their heading directions, i.e. steer. This strongly implicates an active role of the steering wave in the regulation of steering and turning. The crawling wave seems to contribute much less to steering maneuvers as its power barely varies along the range of track curvature. Crawling wave power presents a positive association with locomotion speed and therefore highlights its role in promoting travel across distances. (Yet, the main parameter controlling the worms' speed is rather thought to be the bending frequency of the crawling wave, which is strongly correlated to speed. The interrelation of the parameters power, frequency and speed is discussed in section 4.3.)

Previous studies dividing worms into 48-100 segment angles have revealed that four eigenworms are sufficient to describe over 95% or 93% of total variance of worm postures, of worms moving both off (Stephens et al., 2008) or on food (Brown et al., 2013), respectively. Here, eigenworms derived from 24 inter-segment angles produce similar shapes, while six eigenworms are necessary to account for 93% of worm posture variance. The moderate change of variance contribution might be due to the slightly different conditions (1-hour starvation) or simply due to lower resolution of worm images, which result in less precise skeleton extraction compared to previous studies.

The interesting fact that wild type and diverse mutant worm strains rely on similar dominant shapes (Brown et al., 2013), was confirmed in this study for high- and low-curvature mutants. Nevertheless, eigenworms retrieved from mutant worms with aberrant worm postures differ slightly from those of wild type worms. They show modestly increased or decreased wavelengths, respectively. Performing body wave decomposition using the mutant-derived eigenworms, however, does not yield considerable differences concerning the regulation of crawling and steering motions through the respective neuropeptide genes. Moreover, (wild type) worm postures under non-stimulated and stimulated conditions, while animals preferably perform traveling or searching behaviors, respectively, rely on very similar dominant shapes. This means that different locomotion strategies use one shared space of dominant shapes, which enables comparison of crawling and steering waves between periods before and after the sensory stimulation.

4.2 Model: Interneurons AVK and DVA modulate crawling and steering motions

Through the investigation of manipulated worm strains with aberrant postures, I could identify parts of the neural control system regulating crawling and steering motions. I characterized two posture-modulating counter-acting interneuron classes, AVK and DVA, employing FLP-1 or NLP-12 neuropeptide signaling, respectively. A potential model drawn from this study (Figure 4.2) suggests the neuron class AVK as an important repressor of steering motions during travel. At the same time it also restricts crawling motions, but to a lesser extent. Inhibitory regulation of both types of motions, but especially crawling motions, is achieved with the help of FLP-1 neuropeptides. Steering motions are controlled partially independent of FLP-1, possibly via AVK's relatively rich network of gap junction connections (Varshney et al., 2011).

AVK neural activity reflects the animal's locomotion speed and is therefore down-regulated when the animal slows down after an oxygen decrease. High AVK neural activity further reflects low steering wave power during travel. Reduction of AVK activity relieves its repression of steering motions and enables the animal to perform local search behavior. This is reflected in the anti-correlation of AVK activity and steering power. AVK further exerts a speed-stimulating function (not shown in the diagram), which might be a direct regulation of crawling wave frequency, or an indirect effect of stronger steering motions interfering with faster movement.

The interneuron DVA employs NLP-12 neuropeptides to promote powerful and frequent crawling motions and thereby exhibits positive speed regulation. NLP-12-mediated effects on the strength of crawling motions are counteracted by the stretch-sensitive channel subunit TRP-4 (Kang et al., 2010), potentially inhibiting NLP-12 release. This is probably a cell-autonomous function as TRP-4 functions within DVA to inhibit high body curvature (Li et al., 2006).
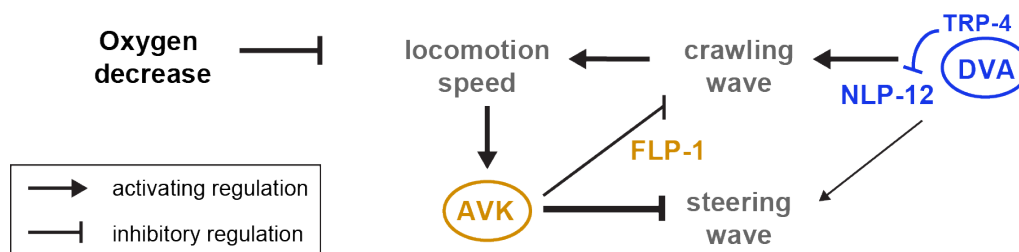
Figure 4.2. Control of crawling and steering via peptidergic AVK and DVA
An oxygen decrease evokes a slowing response, reflected by a decline of AVK neural activity, which relieves repression of crawling and especially steering motions, partially mediated via FLP-1. DVA promotes crawling motions (and to a minor degree steering motions) by employing NLP-12 neuropeptides, which is inhibited by TRP-4-mediated signaling.

The counter-parts AVK and DVA seem to affect body postures via distinct parallel pathways because, in the absence of sensory stimulation, body postures and crawling and steering motions are only moderately altered when both counter-parts are manipulated at the same time. Moreover, the phenotypes caused by *flp-1* and *trp-4* are additive while *nlp-12* suppresses *trp-4* mutations.

DVA regulates body postures via promoting crawling motions. But when AVK is ablated, additional promotion of steering motions is revealed. Thus, DVA seems to support both crawling and steering motions, while AVK inhibits both motion types. The decrease of AVK neural activity during the period after the sensory stimulus should lead to a dis-inhibition of crawling by AVK /FLP-1. However, on average the crawling wave is strongly down-regulated, which should be caused by reduced promotion through DVA /NLP-12. On the contrary, the steering wave increases after stimulation, which should result from reduced suppression through AVK /FLP-1, while reduced promotion of steering through DVA /NLP-12 is rather not important. In the absence of both regulatory counterparts, animals are severely impaired in modulating crawling and steering motions and thus cannot properly switch between travel and local search after stimulation.

Calcium transients of AVK interneurons reflect the animal's locomotion speed. This can be interpreted as speed-modulating function of AVK neural activity, which is consistent with the observed speed reduction in animals with ablated AVK neurons. Possibly AVK neural activity serves to promote speed during travel and its activity decrease after stimulation might be involved in the observed slowing of the animals. However, AVK calcium transients were shifted relative to the animal's instantaneous speed with a delay of around 1.7 seconds. For comparison, recently measured correlations of calcium transients of AVB or RIB (GCaMP5K or GCaMP6F) activity with locomotion speed showed significantly shorter delay times of around 0.5 seconds (Kato et al., 2015). The delay of AVK calcium transients is less than one full undulation cycle (average ~2.5 seconds) and longer than expected if caused solely by GCaMP5K kinetics. GCaMP5K displayed an average time to peak of t_{peak} = 0.06 seconds in response to an action potential measured in mouse visual cortex (in vivo) (Chen et al., 2013). The slightly slower GCaMP3, with t_{peak} = 0.095 seconds (measured in acute cortical mouse brain slices) (Tian et al., 2009), had been evaluated in *C. elegans* dissected body wall muscle: GCaMP3 reached its peak 0.44 s after electrical muscle activation (Butler et al., 2014). Assuming similar calcium kinetics in AVK interneurons, neural activity of AVK lagged at least 1 second behind locomotion speed. This argues against an instructive function of AVK activity and rather favors a speed-monitoring

function of AVK.

The absence of AVK depression in response to an oxygen downshift in immobilized worms further supports the idea that AVK activity monitors locomotion speed. Nevertheless, movement could also exert a gating function for AVK interneurons: Sensory signals perceived via BAG oxygen sensory neurons, which need to be translated into locomotory adjustments, could possibly only affect AVK neural activity when animals are indeed performing locomotion. Other studies have reported altered neuronal dynamics in physically restrained worms (Ben Arous et al., 2010; Gordus et al., 2015). The lack of proprioceptive feedback that normally would occur during unrestrained movement or the strong mechanical stimulation caused by the physical confinement might influence neural activities.

Overall, the correlation observed between AVK activity and locomotion speed is moderate (r = 0.35). In comparison, calcium imaging recordings of AIY and RIB neurons yielded correlation coefficients of at least r = 0.5 (Li et al., 2014), or those of AVB and RIB were measured in another very recent study as r = 0.6 or 0.7, respectively (Kato et al., 2015). But AVK activity and speed display an interesting long-range correlation, not observed in AIY, AVB or RIB. It is possible that AVK activity might function to monitor locomotor activity over a longer timescale. Indeed the correlation is not modulated between non-stimulated and stimulated periods or between forward and reverse movement, further supporting the idea of a 'global' monitor function. The fact that AVK activity does not depend on the direction of movement appears quite unique, as so far neural activities of interneurons usually show strong differences associated with directional change (Kawano et al., 2011; Li et al., 2014). In fact a large portion of the worm nervous system shows direction-dependent activities (Kato et al., 2015).

FLP-1 is also expressed in other interneurons besides AVK, including AVA and AVE pre-motor interneurons and BAG-downstream partners RIG and AIY (Nelson, 1998). Rescuing flp-1-evoked phenotypes outside of AVK restored most of the analyzed behavioral parameters. Although FLP-1 expression appears to be relatively high in AVK compared to the other flp-1 expressing interneurons (observation made during this study, not shown), these other interneurons might also be involved in the suppression of steering and especially crawling wave power. It would be interesting to see whether ablation of these interneurons could recapitulate the high-curvature phenotype of flp-1 mutants.

DVA activity is essential for promotion of crawling waves, as deduced from the behavior of DVA-ablated worms. Consistently, increases in DVA activity during forward movement are associated with increased crawling wave power during non-stimulated and stimulated periods. But DVA calcium transients show no continuous instantaneous relationship with crawling motions. The simple reflection of dorso-ventral body-bending observed in tail-glued animals (Li et al., 2006) could not be confirmed in freely moving worms. Neither do DVA calcium fluctuations largely depend on TRP-4-dependent proprioception in moving worms. Although TRP-4 contributes to the regulation of crawling waves, it is not important for associated DVA calcium fluctuations during normal locomotion. The DVA calcium transients evoked by TRP-4-dependent proprioception might only be revealed in restricted animals, or could be overshadowed by other signals controlling DVA activity during free locomotion.

Indeed, DVA neural activity appears rather complex, encoding multiple features. Besides an association to crawling motions, I could show an association of higher DVA activity with phases of no movement (pausing) or reversals. Both types of events display higher steering power (in case of reversals this is possibly due to the frequently following deep turns), which suggests that DVA activity might reflect increases in steering motions, potentially via TRP-4-mediated proprioceptive mechano-sensation. While the association of voluntary spontaneous pause phases and high DVA calcium fluctuations, however, does not depend on TRP-4, the increased activity around reversals shows dependence on TRP-4. Maybe the previously studied tail-glued worms (Li et al., 2006) generated mainly waves moving from posterior to anterior along the body (= reverse movement), eliciting TRP-4-dependent activation of DVA.

The reversal and pausing events appeared more frequently after oxygen-sensory stimulation and dominated DVA's average activity during that period. Thus DVA calcium transients did not decrease as expected (when animals down-regulated traveling) but instead increased. After removing these events, average DVA activity did not significantly change, despite an expected decrease. But consistently, crawling wave power did not strongly decrease on average in the freely moving imaging experiments either; this was probably caused by differences in experimental conditions such as using agarose pads for the substrate (which are slightly more humid and softer than NGM assays plates).

DVA exhibits its function via NLP-12 neuropeptides: Worms mutant for *nlp-12* show similar (or even stronger) phenotypes as DVA-ablated worms and DVA has been shown to be the single source of NLP-12 secretion in several studies (Bhattacharya et al., 2014; Janssen et al., 2008; Hu et al., 2011). Still, increases in crawling wave power

associated with DVA activity peaks are not abolished in *nlp-12* mutants. Only in the absence of both NLP-12 and FLP-1 neuropeptides is this association severely hampered. Thus, DVA function should rely on both peptide types. A possible interpretation of this could be that FLP-1 is acting upstream of DVA and exhibiting some gating function onto DVA, which could then up-regulate the strength of crawling motions through an additional unidentified signaling path besides NLP-12 secretion. Eventually, this result points to a potential cross-talk between the two characterized counterparts DVA /NLP-12 and AVK /FLP-1 in the regulation of body postures.

Most analyses of this study focused on movement in forward direction, as it is the predominant direction of movement, and forward and reverse locomotion exhibit strong differences: The worm's body wave naturally inverses its direction and many inter- and motorneurons show opposite activities during forward and reverse locomotion (see section 2.3.5 or Kato et al., 2015). The direction of locomotion can be explained by the projection amplitudes of eigenworms 1-2 (Stephens et al., 2008), i.e. is not determined by steering motions. Yet, whether the power of crawling and steering motions are differentially regulated during reverse movement, needs to be determined. Initial observations indeed indicate increases of steering wave power during reverse movement.

4.3 Coordination of locomotion speed, crawling and steering motions

The sensory stimulation evokes changes in the locomotion speed, crawling and steering wave. These behavioral parameters are naturally not independent from each other. Locomotion speed is expected to be strongly controlled via bending frequency of the crawling wave, which is consistent with their strong correlation. Moreover, the reported speed phenotypes of mutants in this study (e.g. AVK-ablation or *nlp*-12 mutation) match the phenotypes observed in crawling frequency. Previously, other studies also reported related changes of locomotion speed and bending frequency in various mutant worm strains (Cronin et al., 2005; Yemini et al., 2013).

The body amplitude is thought to additionally promote locomotion speed, as the thrust generated by undulations is predicted to increase with wave amplitude (Gray, 1953). Here, I extracted differential regulation of crawling and steering wave power over the range of locomotion speed. Power in this study and wave amplitude in previous studies both are measures of the animal's body curvature. Crawling wave power indeed increases across the lower half of the speed range, suggesting promotion of speed, as predicted. The power reaches on average a maximum value at intermediate speed levels (~ 0.15 mm /s) and remains rather constant at higher speed levels. This

potentially constitutes an optimal wave amplitude, balancing increasing undulatory thrust against increasing path length, which would mean increased movement of the body perpendicular to the axis of progression.

The steering wave power is inversely related to speed. Elevated steering motions might interfere with fast locomotion due to their less regular nature, making efficient progression of the whole animal more difficult. Moreover strong steering waves often adopt C-like shapes with more similar curvature along the body that do not generate high thrust. These possibilities and /or crawling wave amplitudes beyond the optimum could explain why the high-curvature mutants (especially *flp-1* and *trp-4* mutants with wild type crawling frequency levels) analyzed in this study were not moving faster than wild type animals.

The counterbalance of steering motions against fast progression might not just be due to biomechanical reasons but constitute an active regulatory mechanism. In the wild, animals must tightly control their motions to successfully perform essential behaviors (Barnard, 2004; Domenici, 2000): While traveling fast along direct paths to cross larger distances, e.g. during migration between different habitats or escape runs from predators, animals generate stereotypic and highly controlled motion patterns. But when locally exploring and sampling the nearby environment, e.g. during foraging or inspection of a new habitat, it is beneficial to reduce movement pace and at the same time employ more flexible motion patterns. Similarly, fly larvae during odorant chemotaxis slow down or even stop to perform large head casts to actively sample the local environment and eventually perform turning maneuvers (Gomez-Marin et al., 2011).

Also animals as simple as *C. elegans* demonstrate this behavioral coordination. After one hour of food deprivation the worms are moving mainly to disperse (Gray et al., 2005; Hills, 2004) presumably in order to find potential food sources that are distant from their current location ('global' or 'straight-line search'). This current study shows that while animals move fast, they do not use strong steering motions but mainly strong crawling motions. This totally makes sense assuming the animals' goal is to cover large distances. When they detect a sensory stimulus indicative of a nearby food source, e.g. a reduction of ambient oxygen levels, they slow down to carefully explore the area ('local search'). Simply reducing speed and thus increasing the time scanning the nearby environment constitutes an exploration strategy (orthokinesis). But simultaneously up-regulating more flexible motions that produce frequent changes in heading direction (klinotaxis) and possibly active environmental sampling, enhances search efficiency; and therefore a larger part of the local area can be explored in the

same time. Thus, animals seem to purposefully coordinate two search strategies. The interneuron pair AVK, studied here, is a likely candidate actively coordinating locomotion speed (orthokinesis) and steering motions (klinotaxis) in the worm. It appears to monitor speed and transform this information into corresponding repression of steering motions. In the absence of AVK neurons, worms exhibit a slowing response to stimulation, but do not alter their steering motions. In mutant animals with functional AVK neurons, phenotypes of speed and steering motions appear more inter-related.

Bending amplitude and frequency have been shown to linearly correlate over a range of environments of different viscosities, evoking different waveforms and bending frequencies of undulations (Berri et al., 2009). In this current study the interneuron DVA and FLP-1 neuropeptides serve to promote or repress the power of crawling motions, respectively. But they do not regulate crawling frequency, implying distinct neural pathways in control of these two features. Thus, regulation of worm locomotion speed seems to rely on two separable mechanisms, crawling wave frequency and power /amplitude. They are usually co-regulated as illustrated by their positive relation. Consequently, worms need to adjust and coordinate crawling frequency, crawling power and steering power to build expedient complex motor behaviors. Crawling and steering power are regulated in a reciprocal manner. This either generates efficient crawling with low steering during traveling behavior, or increased steering during slow local search when crawling motions are only moderately needed. It is achieved via (at least partially) separate neural pathways, one encompassing AVK and FLP-1 and the other DVA and NLP-12. But exactly how crawling and steering motions are adjusted against each other remains to be elucidated. As AVK is repressive and DVA is activating, simple co-activation of the two neuron classes by upstream signals would simultaneously repress steering and promote crawling while inhibition of the neuron would yield the opposite. The two counterparts could also cross-regulate each other. The fact that the observed relations are very similar in non-stimulated and stimulated animals implies that there is a common coordination mechanism of crawling and steering, permanently controlling the worms' locomotion strategy.

One remaining question is how the switch between different locomotion strategies is initiated (sketched in Figure 4.3). Are all three parameters, crawling frequency, crawling power and steering power, separately adjusted at the same time? Or is one parameter actively affected by the signals transmitted through the oxygen-sensory BAG neurons and the other parameters follow?
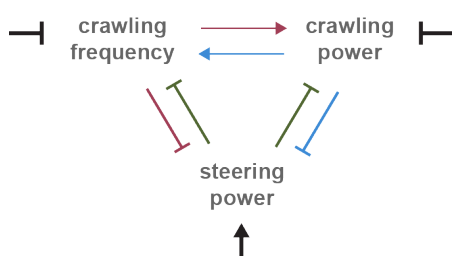
Figure 4.3. Possible inter-relations of crawling frequency, crawling and steering power
Crawling frequency might repress steering power. Crawling frequency and power might be co-regulated or one might positively affect the other. Strong steering might inhibit higher bending frequencies. Steering and crawling power might be reciprocally balanced against each other. The three parameters could instead be co-regulated by simultaneous upstream signals. (Interactions illustrate a temporal hierarchy and are not necessarily direct.)

As hypothesized in the model in Figure 4.2, a drop in speed (or possibly a drop of crawling frequency) might be causative for relieving steering motion suppression. The initial speed reduction might be achieved by simultaneous down-regulation of crawling wave frequency and power. But as the two parameters can be separately controlled, it is also possible that the power of crawling motions is initially restricted, evoking depression of frequency or vice versa. It is difficult to determine a potential temporal sequence when the distinct parameters are adjusted within a very short time interval and can therefore not be answered in this study.

4.4 Do neural correlates of crawling and steering waves exist?

The study raises the question of what the decomposition of worm locomotion means in terms of motor execution and its underlying neural control. Do neural correlates of crawling and steering waves exist in the *C. elegans* nervous system? The concept of controlling two parallel motion patterns is related to the assumption that nervous systems might control fixed patterns of relative levels of muscle activation to construct complex motor outputs, instead of independently regulating a huge amount of individual muscles or motor units (Lee, 1984; Sherrington, 1910). Such relative muscle activation patterns are often termed muscle synergies (Tresch and Jarc, 2009) (see section 2.2).

C. elegans might employ such a higher-level organization of motor behavior by combining crawling and steering motion patterns. Crawling and steering waves do not completely fulfill the criteria defining muscle synergies, as they do not represent invariant patterns, only the amplitudes of which are regulated. Yet, this is true for the underlying eigenworms (Stephens et al., 2011; 2008). These constitute fixed shapes whose projection amplitudes vary, but not the shapes themselves. Consistently, eigenworms do not change depending on oxygen-sensory stimulation and are shared between individual animals (this was confirmed by comparing eigenworms derived from individual worm tracks, but not shown in this thesis). It is appealing to imagine that worms might encode motor behaviors as various combinations of a few fixed shapes

(Stephens et al., 2008). Crawling and steering waves could be thought of as varying higher-level coordinating patterns of muscle activation.

The concept of two parallel motion patterns makes sense in terms of motor execution: Crawling wave generates thrust for progression and flexible steering motions are overlaid to determine the full posture outcome. As described in the previous sections 4.1 and 4.3, crawling and steering wave power display meaningful relations to locomotion speed and a reasonable inverse relation between each other. After oxygen-sensory stimulation the body wave drastically changes its pattern, from predominant sinusoidal shapes to more irregular body postures. But simply measuring the power of the body wave does not adequately capture these behavioral changes. However, the decomposition is necessary to quantitatively describe the simultaneous down-regulation of crawling and up-regulation of steering postures. Additional support for this concept comes from the following findings: (1) Cross-correlation analyses on selected segment angles, as discussed in section 4.1, delineate that both waves have a unique and meaningful pattern. (2) The interneurons AVK and DVA predominantly modulate only one of the two motion types. (3) AVK-ablated and *flp-1* mutant animals similarly exhibit high body curvature and increased body wave power, but distinct phenotypes of crawling and steering motions. This confirms an observation made during this study: Although the two worm strains show exaggerated body bends, their locomotion styles show qualitative differences. (4) Neural activities of AVK and DVA present preferential associations with decomposed waves: DVA calcium transient peaks associate with significant increases of crawling power, while the total body wave shows no associated regulation. When AVK activity drops during speed valleys, steering motions demonstrate more distinct up-regulation than the total body wave.

Nevertheless, one should not neglect that principle components analysis, used to decompose worm locomotion, is a linear decomposition method and yields components (eigenworms) that are orthogonal to each other, which inherently puts constraints onto the data treatment. If such patterns underlying the dynamics of body bends exist, they might display non-linear properties. Thus, this study's results should not necessarily be converted one-to-one to a mechanistic level. Nevertheless, the results support a promising concept of higher-level organization of motor control that is gaining increasing evidence from a variety of species (Bizzi and Cheung, 2013; Tresch and Jarc, 2009).

If worm undulations indeed rely on the regulation of separate crawling and steering motion patterns, what could be the neural structures and neural rhythms encoding the rhythmic motion patterns? Muscle synergies in vertebrates are believed to be encoded by spinal modules, which are units of interconnected interneurons in the spinal cord or brain stem. The motor cortex could combine and coordinate appropriate modules to regulate complex motor outputs (Bizzi and Cheung, 2013).

As described in section 2.2, mouse spinal interneurons are organized into separate modules that regulate limb alternation at different movement speeds (Bellardita and Kiehn, 2015; Talpalar et al., 2013). Limb alternation might be overlaid upon a more simple movement mode with synchronous limb motions, which drives locomotion when limb alternation is impaired. Motion patterns of *C. elegans* may be similarly encoded in units of interneurons, which form the largest group of neurons in the worm. First-layer interneurons receive direct information from sensory neurons and signal to second-layer interneurons (Gray et al., 2005; Tsalik and Hobert, 2003). Neurons from both layers are highly interconnected and relay signals to head motor neurons or pre-motor interneurons, finally controlling motor neurons. Head motor neurons can also function as interneurons via downstream connections to other inter- and motor neurons besides body wall muscle. Distinct subsets of second-layer interneurons and head motor neurons could potentially underlie crawling and steering motion patterns similar to spinal cord modules. First-layer interneurons could serve to regulate the combinations of neural modules.

As described in section 2.3.5, certain interneurons promote either forward runs (AVB, PVC, AIY, RIB, AIA) or reversals (AVA, AVD, AVE, AIB, AIZ) (Chalasani et al., 2007; Kawano et al., 2011; Li et al., 2014; Schrödel et al., 2013; Tsalik and Hobert, 2003; Wakabayashi et al., 2004), and could be interpreted as interneurons important for crawling motions. Interneurons like AIZ or AIY have also been reported to be essential for gradual directional changes during chemotaxis (Iino and Yoshida, 2009; Kocabas et al., 2012; Satoh et al., 2014), which suggests roles in the regulation of steering motions. However, it is not clear whether these neurons would serve to regulate the execution or the formation of motion patterns, i.e. whether they are upstream or part of encoding neural modules. AVK and DVA interneurons could rather fulfill modulatory functions onto these modules than constitute components of them. The neurons are necessary for proper regulation of the patterns but not essential for the pattern generation: Double ablated AVK-; DVA- animals are still able to crawl and perform steering maneuvers like deep omega turns.

Another possibility is that the two patterns could be encoded within different pools of motor neurons. Steering motions could be encoded by head motor neurons, which control head and neck muscles, while crawling motions could arise from motor neurons in the ventral nerve cord, which control neck and body muscles (VNC). Support for the idea of two separable motor modules in head and VNC that predominantly control steering or thrust generation, respectively, has been described in section 2.3.5 (p. 28-29). SMB, SMD, RME, RIV head motor neurons are potential candidate neurons regulating steering motions. When these neurons are manipulated, turning maneuvers, head amplitude and /or gradual directional changes are impaired (Gray et al., 2005; Kocabas et al., 2012; McIntire et al., 1993) (see section 2.3.5 for details). However, the execution of steering motions according to this current study involves the whole body; the signal would have to be relayed onto VNC motor neurons and body muscles. AVK is connected to head motor neurons (see section 4.5) and could affect steering motions initiated in the head, while DVA could signal directly to ventral cord motor neurons and control body motions important for crawling.

In vertebrates, spinal cord interneurons engage in neural circuits to form central pattern generators (CPGs), which generate rhythms and patterns essential for limb movements (Grillner and Jessell, 2009). In the *C. elegans* nervous system, neurons or circuits generating rhythmic activities for rhythmic undulatory locomotion are to date inconclusively identified. While the neural circuitry in the worm's head is suggestive of containing a CPG (Cohen and Sanders, 2014), motor neurons along the VNC, which innervate body wall muscles, are also considered a potential source for the undulatory rhythm: They display oscillatory activities (Faumont et al., 2011; Kawano et al., 2011) and their circuits show a distributed and recurrently connected architecture that theoretically could produce endogenous rhythmic patterns (Haspel and O'donovan, 2011). As worms have at least 8 distinct classes of ventral cord motor neurons (VA, DA, VB, DB, VD, DD, AS, VC), different patterns could theoretically be encoded by different subsets. As A-type (VA, DA) or B-type (VB, DB) neurons are considered to be especially important for reverse or forward movement, respectively (Chalfie et al., 1985; Kawano et al., 2011), these could preferentially control crawling motions. Other motor neuron classes (VD, DD, AS, VC), the roles of which in locomotion are less understood, could predominantly affect steering motions. GABAergic signaling from the inhibitory D-type neurons (VD, DD) for example is not necessary for forward crawling movement, but involved in promoting the body wave amplitude (McIntire et al., 1993). Acute interference with the activity of either VD or DD motor neurons can evoke biased strong body bends and thereby omega turns. Ablation of either VD or DD neurons

results in a dorsally or ventrally biased course during forward movement, respectively (Donnelly et al., 2013). Studying mutant worms lacking functional GABA synthesis or D-type motor neurons should reveal whether GABAergic signaling preferentially affects the amplitude of the steering wave and whether it is essential for postural adjustments after sensory stimulation. Moreover, imaging ventral cord motor neurons in freely moving worms and analyzing their activity patterns in association with crawling and steering motions could help discovering whether the distinct motion types are transmitted via distinct motor neurons classes. As discussed in the next section, ventral cord motor neurons are likely targets of NLP-12 and FLP-1 neuropeptides, which could be secreted along the entire length of the ventral cord due to the structure of both the AVK and DVA neural processes. The peptides could act as modulating factors upon the motion pattern encoding circuits.

Yet, the underlying neural structures might not be organized in such a modular manner. The encoding circuits might be overlapping and consist of inter- and motor neurons, as it is the case for the CPG circuits that underlie two different feeding motor patterns of lobsters and crabs (Marder and Bucher, 2007) (see section 2.1 for details). Two distinct main rhythms, which can occur in parallel, are generated by distinct sub-circuits, which are highly interconnected with each other and even share certain neurons (Weimann et al., 1991). Modulation via a range of classical neurotransmitters, biogenic amines and neuropeptides can alter circuit dynamics or even circuit configurations. The same neural structures can therefore produce a range of different output motor patterns. As the *C. elegans* nervous system comprises of highly interconnected inter- and motor neurons, a more complex system of overlapping and interconnected sub-circuits could potentially underlie crawling and steering motion patterns. The neuropeptides FLP-1 and NLP-12 could provide modulatory inputs to reconfigure circuit dynamics and /or circuit composition. Resulting modifications of neural rhythms would yield changes in motor output, i.e. adjustments of crawling and steering motion patterns. As each of the two characterized regulatory parts, DVA /NLP-12 and AVK /FLP-1, affects both crawling and steering waves, such complex overlapping structures seem more likely to underlie crawling and steering motion patterns than discrete inter- or motor neuron modules.

An important note is that superposition of two motion types should not happen at the final step, in terms of adding two muscle contraction forces together. Opposing forces of crawling and steering waves at the muscle level would be a waste of energy. Integration should happen at a higher level.

Last but not least, one cannot exclude the possibility that the decomposition into crawling and steering waves is only a theoretical concept without discrete neural correlates. These results could also arise from biomechanical constraints caused by the worm's anatomy or its interactions with the environment. Likewise the existence of neural correlates of muscle synergies is still debated (Kutch and Valero-Cuevas, 2012).

4.5 Potential up- and downstream structures of AVK and DVA involved in the control of locomotion strategies

The AVK interneuron class receives input from sensory, inter- and motor neurons. Notably there are strong synaptic inputs from the head motor /interneuron class RMF and several gap junctions from the head motor /interneuron class SMB (White et al., 1986). These neurons might relay information about bending strength and /or frequency to AVK and could explain the reflection of locomotion speed in AVK's activity. For RMF no specific function has been assigned so far, but AVK appears as its main output: 14 of its 23 determined chemical synapses are with AVK. The 7 electrical synapses between AVK and SMB seem important for the control of body posture, as SMB ablation has been shown to lead to increased head bend amplitude and body curvature (Gray et al., 2005), resembling the AVK-ablation phenotype of this current study. However, it is not clear whether SMB constitutes an input or output to AVK, as the direction of signal transmission through the electrical synapses is not known. Neural activities of SMB neurons that cause head muscle activation could possibly be transferred to AVK via gap junctions. AVK neural activity would then reflect SMB activity and indirectly head bending activity*.*

AVK activity could also be modulated via signals from PDE mechano-sensory neurons, which have many (21) chemical synapses onto AVK and thus should be major inputs. Besides mechanically sensing bacterial lawns (Sawin et al., 2000) and harsh touch (Li et al., 2011), the dopaminergic PDE neurons with processes along the entire body length are proposed to become stimulated during worm movement and secrete dopamine to maintain a steady speed (Omura et al., 2012). Interestingly, FLP-1 neuropeptides have already been suggested to be involved in dopamine-dependent modulation of *C. elegans* locomotion behavior in a swimming-induced paralysis paradigm (Wani et al., 2012).

Instead of indirect information about bending from other neurons, AVK could also monitor speed itself via proprioception. One theoretical possibility is that AVK could sense bending directly via stretch-sensitive molecules, as originally suggested for DVA

(Li et al., 2006). But no mechano-sensitive TRP or DEG/ENaC molecules are known to be expressed in AVK so far.

If AVK is rather signaling the transmission of the oxygen-sensory stimulus into behavioral responses, it could receive inhibitory inputs indirectly (via RIG interneurons) from BAG oxygen-sensory neurons, which are activated after oxygen level decreases. However, as discussed in section 4.2, AVK is rather monitoring locomotory activity. Additionally, speed reductions during constant 21% oxygen (without BAG activation) were also associated with drops of AVK activity.

The DVA interneuron receives most of its synaptic input from mechano-sensory neurons, mainly dopaminergic PDE neurons as well as some others (PLM, FLP, PHC) (White et al., 1986). A stimulatory effect of dopamine on the release of NLP-12 neuropeptides from DVA has previously been shown (Bhattacharya et al., 2014). Thus, dopaminergic PDE neurons could transfer signals about the locomotory activity onto DVA. As previously discussed, the TRP-4-dependent proprioception within DVA seems to be less important for DVA's activity, although it is involved in the release of NLP-12 and the regulation of crawling wave power. AVK also exhibits one synaptic connection onto DVA. Altogether, PDE neurons could transfer information through activation of both AVK and DVA into simultaneous inhibition of steering and promotion of crawling wave power. Through this pathway sensory stimuli other than oxygen could perhaps affect crawling and steering motions as well. As relations between speed and crawling or steering wave power persist in non-stimulated animals, their coordination is not oxygen-specific but a general mechanism.

To modulate locomotion, AVK and DVA signal to inter- and /or motor neurons. The neurons for example have connections to the important pre-motor interneurons AVE, AVB and AVA, and to ventral cord motor neurons. Both neuron classes are also connected to SMB class neurons, which have a role in restricting high-amplitude body waves (Gray et al., 2005). AVK activity could be transmitted to SMB via gap junctions and indirectly reduce bending strength, although it is not clear how cholinergic SMB motor neurons (Duerr et al., 2008; Rand and Nonet, 1997) generate suppression of bending. Stimulating either ventral or dorsal SMB neurons changes the worm's heading direction (Kocabas et al., 2012), which additionally suggests SMB neurons as targets of AVK to regulate steering motions. AVK is also pre-synaptic to four other head motor neuron classes and could therefore influence steering motions initiated in the head via several downstream partners. AVK might transmit its signals only partially

via FLP-1 peptides, and otherwise rely on its rich set of gap junction proteins and its central position in the worm's gap junction network (Altun et al., 2009; Varshney et al., 2011).

Both neuron classes, AVK and DVA, have long neural processes in the ventral nerve cord spanning the length of the worm body. The FLP-1 and NLP-12 peptides could potentially extra-synaptically reach all VNC motor neurons, as their cell bodies are inside the VNC. While DVA might mainly employ NLP-12 for signaling, DVA ablation and *nlp-12* mutant animals display discrepancies in their phenotypes. NLP-12 peptides are proposed to act on cholinergic motor neurons to potentiate transmission at the neuromuscular junction via CKR-2 receptors (Hu et al., 2011; Janssen et al., 2008). As *ckr-2* mutants behave like wild type and not like *nlp-12* mutant animals in this current study, there must be different or additional receptors mediating NLP-12 effects on crawling motions. Nevertheless, it seems likely that NLP-12 promotes crawling motions via increasing cholinergic signaling at the neuro-muscular junctions. Another recent study has proposed a role for NLP-12 in increasing the duration of synaptic currents at these synapses by enhancing acetylcholine release from cholinergic motor neurons (Bhattacharya et al., 2014).

Although their receptors are not known, FLP-1 peptides have been implicated in the suppression of the locomotor circuit by modulating GABAergic signaling at the neuromuscular junctions (Stawicki et al., 2013). This is consistent with the Aldicarb-resistant phenotype (a pharmacological measure of NMJ signaling) of *flp-1* mutant worms (Sieburth et al., 2005), which suggests a suppression of inhibitory or promotion of excitatory signaling. Thus NLP-12 could promote bending strength by stimulating cholinergic B- and / or A-type motor neurons and FLP-1 could suppress bending strength via stimulating inhibitory D-type motor neurons. While DVA is the only known source of NLP-12, FLP-1 is also expressed in AVA and AVE pre-motor interneurons, and the BAG-downstream interneurons RIG and AIY (Nelson, 1998). These neurons might in addition to AVK secrete FLP-1 to regulated steering and crawling motions. Interestingly, AIY neurons are known to be important for steering in chemotaxis (Kocabas et al., 2012; Satoh et al., 2014).

4.6 Body coordination within crawling and steering motion patterns

How different body parts are coordinated to form crawling or steering waves was not a major focus of this study. Nevertheless, it became clear from the cross-correlation results, that regular crawling wave patterns are formed by tight coordination of different body parts. Steering wave patterns are generated by more flexible relative positions of

different body parts that show a certain degree of correlation. Interestingly, the highest correlations of head segment angles with mid-body or posterior body segment angles do not include any delay time between the different body parts. This is true for both crawling and steering waves and when cross-correlations are performed on data only during forward movement.

A recent study proposes that (artificially imposed) body bends are propagated posteriorly via stretch-sensation through (anteriorly directed) neural processes of the B-type motor neurons. This means that the same motor neurons sense and stimulate muscle contraction (Wen et al., 2012). During movement a full undulation cycle takes about 2.5 seconds. If any change in wave pattern during forward movement was solely initiated in the head and propagated from head to tail only via sequential proprioception of bending, peak correlations between different body parts should display a delay recapitulating the propagation time. The absence of a delay time for crawling and steering waves implies simultaneous adjustment of different body parts and argues against purely sequential proprioceptive wave propagation.

The concept of sensory feedback governing the generation of sinusoidal waveforms is a strongly considered model, as no feed-forward pattern generator is yet identified in *C. elegans* and such models have yielded good approximations for worm locomotion (Boyle et al., 2012; Bryden and Cohen, 2008). These models however, deal only with the generation of constant forward movement wave patterns and do not incorporate wave pattern modulations that occur during slowing or steering. This current study suggests that changes of wave patterns are simultaneously initiated at three points along the body. In between these points proprioceptive signals might propagate the crawling and steering wave patterns: The cross-correlation profiles between head angle and all 24 segment angles do indeed display delays, which can go up to 0.6 s for crawling waves and up to 1s for steering waves, i.e. fractions of the duration of a full undulation cycle. Overall, this supports the notion that steering motions are not solely generated via head motions but through coordinated parallel adjustments along head and body.

4.7 Functional implementation of motion pattern coordination in the control of locomotion strategies

Many studies that examine different strategies of locomotion rely on the identification and quantification of discrete events such as forward runs and reorienting reversals and /or turns (Bhattacharya et al., 2014; Gomez-Marin et al., 2011; Gray et al., 2005; Wakabayashi et al., 2004). Such analyses are based on the concept that animals

control these strategies by regulating the switches between exclusive motor programs, e.g. when to switch runs off or turns on. The current study is based on a different concept, namely that animals continuously adjust the contributions of different parallel motion types; this means that animals constantly regulate how much to turn. Different locomotion strategies like travel and stimulus-induced local search behaviors of food-deprived animals are established through balancing crawling and steering motions. While promotion of crawling motions supports traveling, increases in steering motions support local search (Figure 4.4).

Figure 4.4. Travel and local search strategies are determined through the balance of crawling and steering wave contributions.

The distribution of steering wave power against locomotion speed does not reveal separated 'behavioral states'. A gradually decreasing oxygen ramp evokes gradual changes of steering wave power. This means that from travel to local search worms pass through 'intermediate states' and do not abruptly switch between the two strategies. Thus, the off-food locomotion behaviors of food-deprived worms classified here as travel and local search should rather be extremes along one continuous locomotion mode. The modulation of the motion patterns, which is partially achieved via FLP-1 and NLP-12 neuropeptides, fine-tunes the locomotion strategy. In the absence of both neuropeptides, animals are severely impaired in modulating crawling and steering motions and therefore cannot really change between travel and local search after stimulation.

This defect seems to also affect their chemotaxis performance: Current experiments ongoing in our laboratory (results not shown in this thesis) reveal that *flp-1; nlp-12* double mutant worms are hampered in executing weathervaning chemotaxis in oxygen gradients. As most movements in a gradient result in a change of oxygen levels, animals might continuously adjust their crawling and steering motions. The mutant animals are not able to properly fine-tune the strength of their steering motions in response to step-like or gradual oxygen changes. Thus, they also fail to properly adjust steering motions depending on their orientation in the gradient. This means that they cannot steer (perform klinotaxis) towards preferred intermediate oxygen levels as efficiently as wild type animals.

The travel behavior described in this study matches the previously described dispersal behavior initiated after roughly 15-30 minutes away from food, which consists of fast and straight movement with low number of reorienting events (reversals, omega turns) (Gray et al., 2005; Hills, 2004; Wakabayashi et al., 2004). The dispersal behavior follows after an area-restricted search, which occurs immediately after removal from food: Animals perform frequent reorientation maneuvers, similar to the oxygen-induced local search described here. In fact, under both conditions, it is likely that animals are locally searching for food, either due to recent experience of food or due to a sensory stimulus indicative of a nearby food source.

Extrapolating the results from oxygen-induced local search, it seems likely that worms gradually transit from area-restricted search after removal from food to dispersal via gradually down-regulating steering motions and up-regulating crawling motions. This would match the reported gradual decline in omega turn frequency (Gray et al., 2005). NLP-12 and FLP-1 neuropeptides are likely to be involved in the behavioral changes. Consistently, a recent study proposes a dopamine-evoked increase of NLP-12 secretion through DVA immediately after removal from food (Bhattacharya et al., 2014). The authors further show that NLP-12 is important for high body amplitude after the switch from on- to off-food conditions, which fits NLP-12's function in promoting body curvature under food-deprived conditions as observed in this current study. NLP-12-mediated stimulation of crawling waves could explain the increase of speed associated with the removal from food (Gray et al., 2005). The reported requirement of NLP-12 to increase reorientation events and thereby support local search behavior (Bhattacharya et al., 2014), indicates that NLP-12 also promotes steering motions after the sudden withdrawal of food. How NLP-12 and FLP-1 secretion change as time away from food increases is not known so far.

On food, *C. elegans* moves generally much slower than off food and spontaneously switches between two behavioral states: dwelling and roaming behaviors. Dwelling consists of especially slow movement with increased directional change (including many reversals) leading to higher average track curvature and an overall low displacement. Roaming describes faster movement along straighter paths with few directional changes, which leads to lower average track curvature and greater displacement (Ben Arous et al., 2009; Fujiwara et al., 2002). FLP-1 neuropeptides and TRP-4 mechano-sensation have also been shown to be important for suppressing high body curvature on food (Li et al., 2006; Nelson, 1998). NLP-12's potential effects on

body curvature on food have not been studied so far. Modulation via FLP-1 and TRP-4 /NLP-12, which characterizes the transition between travel and local search off food, might also determine the switch between dwelling and roaming on food.

Dwelling might arise through higher steering and lower crawling motions, while roaming could be generated by moderate up-regulation of crawling and suppression of steering. Yet, it is not clear whether the cause of high track curvature during dwelling is solely due to the directional changes associated with reversals or additionally due to increased steering /turning maneuvers (Gallagher et al., 2013). Regulation of changes between forward and reverse movement represents another important contribution to directional change and therefore to the determination of locomotion strategies. This has not been considered in this current study, but is another very important parameter defining locomotion strategies, like dwelling or klinokinesis chemotaxis (Pierce-Shimomura et al., 1999).

Roaming and dwelling could also be considered as extreme behaviors along the range of one continuous locomotion mode. Indeed, a recent study modeling *C. elegans* on-food behaviors, suggests that the observed behaviors appear not to be limited to discrete roaming and dwelling states, but intermediate states also occur (Gallagher et al., 2013). Modulation and balance of different motion types could also determine roaming, dwelling or less frequently occurring intermediate behaviors. In fact, another recent study supports the idea that neuromodulation is heavily employed to regulate the switch between the two opposite locomotion strategies (Flavell et al., 2013). The monoamine serotonin promotes dwelling behavior, while PDF neuropeptides support roaming behavior. In the absence of either modulator, animals are still able to perform the respective behavioral strategy, however, the behavior durations are reduced. Together these studies support a common principle in the design of various locomotion strategies: Neuromodulation is important to properly employ and balance motion patterns, however it is not required for their generation.

It would be very interesting to see, whether differential regulation of crawling and steering motion patterns could also account for the distinct movement kinetics of swimming motions, including increased bending frequency and wavelength (Fang-Yen et al., 2010; Pierce-Shimomura et al., 2008). Although originally thought to represent to distinct gaits, there is increasing evidence that crawling on dry surfaces and swimming in liquid are extremes of a single gait, defined by external forces (Berri et al., 2009; Lebois et al., 2012). Swimming postures resemble C-shapes (longer wavelength) and are similar to the shapes of up-regulated steering waves, while postures of crawling

animals are S-shapes (shorter wavelength) and similar to strong crawling wave shapes. Thus, modulation of crawling and steering waves in order to regulate the behavioral changes seen between crawling and swimming seems conceivable. In line with this, it has been reported that modulation via serotonin supports swimming, while dopamine promotes crawling (Vidal-Gadea et al., 2011). Further analyses decomposing body waves of worms swimming in liquid or moving on food should help reveal whether *C. elegans'* locomotion repertoire can be fully explained by modulation and balance of crawling and steering motions.

Overall, the results of this current study support the concept of higher-level organization of locomotion behaviors as superposition of motion patterns that generate either regular or flexible motions. This concept suggests that nervous systems might control complex behavioral outputs including diverse locomotion strategies by combining and coordinating simpler elementary motion patterns.

5 Experimental procedures

5.1 Worm population behavioral assays

(1) Assays

Behavioral studies of *C. elegans* populations were done as described previously (Zimmer et al., 2009) with some modifications: For each assay ~25 adult animals grown on OP50 seeded food plates (1 day post L4 larval stage) were transferred (via manual picking) without food onto a plane food-free nematode growth medium (NGM) agar surface in a 14 cm petri dish (NGM assay plate). Animals were starved for one hour on the NGM assay plate prior to examination. A 36 mm x 36 mm area was cut out of Whatman filter paper soaked in 20mM of repelling copper chloride to prevent animals from leaving the assay arena. A custom-made transparent plexiglass device with a flow arena of 39 mm x 39 mm x 0.7 mm was placed onto the assay arena and animals were exposed to a gas flow of 25 ml/ min containing 21% (v/ v) oxygen for six minutes, followed by a switch to 10% O_2 for six minutes (shift assays) or followed by a temporal ramp from 21% to 4% oxygen lasting three minutes (step size 0.094 %/ s). All gas mixtures were balanced with nitrogen. Gases were mixed with a static mixing element connected to mass flow controllers (Vögtlin Instruments) that were operated by custom written LabVIEW (National Instruments) software. The temporal oxygen shifts and ramp were confirmed by measuring oxygen concentrations in the device with an oxygen-sensitive fluorescent spot sensor (PreSens). We measured that oxygen shifts equilibrate the arena within 12 s. The oxygen ramps were found to be linear as expected. Recordings of freely behaving animals illuminated with 200 mm x 200 mm flat red LED lights were made at 10 fps on 4-5 megapixel CCD cameras (JAI) using Streampix software (Norpix). The pixel resolution was 0.0129mm/ pixel.

Representative worm images in Figure 3.1 and 3.28 were generated by cutting out a portion from video frames recorded at 21% oxygen.

(2) Tracking and analyses

Movies were analyzed with a customized version of the Parallel Worm Tracker, a MATLAB-based (MathWorks) image processing and tracking script described previously (Chalasani et al., 2007; Ramot et al., 2008; Zimmer et al., 2009). Briefly, worms were detected by gray level thresholding. Centroids were determined from ellipses fit onto the binary worm images. Worm trajectories were generated by connecting nearby centroid coordinates in adjacent frames and each trajectory coordinate was assigned with recorded binary images, centroid coordinates and shape parameters; the resulting data-structures are termed here worm tracks. Trajectories are

terminated when worms collide with each other or with the boundaries of the arena. Each worm track therefore represents a fragment of each worm's complete behavior during the recording time. Worm tracks with a length of less than 200 (20s duration) frames were discarded. Each worm is typically represented by multiple worm tracks of varying length. The resulting trajectories were smoothed and used to calculate instantaneous translational speed of the worm's centroid, which is measured along the axis of progression. Periods of backward locomotion were detected based on changes in angular velocity and building on the fact that animals were moving most of the time in forward direction, which was confirmed also for all mutants used in this study. Reversals frequency was calculated in 10-second bins. Reversals usually were excluded (data set to NaN) from the population behavioral assay analyses to obtain forward locomotion only. Time periods during which the animals were within 80pixels (=1.0mm) distance to the Whatman paper were also excluded. Deep, so-called omega turns were detected based on characteristic changes in object eccentricity and angular speed, and their frequency was calculated in 10-second bins.

All further analyses on data from worm population assays were performed using custom MATLAB scripts.

Track curvature was determined from smoothed centroid trajectories for every frame as absolute change of heading angle between adjacent frames. Therefore the heading angle per frame i was extracted as the four-quadrant inverse tangent of the x/y-coordinates resulting from the differences between the centroid x/y-positions in frame $i-5$ and frame $i+5$ (1-second intervals). The result (change of heading angle per frame) was divided by the mean crossed distance per frame during the same 1-second interval. This yielded change of heading angle over distance. Data during which animals were barely moving (speed < 0.03 mm /s) had to be excluded as centroid "wobbling" due to tracking issues at very low speeds caused falsely high curvature levels. Artificially high values (>31 rad /mm = 99.5 percentile) were removed. Data during reverse movement were excluded.

Displacement was calculated in bins (Figure 3.3 E) or running windows (Figure 3.14, 3.15 and 3.28) of 30 seconds. Distance of the centroid positions between start and end point for every bin were determined for each worm track (Figure 3.3 E). For chosen time intervals (as indicated in the figure legends) the displacement was determined as distance of the centroid position between 15 seconds before and 15 seconds after every respective frame (=running window, Figure 3.14, 3.15 and 3.28). The intervals pre or post the oxygen downshift were chosen in a way that the running window around

the last or first frame, respectively, did not include time points beyond the shift. For displacement, movement in reverse direction was not excluded.

5.2 Skeletonization and segment angle analyses

All analyses were performed using custom MATLAB scripts.

After thresholding, the binary worm images were processed (by dilation, erosion, edge-smoothing, bridging unconnected points, hole-filling) before they were eventually skeletonized (including trimming for optimization) to obtain one-dimensional splines tracing the midline of the worms from head to posterior end. The pointy tail tips were omitted due to thresholding issues. Artificially short skeleton splines (< 45 worm skeleton points) were excluded and the data of these frames set to NaN. The extracted splines were smoothed and divided into 25 equally spaced body segments by cubic spline interpolation. Images of worms forming coil-like postures as occurring e.g. during deep omega turns could not be skeletonized. Thus, curvature data during these highly curved postures were not fully covered. Yet, time points during those turning events around the moments of head-body touching could be skeletonized.

Head positions were determined based on direction of movement and taking into account when the animals moved backward. Then skeletons were ordered accordingly. Head-tail flips were further prevented due to the fact that the head position could only change by limited distance in-between adjacent frames (0.1 second). Thus both skeleton end points were compared to the head position of the previous frame and the end point with smaller distance was usually (except for identified deep omega turns, when head and tail position were very close) taken as the new head position. 24 inter-segment angles were calculated between the adjacent segments from head (segment angle #1) to tail (segment angle #24). Segment angle time series were added to the worm tracks structures. They were termed body wave. Previous studies had used at least 48 (up to 100) segments (Brown et al., 2012; Stephens et al., 2008; Yemini et al., 2013). Here, 24 segment angles recapitulated similar eigenworm shapes. The advantage of choosing (in comparison to these studies) lower resolution was being able to record from multiple animals simultaneously and to acquire data with the parallel worm tracker described above. This approach provides higher sample power required for trial averaging and statistics when assaying behavioral responses that naturally exhibit high single trial animal-to-animal variability.

5.3 Eigenworm-based decomposition and analysis of crawling and steering wave

All analyses were performed using custom MATLAB scripts.

For calculation of eigenworms (except for Figure 3.5), all wild type N2 segment angle time series (containing forward and backward locomotion) were concatenated. For Figure 3.5, only wild type segment angle time series that were spanning defined 60-second intervals directly pre or post the oxygen shift, respectively, were concatenated. Then eigenworms (EW) (and eigenvalues for Figure 3.5) were derived by standard principal components analysis (PCA) on the concatenated angles. Variance contribution per eigenworm (Figure 3.5) was calculated as the relative fraction each eigenvalue contributed to the sum of all eigenvalues.

Segment angle time series of all individual worm tracks from all strains were projected onto these wild type-derived eigenworms. The time series mean of each angle was subtracted from each angle. Then, crawling wave or steering wave was generated by firstly calculating the cross-product of the 24 segment angles with a matrix made up by eigenworms 1-2 or remaining eigenworms 3-24, respectively. This step yielded a description of the body wave in terms of 2 or 22 projection amplitudes along the respective eigenworms. Secondly, the cross product of the result with the respective eigenworm matrix was calculated and the previously subtracted mean was added. This step retrieved the description in terms of 24 segment angles.

$$crawling\ wave$$
$$= (\ ([EW1:EW2]\ x\ [angles - mean(time\ series)])\ x\ [EW1:EW2]) + mean(time\ series)\ )$$

$$steering\ wave$$
$$= (\ ([EW3:EW24]\ x\ [angles - mean(time\ series)])\ x\ [EW3:EW24])$$
$$+ mean(time\ series)\ )$$

This procedure decomposed the body wave on a frame-by-frame basis into crawling wave and steering wave. As PCA is a linear decomposition method, the total body wave is the sum of every corresponding crawling and steering wave:

$$body\ wave = crawling\ wave + steering\ wave$$

Mutant eigenworms in Figure 3.16 were derived from all concatenated segment angle time series (containing forward and backward locomotion) from the respective worm strain and performing principle components analysis in the same way as for wild type data. The projections of mutant-derived body waves onto the corresponding mutant

eigenworms and generation of crawling and steering wave shown in Figure 3.21 were done with the same equations mentioned above.

Cross-correlation functions in Figure 3.7 A-F were calculated from selected segment angles (as indicated) of all wild type N2 crawling or steering wave time series. This method was robust with respect to the varying lengths (at least 20s) of worm tracks. For Figure 3.7 G-H all wild type time series from a 3-minute interval (at 21% oxygen) were pooled before performing cross-correlation of head segment angle #2 against all 24 segment angles. Periods of reverse movement were excluded. The absolute value of the peak correlation and the respective absolute lag time for each combination were plotted.

I calculated the **power** of each wave by summing the absolutes of all 24 segment angles per time point. An inter-segment angle of zero should ideally result from zero bending strength. The more the angle deviates from zero, the higher the bending strength. In order to capture the whole-worm absolute bending strength exerted by the respective wave, the sum of all segment angle absolutes thus represents a good measure.

Bending frequency of crawling waves was derived by determining maxima from the time series of mid-body segment angle (#11) absolutes (smoothed by 3 frames) with a peak-finding algorithm. Peak-to-peak frequencies were calculated from these data and continuous time series of bending frequency were obtained by cubic interpolation. Thus, crawling frequency was measured as bends in ventral or dorsal direction per time (one bend = half an undulation cycle). In order to account only for forward locomotion, periods of backward locomotion were excluded from frequency population data.

Worm shapes in Figure 3.6D were reconstructed from total body wave, crawling wave or steering wave by calculating synthetic worm silhouettes at chosen points of worm track time series. From the respective 24 segment curvature angles and a list of 25 fixed end-to-end segment lengths, the position of 26 2D points along the central line of the worm body from head to tail were calculated. Combining these 26 central line points with a fixed list of 26 cross sectional widths from head to tail, a filled 2D polygonal model of the worm consisting of 50 quadrilaterals and 2 triangles, one for the head-most segment and one for the tail-most segment, was created. The overall orientation for these reconstructed worms was determined at each time point by matching the centroid-to-nose-tip vector to a corresponding vector extracted from real

movies. The filled 2D polygonal model was then rendered into an image using a standard triangle-filling pixel scan-line algorithm.

5.4 Distributions, trial-averaging, quantifications and statistics of behavior data

All analyses were performed using custom MATLAB scripts.

For **trial-averaging**, means and standard errors of the mean (SEM) of behavioral time courses were calculated from population averages, which were determined on a frame-by-frame basis from all worm tracks of all experiments available in each frame. These averages were finally binned (by 10 frames = 1-second intervals) for display reasons. Averages of reversal and omega turn frequency or displacement rate were determined in 10-seconds or 30-seconds bins, respectively, per worm track and averaged after binning.

Distributions of behavioral features were derived as follows. For 1D relative distributions of power of the respective waves (Figures 3.10, 3.11, 3.19), all data from the indicated time interval were pooled per experiment and normalized histograms with 0.1rad bin size were derived and then averaged over all experiments. For analyzing two behavioral features against each other, all worm tracks (binned by 5 frames = 0.5 seconds) within the respective indicated time interval of all experiments were pooled. For density maps displaying 2D distributions (Figures 3.4, 3.12), normalized 2D histograms were derived with the following bin sizes. Figure 3.4: locomotion speed (bin size =0.001 mm /s) against track curvature (bin size = 0.02 rad /mm). Speed range was cut off due to track curvature artifacts below 0.03mm/s (see calculation of track curvature) or data sparseness above 0.3 mm/s, respectively. Very high track curvature values (>7 rad /mm) were not shown due to data sparseness. Figure 3.12: locomotion speed (bin size =0.001 mm /s) against steering wave power (0.025 rad). For sorting one behavioral feature Y over another feature X (Figures 3.4, 3.8, 3.9), feature X was divided into bins of equal length (speed 0.01 mm /s, track curvature 0.4 rad /mm, crawling wave power 0.1 rad). Medians and inter-quartile ranges of feature Y from worm track data within each bin of X were calculated and plotted over the medians of bins from X. Very high values of speed (>0.3 mm /s), track curvature (> 5 rad /mm) and power (>5 rad) were not shown due to data sparseness. Linear correlation coefficients (Figure 3.9 E) were calculated from all pooled data points via a MATLAB standard function.

Example trajectories in Figure 3.8D were chosen during the 10% oxygen phase. Positions and steering wave power were binned by 5 frames (0.5 s) and the trajectories' start points were aligned.

For **quantifications and statistics** we chose to account for experiment-to-experiment variability. Therefore the population means for each individual experiment were calculated from respective indicated time intervals. For changes after oxygen downshift, the means of two equally sized intervals were subtracted per experiment. Relative changes of locomotion speed were determined by normalizing the change over the level obtained during the interval pre downshift for each experiment.

Boxplots displayed median, interquartile range and 5-95 percentile whiskers of these calculated means from all experiments. Sample sizes were the number of experiments. All data of mutants were compared to the wild type N2 dataset, or between selected strains as indicated, by one-way-ANOVA with Sidak correction. For comparing neuropeptide mutants (and cell ablated lines) to wild type, all acquired data per strain were used, because the *flp-1* mutant displayed relatively increased behavioral variability between different sets of experiments. In order to get the best picture of its phenotype all data were taken into account. For analyzing neuropeptide rescues strains, only mutant and wild type experiments performed in parallel were used. For analyzing strains mutant for *trp-4* (Figure 3.28, 3.29), only the data from wild type and other mutant strains acquired in parallel were used.

For comparing intervals pre and post the shift per strain (Figure 3.3), paired t-tests were performed.

5.5 Simultaneous imaging of neuronal calcium and behavior

Calcium imaging recordings of freely moving animals were performed with an automatic re-centering system developed and described in (Faumont et al., 2011). Adult (1 day post L4 larval stage) single worms expressing both mCherry and GCaMP5K (or GFP) in the neuron of interest were placed on food-free nematode growth medium (NGM) agarose pads and sealed in a custom-built airtight chamber with inlet and outlet connectors for gas delivery. Animals were starved for 1 hour prior the imaging experiment on a food-free normal NGM plate. For agarose pads, freshly mixed NGM containing agarose instead of agar (for higher transparency and less background signals) was melted and poured into a ring (2.45 mm thick and 50 mm diameter). Enclosing with two glass plates ensured hardening into a plane surface. This was essential for avoiding out-of-focus movement. An indentation around the pad borders was made by pressing a smaller ring (38 mm diameter) onto the hardened agarose. 20mM of repelling copper chloride was pipetted into the indentation to restrict the worm to the central part of the pad. The prepared pad was then transferred into the chamber, which was sealed airtight and covered with a glass slide (0.55 mm thickness)

holding a distance of 0.7 mm from the pad surface. The sealed chamber was integrated into a motorized stage connected to a controller (MS-2000-PhotoTrack, Applied Scientific Instrumentation). 21% (v/ v) oxygen, balanced with nitrogen, was applied for 4 minutes with a gas flow of 50ml/ min to the chamber, followed by a switch to 10% O_2 for 4 minutes. Gases were mixed with a static mixing element connected to mass flow controllers (Vögtlin Instruments).

Image acquisition was carried out using an inverted compound microscope (Zeiss Axio Observer.Z1) which employed two Charge-Coupled Device (CCD) cameras (Evolve 512, Photometrics). A CoolLED pE-2 excitation system, equipped with an ET-EGFP/mCherry excitation filter set (59022x, Chroma) and a dichroic (59022bs, Chroma), generated dual wavelength excitation (470 nm and 585 nm). Images were acquired with 33 ms exposure time (30 fps) via a long-distance 63x objective (Zeiss LD Plan-Neofluar 63x, 0.75 NA), which was operated by Visiview software (Visitron Systems GmbH, Germany). A quadrant photomultiplier tube (Hamamatsu) detected high-wavelength mCherry light emitted from the mCherry fluorophore expressed in the neuron (and serving thus as a tracking target), split by a dichroic mirror (620spxr, Chroma). The signal was used to re-center the motorized stage via the controller. The remaining emitted light from the neuronal expressed fluorophores was split via a DualCam DC2 cube (565 lpxr, Photometrics) and sent to the two CCD cameras, recording mCherry emission (641 /75 nm, Brightline) or GCaMP emission (520 /35 nm, Brightline), respectively. Prior to that a neutral density filter decreased mCherry emission to 50% in order to avoid signal saturation.

Simultaneous recording of animal behavior was achieved by infrared LED illumination (780 nm) and image acquisition by an IR-sensitive CCD camera (Manta Prosilica GigE, Applied Vision Technologies) at 4x magnification (resolution = 1.6 mm /pixel) and with 100ms exposure time (10 fps) operated by StreamPix software (Norpix).

5.6 Image processing of freely moving calcium-imaging data

Fluorescence intensity values for GCaMP and mCherry were extracted with a custom-made MATLAB tracking script. After manually determining a threshold intensity value for the mCherry channel-derived images capturing the neuron of interest during all recording frames, the sum of pixels from a connected region of at least 50-pixel size above threshold was measured in each frame. For the GCaMP channel-derived images, I measured the sum of pixels from the region matching the mCherry thresholded area for each frame. Both datasets were background-corrected by subtracting the average background pixel value (obtained from the respective first

image frame capturing unspecific tissue signal) multiplied by the number of pixels thresholded in that frame.

The ratio R of GCaMP5K/ mCherry was calculated per frame to correct for artificial GCaMP fluorescence changes due to motion artifacts or out-of-focus movements of the cell body. Very strong out-of-focus movements were automatically excluded, as the there was no connected region >50 pixels above threshold in that frames. I further corrected for stronger out-of-focus movements, which could not be fully corrected not through the ratio calculation, by determining strong drops or rises in mCherry fluorescence (relative to its gross local mean) and occasionally unreasonably large relative drops in GCaMP fluorescence values (relative to its gross local mean). Normalized ratio dR /R (%) was calculated as the difference of R extracted from each frame to the mean R of the total recording and divided by mean R [(R-mean(R)) /mean(R)]. Further signal artifacts were determined and excluded by determining extremely high ratio values (absolute and relative to a finer local mean) and drops (relative) of the normalized ratio, which had been carefully evaluated for each cell. All excluded data were set to NaN. GFP control data were extracted and processed exactly the same way as GCaMP data.

5.7 Segmentation, skeletonization and extraction of segment angles from infrared recordings

Worm skeleton extraction from infrared videos was performed as described in (Yemini et al., 2013), save for a few minor modifications. The custom-made MATLAB codes were modified and shared by the authors. Videos were down-sampled to 520x519 pixels. A fixed binarizing threshold value (an 8-bit grayscale value of 127) was manually chosen for every recording to separate worm from background. The thresholded worm was dilated by usually 3 pixels to smooth any imperfections of the thresholded image and then eroded by usually 8 pixels to achieve an accurate representation of the worm (Dilation and erosion parameters were adjusted when necessary). The original algorithm was too stringent in rejecting poorly segmented worm shapes. Therefore, all thresholds for worm-shape rejection were relaxed by 80% without compromising the effectiveness of this step. Head/tail classification was a matter of determining which end of the worm was more central, which depended on the position of the mCherry fluorophore tracking target in the worm. Therefore, within video chunks of contiguous worm segmentations, individual skeletons were oriented relative to each other as previously described, then head and tail were determined by taking the mean distance of both worm ends from the video center. Thereafter, all steps to

skeletonize the worms were as formerly described (Yemini et al., 2013), save for a reduction in skeleton size to 26 worm points. As a final step, videos overlaying the skeleton onto the actual original worm image were produced so that the fidelity of skeletonization could be evaluated directly, ensuring error-free behavioral data.

5.8 Analyses of simultaneous calcium imaging and behavioral data

Locomotion speed and direction

Precise positions of the motorized tracking stage and thus the tracked neural target were recorded for every frame (30 fps) via the VisiView software and extracted using a MetaMorph (Universal Imaging) custom-made script. Obtained stage positions were further analyzed with MATLAB-based custom-made processing scripts. Locomotion speed was calculated with a step-size of 30 frames (=1 second), i.e. speed of frame i was the distance between positions of frame i-15 and frame i+15 divided by the passed time. Artificially high values (>0.6 mm /s), when the tracking of the cell was lost, were excluded. Angular velocity was calculated with a step-size of 5 frames after extracting heading angles from changes in x/y-coordinates during 30-frame bins of smoothed (30 frames) trajectories. Then, periods of backward locomotion were detected based on local maxima of absolute angular velocity, local maxima and minima of the speed derivative and minima of speed, and by considering a maximum length of reversals per strain.

All further analyses were performed using custom MATLAB scripts.

Inter-segment angles

The splines encoded by the extracted 26 worm skeleton points were smoothed per frame and 24 inter-segment angles were calculated for each frame. When no or artificial (too long or short due to image segmentation issues) skeletons were retrieved, segment angles were set to NaN. Small gaps (<0.5 seconds) in segment angle time series were filled by cubic interpolation and angles were smoothed over time (15 frames = 1.5 seconds). In order to match calcium imaging and segment angle data, the segment angle time series were cubically interpolated from their original acquisition rate of 10Hz to the 30Hz-frame rate of the calcium imaging recordings.

Single traces of normalized ratio or wave power were smoothed by 15 frames (0.5 seconds) prior **trial-averaging**. Then means and SEMs from time courses of normalized ratio dR /R or behavior parameters were calculated from of all recordings and averages were binned (by 30 frames = 1-second intervals) for display reasons.

Fraction of animals reversing or pausing were calculated and binned, into 10-seconds or 5-seconds bins, respectively. If indicated, only data during certain locomotion phases e.g. forward movement were used to calculate averages by setting ratio or behavior data e.g. during reversals (and pause phases) to NaN. For statistics, means of normalized ratio or behavior parameters were calculated per worm from respective indicated time intervals. The means pre and post the oxygen downshift were compared with paired tests (paired t-test or Wilcoxon matched-pairs signed rank test) as indicated to evaluate the changes. For comparing these oxygen-evoked changes between different worm strains (GCaMP- vs. GFP-expressing worms) or conditions (freely moving vs. immobilized) the means of the two equally sized intervals (pre and post) were subtracted per worm and evaluated by one-way-ANOVA with Dunnett's correction or Mann Whitney test, as indicated.

Single worm traces for illustration were smoothed by 5 frames and every 10th point was plotted for display reasons.

Eigenworms of all pooled segment angle time series (containing forward and backward locomotion) of wild type GCaMP-expressing N2 worms from calcium-imaging experiments were concatenated (separately for AVK and DVA imaging lines). Then eigenworms (EW) were derived by standard principal components analysis (PCA) on the concatenated angles using MATLAB. The individual segment angle time series of all recorded worms from all strains were projected onto these wild type-derived (respective AVK- or DVA-GCaMP) eigenworms exactly the same way, as done for the population behavioral assays (section 5.3) to retrieve **crawling and steering waves**. Further the power of each wave was calculated accordingly by summing the absolutes of all 24 segment angles per time point.

Bending **frequency** and **amplitude** of all waves were calculated by detecting local maxima of the angles' absolutes with a peak-finding algorithm, and determining thereof the peak-to-peak frequencies and absolute peak amplitudes. Continuous time series of bending frequency and absolute amplitude envelope were obtained by cubic interpolation.

For further analyses all data time series were smoothed by usually 5 frames, or 15 frames when peak detection was involved. **Cross correlation function** in Figure 3.23 B was calculated per worm from whole recording time series and mean and SEM was derived from all worms.

For analyzing the **relation of the neural activity ratio to selected behavior features**, data points per worm were binned by 15 frames (= 0.5 seconds) and then pooled from all recordings. If indicated, only data within respective time intervals or data during specific locomotion phases were taken into account. The ratio data were then sorted over bins of equal length of the behavior feature (speed 0.01 mm /s, wave power 0.2 rad). Medians and inter-quartile ranges of the ratio data within each bin were calculated and plotted over the medians of the behavior bins. Very high values of speed (>0.35 mm /s) and power (>4 or 6 rad) were not shown due to data sparseness. **Linear correlation coefficients** were calculated per worm with a MATLAB standard function and compared between intervals, locomotion phases or between strains, using paired or unpaired t-test or one-way-ANOVA with Sidak's correction as indicated. Boxplots displayed median, interquartile range and 5-95 percentile whiskers of these calculated means from all worms. Before analyzing the relation of AVK ratio and locomotion speed, ratio data were shifted relative to speed data by a lag time of 1.67 seconds, which had been derived from the peak r value of the cross-correlation.

For **event-triggered averages**, a peak-detection algorithm was used to determine speed valleys during forward locomotion (excluding reversals) for AVK recordings or DVA ratio peaks during forward moving phases (from identified 'moving phases' and excluding reversals). Further reversal start time points derived from the stage position were used. The respective traces of speed, normalized ratio dR /R or wave power plus surrounding 6-10 seconds on either side were aligned to these events and means and SEMs per frame of all events were calculated and plotted. Wilcoxon matched-pairs signed rank tests compared means calculated per event of short intervals (length as indicated) pre and post the event. The means of the pre and post intervals were subtracted per event and the changes were evaluated by Mann-Whitney test or Kruskal-Wallis test with Dunn's correction (as indicated) comparing different waves or different strains (mutant or GFP-expressing worms to wild type /GCaMP-expressing worms).

Moving and pausing phases were classified as phases of at least 2-second duration above or below a speed threshold of 0.05 mm/s, tolerating gaps of maximum 1 seconds. Means of normalized dR /R or wave power during moving or pausing phases, from worms that were pausing at least 60s of the recording time (with interruptions), were compared via Wilcoxon matched-pairs signed rank tests.

5.9 Imaging of neural activity in microfluidic chip

Microfluidic two-layer PDMS devices were constructed as previously described (Chronis et al., 2007; Zimmer et al., 2009). The worm channel was connected to a reservoir containing S-Basal buffer. All components were connected with Tygon tubing (0.02 in ID, 0.06 in OD; Norton) or polyethylene tubing (0.066 in ID, 0.095 in OD; Intramedic) using 23G Luer-stub adapters (Intramedic). 21% (v/ v) oxygen, balanced with nitrogen, was applied with a gas flow of 50ml/ min for 4 minutes, followed by a switch to 10% O_2 for 4 minutes. Gases were mixed with a static mixing element connected to mass flow controllers (Vögtlin Instruments). After 1-hour starvation on a food-free NGM plate, single adult (1 day post L4 larval stage) worms expressing both mCherry and GCaMP5K in AVK were loaded into the worm channel. Therefore, they were transferred into a drop of S-Basal on the NGM plate, sucked up into Tygon tubing by applying a short vacuum to the worm outlet and finally positioned inside the channel. Image acquisition was carried out using an epifluorescence microscope and a CoolLED pE-2 excitation system, equipped with an ET-EGFP/mCherry excitation filter set (59022x, Chroma) and a dichroic (59022bs, Chroma) providing dual wavelength excitation light (470nm and 585nm) and an Optosplit II (Cairns) image splitter (filter set used: 580 nm beam splitter and 520/35 nm and 641/75 nm bandpass emission filters). Split imaging data were acquired with an Andor iXon 397 EMCCD camera with 100 ms exposure time (10 fps), operated by MetaMorph software (Universal Imaging).

Fluorescence values were measured with a custom-made tracking script written in MetaMorph software. The region of bright mCherry signal was detected by thresholding and robustly tracked using the built-in track object function. Measurement regions for GCaMP signal as well as nearby regions for measuring background values were manually selected for the first image frame. Their positions were updated according to the frame-to-frame displacement of the mCherry-tracking region. Normalized ratio dR /R (%) was calculated in the same way as for the freely moving calcium-imaging data (5.6).

5.10 Worm culture and strains

Worms were maintained at 20˚C on plates of agar nematode growth medium (NGM) seeded with OP50 *Escherichia coli* bacteria as a food source (Brenner, 1974). Wild-type was *C. elegans* Bristol strain N2. Mutant strains used in this study were:

ZIM144, *flp-1(ok2811)IV,* 6x outcrossed to N2

ZIM550, *nlp-12(ok335)I,* 6x outcrossed to N2

ZIM551, *flp-1(ok2811)IV;nlp-12(ok335)I,* derived from crossing ZIM144 with ZIM550

TQ296, *trp-4(sy695)I,* 8x outcrossed to N2

ZIM421, *flp-1(ok2811 IV; trp-4(sy695)I,* derived from crossing ZIM144 with TQ296

ZIM715, *nlp-12(ok335)IV; trp-4(sy695 I,* derived from crossing ZIM550 with TQ296

LSC32, *ckr-2(tm3082);* 8x outcrossed to N2.

I verified the *flp-1(ok2811)* allele by cDNA sequencing: it deletes the last two bases of exon 1 and the entire exon 2 of the *flp-1* coding region resulting in an artificial exon 1 (made up of remaining unspliced parts of intron 2) with a predicted premature stop codon; further this causes a frame shift starting from exon 3 including the whole sequence section encoding the actual neuropeptides. Therefore *flp-1(ok2811)* is a prospective null allele. As opposed to the previously described alleles *flp-1(yn2)* and *flp-1(yn4)*, *flp-1(ok2811)* does not affect the nearby *daf-10* coding region.

Mutant worm strains were received from Caenorhabditis Genetics Center (CGC), Liliane Schoofs Laboratory and Chris Li Laboratory.

Transgenic animals were generated by injecting plasmid mixes into gonads of young adult hermaphrodites and generating heritable extra-chromosomal arrays. All injection mixes were prepared to yield 100ng/ul by adding empty pSM plasmids when necessary. *Punc-122::gfp*, *Punc-122::dsRed* (expressed in so-called coelomocytes) or *Pmyo-3::mCherry* (expressed in body wall muscles) were used as co-injection markers, as indicated. Same G-CaMP transgenes were used by crossing into the different genetic backgrounds.

Strain	Genotype	Description
ZIM466	*lite-1(xu-7)X; mzmEx300[Pflp-1(AVK)::GCaMP5K; Pflp-1(AVK)::mCherry]*	AVK imaging line (wt)
ZIM622	*lite-1(xu-7)X; flp-1(ok2811)IV; nlp-12(ok335)I; mzmEx300[Pflp-1(AVK)::GCaMP5K; Pflp-1(AVK)::mCherry]*	AVK imaging line (flp-1; nlp-12)
ZIM626	*lite-1(xu-7)X; mzmEx407[Pflp-1(AVK)::GFP; Pflp-1(AVK)::mCherry]*	AVK gfp control imaging line
ZIM563	*lite-1(xu-7)X; mzmEx365[Pnlp12::GCaMP5K; Pnlp-12::wCherry]*	DVA imaging line (wt)
ZIM623	*lite-1(xu-7)X; flp-1(ok2811)IV; mzmEx365[Pnlp12::GCaMP5K; Pnlp-12::wCherry]*	DVA imaging line (flp-1)
ZIM644	*lite-1(xu-7)X; nlp-12(ok335)I; mzmEx365[Pnlp12::GCaMP5K; Pnlp-12::wCherry]*	DVA imaging line (nlp-12)
ZIM643	*lite-1(xu-7)X; flp-1(ok2811)IV; nlp-12(ok335)I; mzmEx365[Pnlp12::GCaMP5K; Pnlp-12::wCherry]*	DVA imaging line (flp-1;nlp-12)
ZIM917	*lite-1(xu-7)X; trp-4(sy695)I; mzmEx365[Pnlp12::GCaMP5K; Pnlp-12::wCherry]*	DVA imaging line (trp-4)
TRL144	*lite-1(xu-7)X; lite-1(xu-7)X; Pnlp12::GFP; Pnlp-12::wCherry]*	DVA gfp control imaging line

ZIM319	*flp-1(ok2811)IV; mzmEx142[Pflp-1(AVK)::flp-1::SL2::gfp; Pmyo-3::mCherry]*	*flp-1* rescue in AVK
ZIM318	*flp-1(ok2811)IV; mzmEx32 [Pflp-1::flp-1::SL2::gfp; Pmyo-3::mCherry]*	*flp-1* rescue under full endogenous promoter
ZIM804	*flp-1(ok2811)IV; mzmEx482 [Pflp-18::flp-1::SL2::gfp; Popt-3::flp-1::SL2::gfp; Punc-122::dsRed]*	*flp-1* rescue in interneurons incl. AVA, RIG, AIY, AVE
ZIM915	*flp-1(ok2811)IV; mzmEx142[Pflp-1(AVK)::flp-1::SL2::gfp; Pmyo-3::mCherry]; mzmEx482[Pflp-18::flp-1::SL2::gfp; Popt-3::flp-1::SL2::gfp; Punc-122::dsRed]*	*flp-1* rescue in interneurons incl. AVK and AVA, RIG, AIY, AVE
ZIM837	*nlp-12(ok335)I; mzmEx505[Pnlp12::nlp12::SL2::gfp; Pflp-17::gfp]*	*nlp-12* rescue with endogenous promoter
ZIM367	*mzmEx249[Pflp-1(AVK)::egl-1::SL2::gfp Pflp-1::mCherry; Punc-122::dsRed]*	AVK-
ZIM625	*mzmEx406[Pnlp-12::p12::SL2::mCherry; Pnlp-12::p17::SL2::mCherry; Pnlp-12::mCherry; Punc-122::gfp]*	DVA-
ZIM627	*mzmEx249[Pflp-1(AVK)::egl1::SL2::gfp; Pflp-1::mCherry; Punc-122::dsRed]; mzmEx406[Pnlp-12::p12::SL2::mCherry; Pnlp-12::p17::SL2::mCherry; Pnlp-12::mCherry; Punc-122::gfp]*	AVK-; DVA-
CX11697	*kyIs536[Pflp-17::p17::SL2::gfp elt-2::gfp]; kyIs538[Pglb-5::p12::SL2::gfp; elt-2::mCherry]*	BAG- (from Bargmann laboratory)

Pro-apoptotic genes used for cellular ablation were *egl-1* (Conradt and Horvitz, 1998), or *p12* and *p17,* which encode domains from split caspase 3 (*ced-3*) (Chelur and Chalfie, 2007).

GCaMP5k in mzmEx365 is codon-optimized for *C. elegans* (GenScript).

wCherry is codon-optimized mCherry and was kindly donated by Zhen laboratory

5.11 Molecular biology and promoters for tissue specific expression

PCR-amplified DNA fragments of interest flanked by restriction sites were cloned into pSM vectors. Promoters were inserted via *FseI* and *AscI* sites while coding regions were usually inserted via *NheI* and *Acc651* sites.

Pflp-1(AVK): a 505bp fragment of *flp-1* promoter which extends from position −513 to −9 relative to the *flp-1* start codon, expressed in AVK only (Altun-Gultekin et al., 2001; Nelson, 1998).

Pflp-1: a 5831bp fragment directly upstream of the ATG start codon of *flp-1* gene, reported to be expressed in head neurons AVK, AVE, AVA, RIG, RMG, AIY, AIA, M5 (Nelson, 1998).

Pnlp-12: 383bp fragment, directly upstream of the ATG start codon of the *nlp-12* gene, reported to be solely expressed in DVA (Hu et al., 2011) and kindly provided by the Kaplan laboratory.

Pflp-18 4158bp fragment of 4151bp upstream and 7bp downstream of the ATG start codon of *flp-18* gene.

Popt-3 2464bp fragment directly upstream of the ATG start codon of *opt-3* gene.

flp-1 genomic region including the whole coding regions: 1414bp fragment beginning at start codon and including 127bp of 3'UTR.

nlp-12 genomic region including the whole coding regions: 437bp fragment from start to stop codon.

6 References

Akerboom, J., Chen, T.-W., Wardill, T.J., Tian, L., Marvin, J.S., Mutlu, S., Calderon, N.C., Esposti, F., Borghuis, B.G., Sun, X.R., et al. (2012). Optimization of a GCaMP Calcium Indicator for Neural Activity Imaging. J Neurosci *32*, 13819–13840.

Albrecht, D.R., and Bargmann, C.I. (2011). High-content behavioral analysis of Caenorhabditis elegans in precise spatiotemporal chemical environments. Nat Meth *8*, 599–605.

Allen, A.T., Maher, K.N., Wani, K.A., Betts, K.E., and Chase, D.L. (2011). Coexpressed D1- and D2-Like Dopamine Receptors Antagonistically Modulate Acetylcholine Release in Caenorhabditis elegans. Genetics *188*, 579–590.

Altun, Z.F., and Hall, D.H. (2011). Nervous system, general description. In *WormAtlas*.

Altun, Z.F., Chen, B., Wang, Z.-W., and Hall, D.H. (2009). High resolution map of Caenorhabditis elegansgap junction proteins. Dev. Dyn. *238*, 1936–1950.

Altun-Gultekin, Z., Andachi, Y., Tsalik, E.L., Pilgrim, D., Kohara, Y., and Hobert, O. (2001). A regulatory cascade of three homeobox genes, ceh-10, ttx-3 and ceh-23, controls cell fate specification of a defined interneuron class in C. elegans. Development *128*, 1951–1969.

Angstadt, J., and Stretton, A.W. (1989). Slow active potentials in ventral inhibitory motor neurons of the nematode Ascaris. J Comp Physiol A *166*, 165–177.

Bargmann, C.I. (1998). Neurobiology of the Caenorhabditis elegans Genome. Science *282*, 2028–2033.

Bargmann, C. (2006). Chemosensation in C. elegans. WormBook 1–29.

Barnard, C. J. (2004) Animal behaviour: mechanism, development, function and evolution. Harlow: Pearson Education.

Beets, I., Janssen, T., Meelkop, E., Temmerman, L., Suetens, N., Rademakers, S., Jansen, G., and Schoofs, L. (2012). Vasopressin/Oxytocin-Related Signaling Regulates Gustatory Associative Learning in C. elegans. Science *338*, 543–545.

Bell, W.J. (1991). Searching behaviour: the behavioural ecology of finding resources (Chapman and Hall).

Ben Arous, J., Laffont, S., and Chatenay, D. (2009). Molecular and Sensory Basis of a Food Related Two-State Behavior in C. elegans. PLoS ONE *4*, e7584.

Ben Arous, J., Tanizawa, Y., Rabinowitch, I., Chatenay, D., and Schafer, W.R. (2010). Automated imaging of neuronal activity in freely behaving Caenorhabditis elegans. J Neurosci Methods *187*, 229–234.

Berg, H.C., and Brown, D.A. (1972). Chemotaxis in Escherichia coli analysed by three-dimensional tracking. Nature *239*, 500–504.

Berri, S., Boyle, J.H., Tassieri, M., Hope, I.A., and Cohen, N. (2009). Forward locomotion of the nematode C. elegans is achieved through modulation of a single gait. Hfsp J *3*, 186–193.

Bhattacharya, R., Touroutine, D., Barbagallo, B., Climer, J., Lambert, C.M., Clark, C.M., Alkema, M.J., and Francis, M.M. (2014). A conserved dopamine-cholecystokinin signaling pathway shapes context-dependent Caenorhabditis elegans behavior. PLoS Genet *10*, e1004584.

Bizzi, E., and Cheung, V.C.K. (2013). The neural origin of muscle synergies. Front Comput Neurosci *7*, 51.

Boyle, J.H., Berri, S., and Cohen, N. (2012). Gait Modulation in C. elegans: An Integrated Neuromechanical Model. Front Comput Neurosci *6*, 10.

Bretscher, A.J., Busch, K.E., and de Bono, M. (2008). A carbon dioxide avoidance behavior is integrated with responses to ambient oxygen and food in Caenorhabditis elegans. Proceedings of the National Academy of Sciences *105*, 8044–8049.

Brockie, P.J., Mellem, J.E., Hills, T., Madsen, D.M., and Maricq, A.V. (2001). The C. elegans glutamate receptor subunit NMR-1 is required for slow NMDA-activated currents that regulate reversal frequency during locomotion. Neuron *31*, 617–630.

Brown, A.E.X., Yemini, E.I., Grundy, L.J., Jucikas, T., and Schafer, W.R. (2013). A dictionary of behavioral motifs reveals clusters of genes affecting Caenorhabditis elegans locomotion. Proceedings of the National Academy of Sciences *110*, 791–796.

Bryden, J., and Cohen, N. (2008). Neural control of Caenorhabditis elegans forward locomotion: the role of sensory feedback. Biol Cybern *98*, 339–351.

Butler, V.J., Branicky, R., Yemini, E., Liewald, J.F., Gottschalk, A., Kerr, R.A., Chklovskii, D.B., and Schafer, W.R. (2014). A consistent muscle activation strategy underlies crawling and swimming in Caenorhabditis elegans. Journal of the Royal Society Interface *12*, 20140963–20140963.

C. elegans Sequencing Consortium (1998). Genome sequence of the nematode C. elegans: a platform for investigating biology. Science *282*, 2012–2018.

Chalasani, S.H., Chronis, N., Tsunozaki, M., Gray, J.M., Ramot, D., Goodman, M.B., and Bargmann, C.I. (2007). Dissecting a circuit for olfactory behaviour in Caenorhabditis elegans. Nature *450*, 63–70.

Chalfie, M., Sulston, J.E., White, J.G., Southgate, E., Thomson, J.N., and Brenner, S. (1985). The neural circuit for touch sensitivity in Caenorhabditis elegans. J Neurosci *5*, 956–964.

Chase, D.L., Pepper, J.S., and Koelle, M.R. (2004). Mechanism of extrasynaptic dopamine signaling in Caenorhabditis elegans. Nat Neurosci *7*, 1096.

Chelur, D.S., and Chalfie, M. (2007). Targeted cell killing by reconstituted caspases. Proc Natl Acad Sci USA *104*, 2283–2288.

Chen, B.L., Hall, D.H., and Chklovskii, D.B. (2006). Wiring optimization can relate neuronal structure and function. Proc Natl Acad Sci USA *103*, 4723–4728.

Chen, T.-W., Wardill, T.J., Sun, Y., Pulver, S.R., Renninger, S.L., Baohan, A., Schreiter, E.R., Kerr, R.A., Orger, M.B., Jayaraman, V., et al. (2013). Ultrasensitive fluorescent proteins for imaging neuronal activity. Nature *499*, 295–300.

Cheung, B.H.H., Cohen, M., Rogers, C., Albayram, O., and de Bono, M. (2005). Experience-dependent modulation of C. elegans behavior by ambient oxygen. Curr Biol *15*, 905–917.

Chronis, N., Zimmer, M., and Bargmann, C.I. (2007). Microfluidics for in vivo imaging of neuronal and behavioral activity in Caenorhabditis elegans. Nat Meth *4*, 727–731.

Cohen, E., Yemini, E., Schafer, W., Feitelson, D.G., and Treinin, M. (2012). Locomotion analysis identifies roles of mechanosensory neurons in governing locomotion dynamics of C. elegans. Journal of Experimental Biology *215*, 3639–3648.

Cohen, N., and Sanders, T. (2014). Nematode locomotion: dissecting the neuronal–environmental loop. Curr Opin Neurobiol *25*, 99–106.

Conradt, B., and Horvitz, H.R. (1998). The C. elegans protein EGL-1 is required for programmed cell death and interacts with the Bcl-2-like protein CED-9. Cell *93*, 519–529.

Cronin, C.J., Mendel, J.E., Mukhtar, S., Kim, Y.-M., Stirbl, R.C., Bruck, J., and Sternberg, P.W. (2005). An automated system for measuring parameters of nematode sinusoidal movement. BMC Genet. *6*, 5.

Davis, R.E., and Stretton, A.O. (1989). Passive membrane properties of motorneurons and their role in long-distance signaling in the nematode Ascaris. J Neurosci *9*, 403–414.

de Bono, M., and Villu Maricq, A. (2005). NEURONAL SUBSTRATES OF COMPLEX BEHAVIORS IN C. ELEGANS. Annu Rev Neurosci *28*, 451–501.

Domenici, P. (2000). Biomechanics in animal behavior. London: Taylor & Francis.

Donnelly, J.L., Clark, C.M., Leifer, A.M., Pirri, J.K., Haburcak, M., Francis, M.M., Samuel, A.D.T., and Alkema, M.J. (2013). Monoaminergic Orchestration of Motor Programs in a Complex C. elegans Behavior. PLoS Biol *11*, e1001529.

Duerr, J.S., Han, H.-P., Fields, S.D., and Rand, J.B. (2008). Identification of major classes of cholinergic neurons in the nematode Caenorhabditis elegans. J Comp Neurol *506*, 398–408.

Esmaeili, B., Ross, J.M., Neades, C., Miller, D.M., and Ahringer, J. (2002). The C. elegans even-skipped homologue, vab-7, specifies DB motoneurone identity and axon trajectory. Development *129*, 853–862.

Fang-Yen, C., Wyart, M., Xie, J., Kawai, R., Kodger, T., Chen, S., Wen, Q., and Samuel, A.D.T. (2010). Biomechanical analysis of gait adaptation in the nematode Caenorhabditis elegans. Proceedings of the National Academy of Sciences *107*, 20323–20328.

Faumont, S., Lindsay, T., and Lockery, S. (2012). Neuronal microcircuits for decision making in C. elegans. Curr Opin Neurobiol *22*, 580–591.

Faumont, S., Rondeau, G., Thiele, T.R., Lawton, K.J., Mccormick, K.E., Sottile, M., Griesbeck, O., Heckscher, E.S., Roberts, W.M., Doe, C.Q., et al. (2011). An Image-Free Opto-Mechanical System for Creating Virtual Environments and Imaging Neuronal Activity in Freely Moving Caenorhabditis elegans. PLoS ONE *6*, e24666.

Flavell, S.W., Pokala, N., Macosko, E.Z., Albrecht, D.R., Larsch, J., and Bargmann, C.I. (2013). Serotonin and the Neuropeptide PDF Initiate and Extend Opposing Behavioral States in C. elegans. Cell 1–13.

Fraenkel, G.S., and Gunn, D.L. (1961). The Orientation of Animals: Kineses, Taxes and Compass Reactions (Dover Publ.).

Francis, M.M., Evans, S.P., Jensen, M., Madsen, D.M., Mancuso, J., Norman, K.R., and Maricq, A.V. (2005). The Ror Receptor Tyrosine Kinase CAM-1 Is Required for ACR-16-Mediated Synaptic Transmission at the C. elegans Neuromuscular Junction. Neuron *46*, 581–594.

Frézal, L., and Félix, M.-A. (2015). C. elegans outside the Petri dish. Elife *4*.

Friesen, W.O., and Cang, J. (2001). Sensory and central mechanisms control intersegmental coordination. Curr Opin Neurobiol *11*, 678–683.

Fryxell, J.M., Hazell, M., Börger, L., Dalziel, B.D., Haydon, D.T., Morales, J.M., McIntosh, T., and Rosatte, R.C. (2008). Multiple movement modes by large herbivores at multiple spatiotemporal scales. Proceedings of the National Academy of Sciences *105*, 19114–19119.

Fujiwara, M., Sengupta, P., and McIntire, S.L. (2002). Regulation of body size and behavioral state of C. elegans by sensory perception and the EGL-4 cGMP-dependent protein kinase. Neuron *36*, 1091–1102.

Gallagher, T., Bjorness, T., Greene, R., You, Y.-J., and Avery, L. (2013). The Geometry of Locomotive Behavioral States in C. elegans. PLoS ONE *8*, e59865.

Gao, S., and Zhen, M. (2011). Action potentials drive body wall muscle contractions in Caenorhabditis elegans. Proceedings of the National Academy of Sciences *108*, 2557–2562.

Gomez-Marin, A., and Louis, M. (2014). Multilevel control of run orientation in Drosophila larval chemotaxis. Front. Behav. Neurosci. *8*, 38.

Gomez-Marin, A., Stephens, G.J., and Louis, M. (2011). ncomms1455. Nat Comms *2*, 441–10.

Goodman, M.B., Hall, D.H., Avery, L., and Lockery, S.R. (1998). Active currents regulate sensitivity and dynamic range in C. elegans neurons. Neuron *20*, 763–772.

Gordus, A., Pokala, N., Levy, S., Flavell, S.W., and Bargmann, C.I. (2015). Feedback from Network States Generates Variability in a Probabilistic Olfactory Circuit. Cell 1–15.

Gray, J. (1953). Undulatory propulsion. Quarterly Journal of Microscopical Science *3*, 551–578.

Gray, J., and Lissmann, H.W. (1964). The locomotion of nematodes. J Exp Biol *41*, 135–154.

Gray, J.M., Hill, J.J., and Bargmann, C.I. (2005). A circuit for navigation in Caenorhabditis elegans. Proc Natl Acad Sci USA *102*, 3184–3191.

Gray, J.M., Karow, D.S., Lu, H., Chang, A.J., Chang, J.S., Ellis, R.E., Marletta, M.A., and Bargmann, C.I. (2004). Oxygen sensation and social feeding mediated by a C. elegans guanylate cyclase homologue. Nature *430*, 317–322.

Grillner, S., and Jessell, T.M. (2009). Measured motion: searching for simplicity in spinal locomotor networks. Curr Opin Neurobiol *19*, 572–586.

Harden-Jones F.R. (1955). Photokinesis in the ammocoete larva of the brook lamprey. J Exp Biol *32*, 492–503.

Hart, A.C., Sims, S., and Kaplan, J.M. (1995). Synaptic code for sensory modalities revealed by C. elegans GLR-1 glutamate receptor. Nature *378*, 82–85.

Hart, C.B., and Giszter, S.F. (2010). A Neural Basis for Motor Primitives in the Spinal Cord. J Neurosci *30*, 1322–1336.

Haspel, G., and O'donovan, M.J. (2011). A Perimotor Framework Reveals Functional Segmentation in the Motoneuronal Network Controlling Locomotion in Caenorhabditis elegans. J Neurosci *31*, 14611–14623.

Haspel, G., O'donovan, M.J., and Hart, A.C. (2010). Motoneurons Dedicated to Either Forward or Backward Locomotion in the Nematode Caenorhabditis elegans. Journal of Neuroscience *30*, 11151–11156.

Hedgecock, E.M., and Russell, R.L. (1975). Normal and mutant thermotaxis in the nematode Caenorhabditis elegans. Proc Natl Acad Sci USA *72*, 4061–4065.

Hendricks, M., Ha, H., Maffey, N., and Zhang, Y. (2012). Compartmentalized calcium dynamics in a C. elegans interneuron encode head movement. Nature 1–6.

Hills, T. (2004). Dopamine and Glutamate Control Area-Restricted Search Behavior in Caenorhabditis elegans. J Neurosci *24*, 1217–1225.

Hills, T.T. (2006). Animal foraging and the evolution of goal-directed cognition. Cogn Sci *30*, 3–41.

Hu, Z., Pym, E.C., Babu, K., Vashlishan Murray, A.B., and Kaplan, J.M. (2011). A Neuropeptide-Mediated Stretch Response Links Muscle Contraction to Changes in Neurotransmitter Release. Neuron *71*, 92–102.

Huang, K.-M., Cosman, P., and Schafer, W.R. (2008). Automated detection and analysis of foraging behavior in Caenorhabditis elegans. Automated Detection and Analysis of Foraging Behavior in Caenorhabditis Elegans *171*, 153–164.

Iino, Y., and Yoshida, K. (2009). Parallel Use of Two Behavioral Mechanisms for Chemotaxis in Caenorhabditis elegans. J Neurosci *29*, 5370–5380.

Izquierdo, E.J., and Lockery, S.R. (2010). Evolution and Analysis of Minimal Neural Circuits for Klinotaxis in Caenorhabditis elegans. J Neurosci *30*, 12908–12917.

Jander, R. (1975). Ecological Aspects of Spatial Orientation. Annu. Rev. Ecol. Syst. *6*, 171–188.

Janssen, T., Meelkop, E., Lindemans, M., Verstraelen, K., Husson, S.J., Temmerman, L., Nachman, R.J., and Schoofs, L. (2008). Discovery of a Cholecystokinin-Gastrin-Like Signaling System in Nematodes. Endocrinology *149*, 2826–2839.

Jing, J., Cropper, E.C., Hurwitz, I., and Weiss, K.R. (2004). The construction of movement with behavior-specific and behavior-independent modules. J Neurosci *24*, 6315–6325.

Kang, L., Gao, J., Schafer, W.R., Xie, Z., and Xu, X.Z.S. (2010). C. elegans TRP Family Protein TRP-4 Is a Pore-Forming Subunit of a Native Mechanotransduction Channel. Neuron *67*, 381–391.

Kaplan, J.M., and Horvitz, H.R. (1993). A dual mechanosensory and chemosensory neuron in Caenorhabditis elegans. Proc Natl Acad Sci USA *90*, 2227–2231.

Kato, S., Kaplan, H.S., Schrödel, T., Skora, S., Lindsay, T.H., Yemini, E., Lockery, S., and Zimmer, M. (2015). Global brain dynamics embed the motor command sequence of *Caenorhabditis elegans*. Cell *in press.*

Kawano, T., Po, M.D., Gao, S., Leung, G., Ryu, W.S., and Zhen, M. (2011). An Imbalancing Act: Gap Junctions Reduce the Backward Motor Circuit Activity to Bias C. elegans for Forward Locomotion. Neuron *72*, 572–586.

Khan, A.G., Sarangi, M., and Bhalla, U.S. (2012). Rats track odour trails accurately using a multi-layered strategy with near-optimal sampling. Nat Comms *3*, 703.

Kim, D., Park, S., Mahadevan, L., and Shin, J.H. (2011). The shallow turn of a worm. Journal of Experimental Biology *214*, 1554–1559.

Kocabas, A., Shen, C.-H., Guo, Z.V., and Ramanathan, S. (2012). Controlling interneuron activity in Caenorhabditis elegans to evoke chemotactic behaviour. Nature *490*, 273–277.

Kutch, J.J., and Valero-Cuevas, F.J. (2012). Challenges and New Approaches to Proving the Existence of Muscle Synergies of Neural Origin. PLoS Comput Biol *8*, e1002434.

Lahiri, S., Shen, K., Klein, M., Tang, A., Kane, E., Gershow, M., Garrity, P., and Samuel, A.D.T. (2011). Two Alternating Motor Programs Drive Navigation in Drosophila Larva. PLoS ONE *6*, e23180.

Lebois, F., Sauvage, P., Py, C., Cardoso, O., Ladoux, B., Hersen, P., and Di Meglio, J.-M. (2012). Locomotion Control of Caenorhabditis elegans through Confinement. Biophysical Journal *102*, 2791–2798.

Lee, W.A. (1984). Neuromotor synergies as a basis for coordinated intentional action. J Mot Behav *16*, 135–170.

Leifer, A.M., Fang-Yen, C., Gershow, M., Alkema, M.J., and Samuel, A.D.T. (2011). Optogenetic manipulation of neural activity in freely moving Caenorhabditis elegans. Nat Meth *8*, 147–152.

Li, C., Kim, K., and Nelson, L.S. (1999). FMRFamide-related neuropeptide gene family in Caenorhabditis elegans. Brain Res *848*, 26–34.

Li, W., Feng, Z., Sternberg, P.W., and Xu, X.Z.S. (2006). A C. elegans stretch receptor neuron revealed by a mechanosensitive TRP channel homologue. Nature *440*, 684–687.

Li, W., Kang, L., Piggott, B.J., Feng, Z., and Xu, X.Z.S. (2011). The neural circuits and sensory channels mediating harsh touch sensation in Caenorhabditis elegans. Nat Comms *2*, 315–319.

Li, Z., Liu, J., Zheng, M., and Xu, X.Z.S. (2014). Encoding of Both Analog- and Digital-like Behavioral Outputs by One C. elegans Interneuron. Cell *159*, 751–765.

Liewald, J.F., Brauner, M., Stephens, G.J., Bouhours, M., Schultheis, C., Zhen, M., and Gottschalk, A. (2008). Optogenetic analysis of synaptic function. Nat Meth *5*, 895–902.

Lindsay, T.H., Thiele, T.R., and Lockery, S.R. (2011). Optogenetic analysis of synaptic transmission in the central nervous system of the nematode Caenorhabditis elegans. Nat Comms *2*, 306–309.

Liu, P., Chen, B., and Wang, Z.W. (2011a). Gap Junctions Synchronize Action Potentials and Ca2+ Transients in Caenorhabditis elegans Body Wall Muscle. Journal of Biological Chemistry *286*, 44285–44293.

Liu, P., Ge, Q., Chen, B., Salkoff, L., Kotlikoff, M.I., and Wang, Z.W. (2011b). Genetic dissection of ion currents underlying all-or-none action potentials in C. elegans body-wall muscle cells. The Journal of Physiology *589*, 101–117.

Liu, P., Chen, B., and Wang, Z.-W. (2013). Postsynaptic current bursts instruct action potential firing at a graded synapse. Nat Comms *4*, 1911–1911.

Liu, Q., Hollopeter, G., and Jorgensen, E.M. (2009). Graded synaptic transmission at the Caenorhabditis elegans neuromuscular junction. Proc Natl Acad Sci USA *106*, 10823–10828.

Luo, L., Clark, D.A., Biron, D., Mahadevan, L., and Samuel, A.D.T. (2006). Sensorimotor control during isothermal tracking in Caenorhabditis elegans. J Exp Biol *209*, 4652–4662.

Marder, E., and Bucher, D. (2001). Central pattern generators and the control of rhythmic movements. Current Biology *11*, R986–R996.

Marder, E., and Bucher, D. (2007). Understanding Circuit Dynamics Using the Stomatogastric Nervous System of Lobsters and Crabs. Annu. Rev. Physiol. *69*, 291–316.

McIntire, S.L., Jorgensen, E., Kaplan, J., and Horvitz, H.R. (1993). The GABAergic nervous system of Caenorhabditis elegans. Nature *364*, 337–341.

Nakai, J., Ohkura, M., and Imoto, K. (2001). A high signal-to-noise Ca(2+) probe composed of a single green fluorescent protein. Nat Biotechnol *19*, 137–141.

Nathoo, A.N., Moeller, R.A., Westlund, B.A., and Hart, A.C. (2001). Identification of neuropeptide-like protein gene families in Caenorhabditiselegans and other species. Proc Natl Acad Sci USA *98*, 14000–14005.

Nelson, L.S. (1998). Disruption of a Neuropeptide Gene, flp-1, Causes Multiple Behavioral Defects in Caenorhabditis elegans. Science *281*, 1686–1690.

Niebur, E., and Erdös, P. (1991). Theory of the locomotion of nematodes: Dynamics of undulatory progression on a surface. Biophysical Journal *60*, 1132–1146.

Niebur, E., and Erdös, P. (1993). Theory of the locomotion of nematodes: control of the somatic motor neurons by interneurons. Math Biosci *118*, 51–82.

Omura, D.T., Clark, D.A., Samuel, A.D.T., and Horvitz, H.R. (2012). Dopamine Signaling Is Essential for Precise Rates of Locomotion by C. elegans. PLoS ONE *7*, e38649.

Overduin, S.A., d'Avella, A., Carmena, J.M., and Bizzi, E. (2012). Microstimulation Activatesa Handful of Muscle Synergies. Neuron *76*, 1071–1077.

Overduin, S.A., d'Avella, A., Roh, J., and Bizzi, E. (2008). Modulation of muscle synergy recruitment in primate grasping. J Neurosci *28*, 880–892.

Phelan, P., and Starich, T.A. (2001). Innexins get into the gap. Bioessays *23*, 388–396.

Pierce-Shimomura, J.T., Faumont, S., Gaston, M.R., Pearson, B.J., and Lockery, S.R. (2001). The homeobox gene lim-6 is required for distinct chemosensory representations in C. elegans. Nature *410*, 694–698.

Pierce-Shimomura, J.T., Morse, T.M., and Lockery, S.R. (1999). The fundamental role of pirouettes in Caenorhabditis elegans chemotaxis. J Neurosci *19*, 9557–9569.

Pierce-Shimomura, J.T., Chen, B.L., Mun, J.J., Ho, R., Sarkis, R., and McIntire, S.L. (2008). Genetic analysis of crawling and swimming locomotory patterns in C. elegans. Proc Natl Acad Sci USA *105*, 20982–20987.

Piggott, B.J., Liu, J., Feng, Z., Wescott, S.A., and Xu, X.Z.S. (2011). The Neural Circuits and Synaptic Mechanisms Underlying Motor Initiation in C. elegans. Cell *147*, 922–933.

Porter, J., Craven, B., Khan, R.M., Chang, S.-J., Kang, I., Judkewicz, B., Volpe, J., Settles, G., and Sobel, N. (2006). Mechanisms of scent-tracking in humans. Nature Publishing Group *10*, 27–29.

Ramot, D., Johnson, B.E., Berry, T.L., Carnell, L., and Goodman, M.B. (2008). The Parallel Worm Tracker: A Platform for Measuring Average Speed and Drug-Induced Paralysis in Nematodes. PLoS ONE *3*, e2208.

Rand, J.B., and Nonet, M.L. (1997) Appendix 2 Neurotransmitter Assignments for Specific Neurons. In: Riddle DL, Blumenthal T, Meyer BJ, et al., editors. C. elegans II. 2nd edition. Cold Spring Harbor (NY): Cold Spring Harbor Laboratory Press.

Ren, P., Lim, C.S., Johnsen, R., Albert, P.S., Pilgrim, D., and Riddle, D.L. (1996). Control of C. elegans larval development by neuronal expression of a TGF-beta homolog. Science *274*, 1389–1391.

Ryu, W.S., and Samuel, A.D.T. (2002). Thermotaxis in Caenorhabditis elegans analyzed by measuring responses to defined Thermal stimuli. J Neurosci *22*, 5727–5733.

Sakata, K., and Shingai, R. (2004). Neural network model to generate head swing in locomotion of Caenorhabditis elegans. Network: Computation in Neural Systems *15*, 199–216.

Satoh, Y., Sato, H., Kunitomo, H., Fei, X., Hashimoto, K., and Iino, Y. (2014). Regulation of Experience-Dependent Bidirectional Chemotaxis by a Neural Circuit Switch in Caenorhabditis elegans. J Neurosci *34*, 15631–15637.

Sawin, E.R., Ranganathan, R., and Horvitz, H.R. (2000). C. elegans locomotory rate is modulated by the environment through a dopaminergic pathway and by experience through a serotonergic pathway. Neuron *26*, 619–631.

Sawin, E.P., Harris, L.R., Campos, A.R., and Sokolowski, M.B. (1994). Sensorimotor transformation from light reception to phototactic behavior inDrosophila larvae (Diptera: Drosophilidae). J Insect Behav *7*, 553–567.

Schrödel, T., Prevedel, R., Aumayr, K., Zimmer, M., and Vaziri, A. (2013). Brain-wide 3D imaging of neuronal activity in Caenorhabditis elegans with sculpted light. Nat Meth *10*, 1013–1020.

Schwarz, E.M. (2005). Genomic classification of protein-coding gene families. WormBook.

Sherrington, C.S. (1910). Flexion-reflex of the limb, crossed extension-reflex, and reflex stepping and standing. The Journal of Physiology *40*, 28–121.

Sieburth, D., Ch'ng, Q., Dybbs, M., Tavazoie, M., Kennedy, S., Wang, D., Dupuy, D., Rual, J.-F., Hill, D.E., Vidal, M., et al. (2005). Systematic analysis of genes required for synapse structure and function. Nature *436*, 510–517.

Starich, T.A., Lee, R.Y., Panzarella, C., Avery, L., and Shaw, J.E. (1996). eat-5 and unc-7 represent a multigene family in Caenorhabditis elegans involved in cell-cell coupling. J. Cell Biol. *134*, 537–548.

Stawicki, T.M., Takayanagi-Kiya, S., Zhou, K., and Jin, Y. (2013). Neuropeptides Function in a Homeostatic Manner to Modulate Excitation-Inhibition Imbalance in C. elegans. PLoS Genet *9*, e1003472.

Stephens, G.J., Bueno de Mesquita, M., Ryu, W.S., and Bialek, W. (2011a). Emergence of long timescales and stereotyped behaviors in Caenorhabditis elegans. Proceedings of the National Academy of Sciences *108*, 7286–7289.

Stephens, G.J., Osborne, L.C., and Bialek, W. (2011b). Searching for simplicity in the analysis of neurons and behavior. Proceedings of the National Academy of Sciences *108*, 15565–15571.

Stephens, G.J., Johnson-Kerner, B., Bialek, W., and Ryu, W.S. (2008). Dimensionality and Dynamics in the Behavior of C. elegans. PLoS Comput Biol *4*, e1000028.

Stephens, G.J., Johnson-Kerner, B., Bialek, W., and Ryu, W.S. (2010). From Modes to Movement in the Behavior of Caenorhabditis elegans. PLoS ONE *5*, e13914.

Sulston J, Horvitz H R, Kimble J. Wood W B, editor. (1988) The nematode Caenorhabditis elegans. Cold Spring Harbor, New York: Cold Spring Harbor Laboratory; Appendix 3. Cell lineage. pp. 457–489.

Sulston, J.E., and Horvitz, H.R. (1977). Post-embryonic cell lineages of the nematode, Caenorhabditis elegans. Dev Biol *56*, 110–156.

Sulston, J.E., Schierenberg, E., White, J.G., and Thomson, J.N. (1983). The embryonic cell lineage of the nematode Caenorhabditis elegans. Dev Biol *100*, 64–119.

Sulston, J., Dew, M., and Brenner, S. (1975). Dopaminergic neurons in the nematode Caenorhabditis elegans. J Comp Neurol *163*, 215–226.

Suzuki, H., Thiele, T.R., Faumont, S., Ezcurra, M., Lockery, S.R., and Schafer, W.R. (2008). Functional asymmetry in Caenorhabditis elegans taste neurons and its computational role in chemotaxis. Nature *454*, 114–117.

Talpalar, A.E., Bouvier, J., Borgius, L., Fortin, G., Pierani, A., and Kiehn, O. (2013). Dual-mode operation of neuronal networks involved in left-right alternation. Nature *500*, 85–88.

Thiele, T.R., Faumont, S., and Lockery, S.R. (2009). The Neural Network for Chemotaxis to Tastants in Caenorhabditis elegans Is Specialized for Temporal Differentiation. J Neurosci *29*, 11904–11911.

Tian, L., Hires, S.A., Mao, T., Huber, D., Chiappe, M.E., Chalasani, S.H., Petreanu, L., Akerboom, J., McKinney, S.A., Schreiter, E.R., et al. (2009). Imaging neural activity in worms, flies and mice with improved GCaMP calcium indicators. Nat Meth *6*, 875–881.

Ting, L.H., and Macpherson, J.M. (2005). A limited set of muscle synergies for force control during a postural task. Journal of Neurophysiology *93*, 609–613.

Torres-Oviedo, G., and Ting, L.H. (2007). Muscle synergies characterizing human postural responses. Journal of Neurophysiology *98*, 2144–2156.

Touroutine, D., Fox, R.M., Stetina, Von, S.E., Burdina, A., Miller, D.M., and Richmond, J.E. (2005). acr-16 Encodes an Essential Subunit of the Levamisole-resistant Nicotinic Receptor at the Caenorhabditis elegans Neuromuscular Junction. Journal of Biological Chemistry *280*, 27013–27021.

Tresch, M.C., and Bizzi, E. (1999). Responses to spinal microstimulation in the chronically spinalized rat and their relationship to spinal systems activated by low threshold cutaneous stimulation. Exp Brain Res *129*, 401–416.

Tresch, M.C., and Jarc, A. (2009). The case for and against muscle synergies. Curr Opin Neurobiol *19*, 601–607.

Tsalik, E.L., and Hobert, O. (2003). Functional mapping of neurons that control locomotory behavior inCaenorhabditis elegans. J. Neurobiol. *56*, 178–197.

Varshney, L.R., Chen, B.L., Paniagua, E., Hall, D.H., and Chklovskii, D.B. (2011). Structural Properties of the Caenorhabditis elegans Neuronal Network. PLoS Comput Biol *7*, e1001066.

Vidal-Gadea, A., Topper, S., Young, L., Crisp, A., Kressin, L., Elbel, E., Maples, T., Brauner, M., Erbguth, K., Axelrod, A., et al. (2011). Caenorhabditis elegans selects distinct crawling and swimming gaits via dopamine and serotonin. Proceedings of the National Academy of Sciences *108*, 17504–17509.

Wakabayashi, T., Kitagawa, I., and Shingai, R. (2004). Neurons regulating the duration of forward locomotion in Caenorhabditis elegans. Neurosci Res *50*, 103–111.

Wani, K.A., Catanese, M., Normantowicz, R., Herd, M., Maher, K.N., and Chase, D.L. (2012). D1 Dopamine Receptor Signaling Is Modulated by the R7 RGS Protein EAT-16 and the R7 Binding Protein RSBP-1 in Caenoerhabditis elegans Motor Neurons. PLoS ONE 7, e37831.

Ward, S., Thomson, N., White, J.G., and Brenner, S. (1975). Electron microscopical reconstruction of the anterior sensory anatomy of the nematode Caenorhabditis elegans.N2UU. J Comp Neurol 160, 313–337.

Weimann, J.M., Meyrand, P., and Marder, E. (1991). Neurons that form multiple pattern generators: identification and multiple activity patterns of gastric/pyloric neurons in the crab stomatogastric system. Journal of Neurophysiology 65, 111–122.

Weinshenker, D., Garriga, G., and Thomas, J.H. (1995). Genetic and pharmacological analysis of neurotransmitters controlling egg laying in C. elegans. J Neurosci 15, 6975–6985.

Wen, Q., Po, M.D., Hulme, E., Chen, S., Liu, X., Kwok, S.W., Gershow, M., Leifer, A.M., Butler, V., Fang-Yen, C., et al. (2012). Proprioceptive Coupling within Motor Neurons Drives C. elegans Forward Locomotion. Neuron 76, 750–761.

White, J.G., Southgate, E., and Thomson, J.N. (1992). Mutations in the Caenorhabditis elegans unc-4 gene alter the synaptic input to ventral cord motor neurons. Nature 355, 838–841.

White, J.G., Southgate, E., Thomson, J.N., and Brenner, S. (1976). The Structure of the Ventral Nerve Cord of Caenorhabditis elegans. Philosophical Transactions of the Royal Society B: Biological Sciences 275, 327–348.

White, J.G., Southgate, E., Thomson, J.N., and Brenner, S. (1986). The structure of the nervous system of the nematode Caenorhabditis elegans. Philos. Trans. R. Soc. Lond., B, Biol. Sci. 314, 1–340.

Wicks, S.R., and Rankin, C.H. (1995). Integration of mechanosensory stimuli in Caenorhabditis elegans. J Neurosci 15, 2434–2444.

Yemini, E., Jucikas, T., Grundy, L.J., Brown, A.E.X., and Schafer, W.R. (2013). A database of Caenorhabditis elegans behavioral phenotypes. Nat Meth 10, 877–879.

Yu, S., Avery, L., Baude, E., and Garbers, D.L. (1997). Guanylyl cyclase expression in specific sensory neurons: a new family of chemosensory receptors. Proc Natl Acad Sci USA 94, 3384–3387.

Zheng, Y., Brockie, P.J., Mellem, J.E., Madsen, D.M., and Maricq, A.V. (1999). Neuronal control of locomotion in C. elegans is modified by a dominant mutation in the GLR-1 ionotropic glutamate receptor. Neuron 24, 347–361.

Zimmer, M., Gray, J.M., Pokala, N., Chang, A.J., Karow, D.S., Marletta, M.A., Hudson, M.L., Morton, D.B., Chronis, N., and Bargmann, C.I. (2009). Neurons detect increases and decreases in oxygen levels using distinct guanylate cyclases. Neuron 61, 865–879.

7 Acknowledgements

8 Curriculum Vitae

Ingrid Margarete Hums

Education

11 /2010 – 11 /2015	**Doctoral studies – PhD in Molecular Biology** Vienna Biocenter International PhD program, University of Vienna, Austria, Research conducted at Research Institute of Molecular Pathology (IMP), Vienna
10 /2006 – 09 /2010	**Diploma studies of Molecular Medicine** Albert-Ludwigs-University of Freiburg, Germany
08 /2007 – 06 /2008	**Erasmus program – International studies of Biology** Subjects: genetics and genomics Uppsala University, Sweden
10 /2005 – 09 /2006	**Basic studies of Molecular medicine** Albert-Ludwigs-University of Freiburg, Germany
10 /2003 – 09 /2005	**Pre-clinical studies of Medicine** Ludwig-Maximilians-University of Munich, Germany

Research experiences

Graduate studies in Behavioral Neuroscience at Research Institute of Molecular Pathology (IMP), Vienna, Austria

11 /2010 – 11 /2015	Laboratory of Manuel Zimmer, "Neural control over crawling and steering motions underlies the regulation of locomotion strategies in *C. elegans*"

Diploma thesis work in Epigenetics Research at Max-Planck Institute of Immunobiology Freiburg, Germany

12 /2009 - 09 /2010	Laboratory of Robert Schneider "Functional analysis of new histone modifications"

Research internship and student assistant work, University Freiburg, Germany

11 /2008 - 03 /2009	Laboratory of Ralf Baumeister, Institute for Bioinformatics and Molecular Genetics "Construction and expression of transgenes to rescue *C. elegans* deletion mutant of spinal muscular atrophy gene smn-1"

Genetic research internships at Uppsala University, Sweden

01 - 03 /2008	Laboratory of Klas Kullander, Dept. of Neuroscience, Unit of Developmental Genetics "Study of genetic markers for locomotor central pattern generator (CPG) in mice"
11 - 12 /2007	Laboratory of Leif Andersson, Dept. of Medical Biochemistry and Microbiology "Fine mapping of a major locus for autoimmune thyroiditis in chicken"

Presentations at International Conferences during Doctoral studies

Talks:

- **ESF-EMBO Symposium** "Flies, Worms and Robots: Combining Perspectives on Minibrains and Behaviour" **Sant Feliu de Guixols, Spain** 11/2014
- **C. elegans Topic Meeting** „Neuronal Development, Synaptic Function and Behavior" **Madison/ Wisconsin, USA** 07/2014

Poster presentations:

- **Berlin *C. elegans* Meeting** 05/2014
- **FENS-Brain Conference** "Controlling Neurons, Circuits and Behavior" **Rungstedgaard, Denmark** 04/2015
- **19th International C. elegans Meeting**, **Los Angeles, California, USA** 06/2013

Publications

Gramstrup Petersen J, Rojo Romanos T, Juozaityte V, Redo Riveiro A, **Hums I**, Traunmüller L, Zimmer M, and Pocock R (2013). "EGL-13/SoxD Specifies Distinct O2 and CO2 Sensory Neuron Fates in Caenorhabditis elegans" PLoS Genet *9*, e1003511.